

1 SEARCH FOR  $t\bar{t}Z' \rightarrow t\bar{t}t\bar{t}$  PRODUCTION IN THE MULTILEPTON FINAL STATE IN  
2  $pp$  COLLISIONS AT  $\sqrt{s} = 13$  TEV WITH THE ATLAS DETECTOR

By

Hieu Le

## A DISSERTATION

Submitted to  
Michigan State University  
in partial fulfillment of the requirements  
for the degree of

## Physics — Doctor of Philosophy

2025

12

## ABSTRACT

13 This dissertation presents a search for a new beyond-the-Standard-Model (BSM) particle  
14 at the Large Hadron Collider (LHC). Many BSM models predict a new heavy vector boson  
15 ( $Z$ ) that couples primarily to the top quark in both production and decay (topophilic). The  
16 search is performed in multilepton events consistent with four-top-quark ( $t\bar{t}t\bar{t}$ ) production,  
17 due to the distinctive signature of the multilepton final states and its robustness against  
18 common background processes at the LHC. Analysis data was collected by the ATLAS  
19 detector from 2015 to 2018, using proton-proton collisions at the LHC at a center-of-mass  
20 energy of 13 TeV. No statistically significant deviation from Standard Model predictions is  
21 observed. Exclusion limits are set on the production cross section of the targeted topophilic  
22 particle in the mass range between 1 TeV and 3 TeV.

## ACKNOWLEDGMENTS

24        First and foremost, I am deeply grateful for my dissertation advisor and P.I, Professor  
25    Reinhard Schwienhorst, for his support, guidance and tolerance as part of my role in ATLAS  
26    and my doctoral program at Michigan State. Reinhard is the primary driving force in many  
27    exciting opportunities that I've had the chance to experience, and he also provides much-  
28    appreciated support both in knowledge and wisdom in times of need. I am incredibly thankful  
29    that Reinhard is one of the people that plays a part in who I am today.

30        I would like to express sincere gratitude to one of our postdocs in the MSU ATLAS  
31    group, Binbin Dong, who I closely worked with within ATLAS. Binbin is a massive source  
32    of support for physics, technical and ATLAS-specific knowledge that played a pivotal role  
33    during my training with ATLAS, during the analysis in this dissertation, and during my  
34    time at CERN. I would have never been able to find my way through without her help.

35        I am also extremely thankful for the MSU ATLAS group, in particular Professors Wade  
36    Fisher and Daniel Hayden, for their guidance and feedback on my professional and per-  
37    sonal endeavors which helped immensely in my development both scientifically and socially.  
38    I thank Rongqian Qian and Jason Gombas, my fellow advisees that offered great ideas,  
39    knowledge and friendship. I would like to thank Julia Hinds, Stergios Kazakos and Pratik  
40    Kafle for their support and companionship during my time at CERN. I also thank former and  
41    presents members of our group that I've had the pleasure to work with: Joey Huston, Jos  
42    Gabriel Reyes Rivera, Cecilia Imthurn, Xinfei Huang, Ahmed Tarek, Kyle Fielman, Robert  
43    Les and Trisha Farooque. It was a wonderful experience being part of the MSU ATLAS  
44    group and I hope our group continues to grow, even if it makes scheduling weekly meetings  
45    for everyone that much harder.

46 I would like to express my gratitude to my dissertation committee members, Professors  
47 Reinhard Schwienhorst, Johannes Pollanen, Wade Fisher, Remco Zegers and Yuying Xie, for  
48 their guidance, patience and commitment to my growth and success as a researcher and a  
49 person.

50 It has been a pleasure to work with the many outstanding people in ATLAS, especially  
51 the BSM multi-top analysis team. I would like to thank Philipp Gadow, Krisztian Peters,  
52 Frédéric Déliot and Neelam Kumari for their dedication and commitment to fostering a  
53 successful and fruitful collaboration. I also thank Meng-Ju Tsai, Hui-Chi Lin, Thomas  
54 Nommensen, Jianming Qian, Quake Qin, Tomke Schröer, Xilin Wang, Helena Gomez and  
55 Daniela Paredes for their tireless efforts in the analysis. I am truly glad to have had the  
56 chance to work with all of you.

57 Special thanks to my fellow graduate students that I have had the chance to befriend  
58 during my doctoral journey: Daniel Lay, Grayson Perez, Jordan Purcell, Eric Flynn, Isabella  
59 Molina, Mo Hassan, Cavan Maher and Hannah Berg. You all taught me a lot more than I  
60 could ever imagine and helped me more than I could ever asked for, and I look forward to  
61 see where we go from here.

62 Finally, I would like to thank my family, to whom this dissertation is dedicated: my  
63 spouse Allen Sechrist, for encouraging me tirelessly everyday and always being there for me  
64 even when I can't be there for myself; my cat Eddie, for being the best cat anyone could ask  
65 for; my brother Hien Le, my dad Bac Le, and my mom Thuy Cao, for their endless love and  
66 support. Thank you for being the reason that I am where I am today.

## TABLE OF CONTENTS

67	<b>List of Tables . . . . .</b>	vii
68	<b>List of Figures . . . . .</b>	ix
69	<b>KEY TO ABBREVIATIONS . . . . .</b>	xii
70	<b>Chapter 1. Introduction . . . . .</b>	1
71	<b>Chapter 2. Theoretical Overview . . . . .</b>	5
72	2.1 The Standard Model . . . . .	5
73	2.1.1 Elementary particles . . . . .	5
74	2.1.2 Mathematical formalism . . . . .	9
75	2.1.2.1 Quantum chromodynamics . . . . .	10
76	2.1.2.2 Electroweak theory . . . . .	11
77	2.1.2.3 Higgs mechanism . . . . .	14
78	2.2 Beyond the Standard Model: $t\bar{t}Z' \rightarrow t\bar{t}t\bar{t}$ . . . . .	17
79	2.2.1 Top-philic vector resonance . . . . .	17
80	2.2.2 Production channels . . . . .	19
81	2.2.3 Decay modes . . . . .	20
82	<b>Chapter 3. LHC &amp; ATLAS Experiment . . . . .</b>	22
83	3.1 The Large Hadron Collider . . . . .	22
84	3.1.1 Overview . . . . .	22
85	3.1.2 LHC operations . . . . .	24
86	3.1.3 Physics at the LHC . . . . .	25
87	3.2 The ATLAS detector . . . . .	25
88	3.2.1 Inner detector . . . . .	28
89	3.2.2 Calorimeter systems . . . . .	29
90	3.2.3 Muon spectrometer . . . . .	31
91	3.2.4 Trigger & data acquisition . . . . .	33
92	<b>Chapter 4. Particle Reconstruction &amp; Identification . . . . .</b>	34
93	4.1 Primary reconstruction . . . . .	34
94	4.1.1 Tracks . . . . .	34
95	4.1.2 Vertices . . . . .	35
96	4.1.3 Topological clusters . . . . .	36
97	4.2 Jets . . . . .	37
98	4.2.1 Jet reconstruction . . . . .	38
99	4.2.2 Flavor tagging . . . . .	39
100	4.3 Leptons . . . . .	43
101	4.3.1 Electrons . . . . .	43
102	4.3.2 Muons . . . . .	46

103	4.4	Missing transverse momentum . . . . .	48
104	4.5	Overlap removal . . . . .	49
105	4.6	Object definition . . . . .	50
106	<b>Chapter 5. Data &amp; Simulated Samples</b>	. . . . .	<b>51</b>
107	5.1	Data samples . . . . .	51
108	5.2	Monte Carlo samples . . . . .	51
109	5.2.1	$t\bar{t}Z'$ signal samples . . . . .	52
110	5.2.2	Background samples . . . . .	54
111	<b>Chapter 6. Analysis Strategy</b>	. . . . .	<b>59</b>
112	6.1	Event selection . . . . .	59
113	6.1.1	Event categorization . . . . .	60
114	6.2	Analysis regions . . . . .	61
115	6.2.1	Signal regions . . . . .	63
116	6.2.2	Control regions . . . . .	64
117	6.3	Background estimation . . . . .	67
118	6.3.1	Template fitting for fake/non-prompt estimation . . . . .	68
119	6.3.2	Charge misidentification data-driven estimation . . . . .	68
120	6.3.3	$t\bar{t}W$ background data-driven estimation . . . . .	71
121	<b>Chapter 7. Systematic Uncertainties</b>	. . . . .	<b>74</b>
122	7.1	Experimental uncertainties . . . . .	74
123	7.1.1	Luminosity & pile-up reweighting . . . . .	74
124	7.1.2	Leptons . . . . .	74
125	7.1.3	Jets . . . . .	75
126	7.1.4	Missing transverse energy . . . . .	77
127	7.2	Modeling uncertainties . . . . .	78
128	7.2.1	Signal and irreducible background uncertainties . . . . .	78
129	7.2.2	Reducible background uncertainties . . . . .	80
130	<b>Chapter 8. Results</b>	. . . . .	<b>82</b>
131	8.1	Statistical interpretation . . . . .	82
132	8.1.1	Profile likelihood fit . . . . .	82
133	8.1.2	Exclusion limit . . . . .	85
134	8.2	Fit results . . . . .	86
135	<b>Chapter 9. Summary</b>	. . . . .	<b>92</b>
136	<b>References</b>	. . . . .	<b>93</b>

# List of Tables

<sup>137</sup>	Table 4.1: Overlap removal process for this analysis, applied sequentially from top to bottom. . . . .	49
<sup>140</sup>	Table 4.2: Summary of object selection criteria used in this analysis. $\ell_0$ refers to the leading lepton in the event. . . . .	50
<sup>142</sup>	Table 5.1: Summary of all HLT triggers used in this analysis. Events are required to pass at least one trigger. . . . .	52
<sup>144</sup>	Table 5.2: Summary of all Monte-Carlo samples used in this analysis. $V$ refers to an EW ( $W^\pm/Z/\gamma^*$ ) or Higgs boson. Matrix element (ME) order refers to the order in QCD of the perturbative calculation. Tune refers to the underlying-event tune of the parton shower (PS) generator. . . . .	53
<sup>148</sup>	Table 6.1: Definitions of signal, control and validation regions (VR) used in this analysis. $N_{\text{jets}}$ and $N_b$ refers to the number of jets and number of $b$ -tagged jets respectively. $\ell_1$ refers to the leading lepton, $\ell_2$ refers to the subleading lepton and so on. $H_T$ refers to the $p_T$ scalar sum of all leptons and jets in the event. $m_{\ell\ell}$ refers to the dilepton invariant mass, which must not coincide with the $Z$ -boson mass range of 81-101 GeV for SS2L+3L events. . . . .	62
<sup>154</sup>	Table 6.2: Definitions of SR sub-regions. Events are sorted into different sub-regions based on the number of $b$ -tagged jets and leptons present. . . . .	63
<sup>156</sup>	Table 6.3: List of possible assigned values for DFCAA. . . . .	66
<sup>157</sup>	Table 8.1: Normalization factors for backgrounds with dedicated CRs, obtained from a simultaneous fit in all CRs and SR under the background-only hypothesis. The nominal pre-fit value is 1 for all NFs and 0 for the scaling factors $a_0$ and $a_1$ . Uncertainties shown include both statistical and systematic uncertainties.	88

161	Table 8.2: Pre-fit and post-fit background yields in the inclusive SR. The number of 162 data events and pre-fit estimate signal yields are also shown. Background 163 yields shown are obtained from the fit using the $t\bar{t}Z'$ signal sample with 164 $m_{Z'} = 2$ TeV. Pre-fit yields for $t\bar{t}W$ background are set to 0 nominally 165 prior to data-driven normalization. Total yield uncertainty differs from 166 the quadrature sum of constituent uncertainties due to correlation and 167 anticorrelation effects. . . . .	90
168	Table 8.3: Post-fit impact of uncertainty sources on the signal strength $\mu$ , grouped by 169 categories. Values shown are obtained from the fit using the $t\bar{t}Z'$ signal 170 sample with $m_{Z'} = 2$ TeV. Impact on $\mu$ is evaluated for each uncertainty 171 category by re-fitting with the corresponding set of NPs fixed to their best- 172 fit values. Total uncertainty differs from the quadrature sum of constituent 173 uncertainties due to correlation between NPs in the fit. . . . .	91

# List of Figures

174	Figure 2.1: Particles within the SM and their properties. . . . .	6
176	Figure 2.2: Feynman diagram for $t\bar{t}$ production and subsequent decay processes. Top quark decays into a $W$ -boson and $b$ -quarks, and $W$ -boson can decay to a $q\bar{q}$ or a $\ell\nu_\ell$ pair. . . . .	8
179	Figure 2.3: Illustration of a common representation of the Higgs potential. Before SSB, the ground state $\phi(0)$ is located at A which is symmetric with respect to the potential. A perturbation to this state fixes the ground state energy $ \phi(0) ^2$ to a particular value at B, "spontaneously" breaking the symmetry and degeneracy in $ \phi(0) ^2$ . . . . .	15
184	Figure 2.4: Feynman diagrams for tree level $Z'$ production in association with (a) $t\bar{t}$ , (b) $tj$ (light quark) and (c) $tW$ , decaying to final states containing (a) $t\bar{t}t\bar{t}$ or (b)(c) $t\bar{t}t$ . . . . .	19
187	Figure 2.5: Theoretical $t\bar{t}Z'$ production cross-section times $Z' \rightarrow t\bar{t}$ branching ratio as a function of the $Z'$ mass at LO in QCD coupling to top with $c_t = 1$ under a simplified top-philic model [45, 73, 76]. . . . .	20
190	Figure 2.6: Branching ratios for $t\bar{t}t\bar{t}$ decay. The same-sign dilepton and multilepton channels together forms the SSML channel. . . . .	21
192	Figure 3.1: The full CERN accelerator complex as of 2022. . . . .	23
193	Figure 3.2: Current and future timeline of LHC operations as of 2025 with corresponding center-of-mass energies and projected integrated luminosities. . .	24
195	Figure 3.3: Summary of predicted and measured cross-section for SM processes at the LHC at different center-of-mass energies . . . . .	26
197	Figure 3.4: A cross section slice of the ATLAS detector showing different subsystems along with visualization of different types of particles traveling through the detector . . . . .	27

200	Figure 3.5: Cutaway illustration of the inner detector along with its subsystems. . . . .	28
201	Figure 3.6: Cutaway illustration of the calorimeter system including the EM, hadronic 202 and LAr forward calorimeters . . . . .	30
203	Figure 4.1: Stages of topo-cluster formation corresponding to each threshold. In (a), 204 proto-clusters are seeded from cells with adequate signal significance $\zeta_{\text{cell}}^{\text{EM}}$ . 205 The clusters are further merged and split in (b) according to a predefined 206 cluster growth threshold. The process stops in (c) when all sufficiently 207 significant signal hits have been matched to a cluster. . . . .	37
208	Figure 4.2: Jet energy scale calibration sequence for EM-scale jets. . . . .	39
209	Figure 4.3: Overview of the GN2 architecture. The number of jet and track features 210 are represented by $n_{\text{jf}}$ and $n_{\text{tf}}$ respectively. The global jet representation 211 and track embeddings output by the Transformer encoder are used as 212 inputs for three task-specific networks. . . . .	41
213	Figure 4.4: The $c$ -, light- and $\tau$ -jet rejection rate as a function of $b$ -tagging efficiency 214 for GN2 and DL1d using (a) jets in the $t\bar{t}$ sample, and (b) jets in the $Z'$ 215 sample. The performance ratios of GN2 to DL1d are shown in the bottom 216 panels. . . . .	42
217	Figure 6.1: Post-fit background composition in each analysis region and sub-region. 218 The fit was performed using ideal pseudo-datasets (Asimov data) in the SR. 61	
219	Figure 6.2: Pre-fit kinematic distributions and event compositions in the inclusive 220 SR for (a) $H_T$ i.e. scalar sum of $p_T$ of all objects in the event, (b) jet 221 multiplicity, (c) $b$ -jet multiplicity, (d) leading lepton $p_T$ . The shaded band 222 represents the uncertainty in the total distribution. The first and last bins 223 of each distribution contains underflow and overflow events respectively. . . . .	65
224	Figure 6.3: Charge flip rate calculated for SR and CR $t\bar{t}W$ in bins of $ \eta $ and $p_T$ . . . . .	70
225	Figure 7.1: Combined QmisID uncertainty rate for SR in bins of $ \eta $ and $p_T$ . . . . .	81
226	Figure 8.1: Observed (solid line) and expected (dotted line) upper limits as a function 227 of the $Z'$ mass at 95% CL on the cross-section of $pp \rightarrow t\bar{t}Z'$ production 228 times the $Z' \rightarrow t\bar{t}$ branching ratio. The region above the observed limit is 229 excluded. The solid blue line represents the theoretical signal cross-section 230 with $ct = 1$ at LO in QCD. The green and yellow bands represent the 231 68% ( $\pm\sigma$ ) and 95% ( $\pm 2\sigma$ ) confidence intervals respectively. . . . .	88



## KEY TO ABBREVIATIONS

### Physical & Mathematical Quantities

<sup>239</sup>  $\chi^2$  chi-squared

<sup>240</sup>  $d_0$  transverse impact parameter

<sup>241</sup>  $\Delta R$  angular distance

<sup>242</sup>  $\sqrt{s}$  center-of-mass energy

<sup>243</sup>  $\eta$  pseudorapidity

<sup>244</sup>  $E_T$  transverse energy

<sup>245</sup>  $E_T^{\text{miss}}$  missing transverse energy

<sup>246</sup>  $\Gamma$  decay width

<sup>247</sup>  $\gamma_5$  chirality projection operator

<sup>248</sup>  $\gamma_\mu$  Dirac matrices

<sup>249</sup>  $H_0$  null hypothesis

<sup>250</sup>  $H_T$  scalar sum of transverse momenta  $p_T$  of all objects in an event

<sup>251</sup>  $\mathcal{L}$  Lagrangian

<sup>252</sup>  $\mathcal{L}(\theta)$  likelihood function

<sup>253</sup>  $L$  instantaneous luminosity

<sup>254</sup>  $m_{\ell\ell}$  dilepton invariant mass

<sup>255</sup>  $\mu$  signal strength

<sup>256</sup>  $\mu_F$  factorization scale

<sup>257</sup>  $\mu_R$  renormalization scale

<sup>258</sup>  $N_{\text{jets}}$  number of jets/jet multiplicity

<sup>259</sup>  $\mathcal{O}(n)$  on the order of  $n$

<sup>260</sup>  $\mathcal{P}$  Poisson probability

<sup>261</sup>  $p_T$  transverse momentum

- <sup>262</sup>  $Q$  electric charge  
<sup>263</sup>  $q_\mu$  profile likelihood ratio  
<sup>264</sup>  $\sigma$  standard deviation  
<sup>265</sup>  $\sigma[b]$  cross-section  
<sup>266</sup>  $z_0$  longitudinal impact parameter

## Particles & Processes

- <sup>267</sup>
- <sup>268</sup>  $\gamma^*$  virtual photon  
<sup>269</sup>  $gg$  gluon-gluon fusion  
<sup>270</sup>  $pp$  proton-proton  
<sup>271</sup> PbPb lead-lead  
<sup>272</sup>  $q$  quark  
<sup>273</sup>  $q\bar{q}$  quark-antiquark pair  
<sup>274</sup>  $t\bar{t}$  top/anti-top quark pair  
<sup>275</sup>  $t\bar{t}X$  top pair in association with another particle  
<sup>276</sup>  $t\bar{t}t\bar{t}$  four-top-quark  
<sup>277</sup>  $V$  massive vector bosons ( $W^\pm, Z$ )  
<sup>278</sup>  $H$  Higgs in association with a vector boson

## Acronyms

- <sup>279</sup>
- <sup>280</sup> **1LOS** one lepton, or two leptons of opposite charges  
<sup>281</sup> **2HDM** two-Higgs doublet model  
<sup>282</sup> **AF3** AtlFast3 fast simulation  
<sup>283</sup> **ALICE** A Large Ion Collider Experiment  
<sup>284</sup> **ATLAS** A Toroidal LHC ApparatuS  
<sup>285</sup> **AWAKE** Advanced WAKEfield Experiment  
<sup>286</sup> **BDT** boosted decision tree  
<sup>287</sup> **BR** branching ratio

- <sup>288</sup> **BSM** Beyond the Standard Model
- <sup>289</sup> **CB** combined muon
- <sup>290</sup> **CERN** European Organization for Nuclear Research
- <sup>291</sup> **CKM** Cabibbo-Kobayashi-Maskawa matrix
- <sup>292</sup> **CL** confidence level
- <sup>293</sup> **CMS** Compact Muon Solenoid
- <sup>294</sup> **CP** charge-parity symmetry
- <sup>295</sup> **CR** control region
- <sup>296</sup> **CSC** Cathode Strip Chambers
- <sup>297</sup> **CTP** Central Trigger Processor
- <sup>298</sup> **ECIDS** Electron Charge ID Selector
- <sup>299</sup> **EFT** effective field theory
- <sup>300</sup> **EM** electromagnetic
- <sup>301</sup> **EW** electroweak
- <sup>302</sup> **FASER** ForwArd Search ExpeRiment
- <sup>303</sup> **FCal** forward calorimeter
- <sup>304</sup> **FS** full detector simulation
- <sup>305</sup> **GNN** graph neural network
- <sup>306</sup> **GRL** Good Run List
- <sup>307</sup> **GSC** Global Sequential Calibration
- <sup>308</sup> **GSF** Gaussian-sum filter
- <sup>309</sup> **GUT** Grand Unified Theory
- <sup>310</sup> **HEC** hadronic endcap calorimeter
- <sup>311</sup> **HF** heavy-flavor
- <sup>312</sup> **HL-LHC** High-Luminosity Large Hadron Collider
- <sup>313</sup> **HLT** High-Level Trigger
- <sup>314</sup> **ID** Inner Detector

- <sup>315</sup> **IP** interaction point
- <sup>316</sup> **JER** jet energy resolution
- <sup>317</sup> **JES** jet energy scale
- <sup>318</sup> **JVT** Jet Vertex Tagger
- <sup>319</sup> **KATRIN** Karlsruhe Tritium Neutrino Experiment
- <sup>320</sup> **L1** Level 1
- <sup>321</sup> **LAr** liquid argon
- <sup>322</sup> **LF** light-flavor
- <sup>323</sup> **LH** likelihood
- <sup>324</sup> **LHC** Large Hadron Collider
- <sup>325</sup> **LHCb** Large Hadron Collider beauty
- <sup>326</sup> **LINAC** linear accelerator
- <sup>327</sup> **LLH** log-likelihood
- <sup>328</sup> **LO** leading order
- <sup>329</sup> **MC** Monte Carlo simulation
- <sup>330</sup> **ME** matrix element
- <sup>331</sup> **ML** multilepton
- <sup>332</sup> **MS** Muon Spectrometer
- <sup>333</sup> **MDT** Monitored Drift Tubes
- <sup>334</sup> **MET** missing transverse energy
- <sup>335</sup> **NF** normalization factor
- <sup>336</sup> **NNJvt** Neural Network-based Jet Vertex Tagger
- <sup>337</sup> **NLO** next-to-leading order
- <sup>338</sup> **NNLO** next-to-next-to-leading order
- <sup>339</sup> **NP** nuisance parameter
- <sup>340</sup> **OP** operating point (also working point)
- <sup>341</sup> **OS** opposite-sign

- <sup>342</sup> **PCBT** pseudo-continuous  $b$ -tagging
- <sup>343</sup> **PDF** parton distribution function
- <sup>344</sup> **POI** parameter of interest
- <sup>345</sup> **PS** parton shower
- <sup>346</sup> **PV** primary vertex
- <sup>347</sup> **QCD** quantum chromodynamics
- <sup>348</sup> **QED** quantum electrodynamics
- <sup>349</sup> **QFT** quantum field theory
- <sup>350</sup> **QmisID** charge mis-identification
- <sup>351</sup> **RPC** Resistive Plate Chamber
- <sup>352</sup> **SCT** Semiconductor Tracker
- <sup>353</sup> **SF** scale factor
- <sup>354</sup> **SM** Standard Model
- <sup>355</sup> **SR** signal region
- <sup>356</sup> **SS** same-sign
- <sup>357</sup> **SSB** spontaneous symmetry breaking
- <sup>358</sup> **SS2L** same-sign dilepton
- <sup>359</sup> **SSML** same-sign dilepton, or more than two leptons of any charges
- <sup>360</sup> **TDAQ** Trigger and Data Acquisition
- <sup>361</sup> **TGC** Thin-Gap Chamber
- <sup>362</sup> **TRT** Transition Radiation Tracker
- <sup>363</sup> **VEV** vacuum expectation value
- <sup>364</sup> **VR** validation region
- <sup>365</sup> **UE** underlying-event

# <sup>366</sup> Chapter 1. Introduction

<sup>367</sup> The 20<sup>th</sup> century ushered in a revolutionary period for mankind's understanding of the  
<sup>368</sup> fundamental nature of matter and the forces that govern our universe with the development  
<sup>369</sup> of special relativity and quantum mechanics, which redefined our understanding of space,  
<sup>370</sup> time, energy and matter at the furthest extremes of scale from the vast reaches of the cosmos  
<sup>371</sup> to the tiniest constituents of matter. Building on these principles, Quantum Electrodynamics  
<sup>372</sup> (QED) [1–3] was developed as the first successful quantum field theory (QFT) describing  
<sup>373</sup> electromagnetism. The discovery of beta decay [4] and its paradoxical behaviors within the  
<sup>374</sup> framework of QED prompted the prediction of neutrinos and development of the theory of  
<sup>375</sup> weak interaction.

<sup>376</sup> At around the same time, a spectrum of strongly interacting particles was discovered  
<sup>377</sup> [5] as particle accelerators probed deeper into atomic nuclei, leading to the formation of  
<sup>378</sup> the quark model in the 1960s and with it a hypothesized new binding force, the strong  
<sup>379</sup> force. However, the QFT framework remained incapable of describing the weak and strong  
<sup>380</sup> interactions until advancements in gauge theory and the quantization of non-Abelian gauge  
<sup>381</sup> via QFT resulted in the formation of Yang-Mills theory [6, 7]. This sparked a renaissance  
<sup>382</sup> in modern physics with the unification of electromagnetism and weak force in 1967 under  
<sup>383</sup> the framework of electroweak (EW) [8] theory, as well as the development of Quantum  
<sup>384</sup> Chromodynamics (QCD) [9, 10] to describe the strong force binding quarks.

<sup>385</sup> At this point, the prediction of massless bosons within EW formalism remained a contra-  
<sup>386</sup> diction to the predicted massive  $W^\pm$  and  $Z$  bosons that mediate the weak force. This was  
<sup>387</sup> resolved by the introduction of EW spontaneous symmetry breaking and the Higgs mech-  
<sup>388</sup> anism in 1964 [11–13], which explained the generation of masses for both the EW bosons

389 and fermions. Together, these developments culminated in the Standard Model of parti-  
390 cle physics SM [14], a comprehensive theory that described the electromagnetic, weak, and  
391 strong interactions, classified all known fundamental particles and predicted mathematically  
392 consistent but not yet observed particles. Following its inception, particles predicted by the  
393 Standard Model were gradually observed experimentally, starting with the gluon in 1979  
394 [15], then the  $W^\pm$  and  $Z$  bosons [16, 17], and finally the top quark in 1995 [18, 19]. The  
395 final missing piece was confirmed as the Higgs boson was observed in 2012 independently  
396 by the ATLAS [20] and CMS [21] detectors at the Large Hadron Collider, completing the  
397 Standard Model after a 40-year search and cementing it as the most successful framework  
398 so far describing fundamental constituents of matter and their governing forces.

399 Despite its successes, the Standard Model remains incomplete. Key unanswered questions  
400 include the nature of dark matter [22], which makes up about 27% of the universes energy  
401 content but has no explanation within the Standard Model; the origin of neutrino masses and  
402 their oscillations [23]; the observed matter-antimatter asymmetry in the universe; possible  
403 unification of the EW and strong interaction into a Grand Unified Theory (GUT); and the  
404 hierarchy problem describing the large discrepancy in scales between forces and the apparent  
405 lightness of the Higgs boson compared to values predicted from quantum corrections.

406 After the discovery of the Higgs boson, efforts have been underway to construct new  
407 hypotheses and models in search of beyond the Standard Model (BSM) physics via different  
408 avenues, one of which being direct searches at colliders for new resonances or particles not  
409 predicted by the SM. In particular, the top quark possesses large mass and strong coupling to  
410 the Higgs boson [24] which gives it a special role in many proposed BSM models as a possible  
411 connection with strong coupling to new particles and heavy resonances. In addition, the  
412 top quark has a clean decay signature with well-understood final states and is produced in

abundance at the LHC from  $pp$  collisions in the form of top pairs  $t\bar{t}$  [25, 26]. This dissertation presents a search for the production of a heavy resonance that couples preferentially to top quark (top-philic) in association with a top pair ( $t\bar{t}$ ) in the final state with either two leptons of the same electric charge or at least three leptons (SSML). The search is performed in proton-proton collisions at  $\sqrt{s} = 13$  TeV with the ATLAS detector [27] via the four-top ( $t\bar{t}t\bar{t}$ ) production channel.

A similar search for top-philic heavy resonances was performed using a  $t\bar{t}t\bar{t}$  final state containing either one lepton or two opposite-sign leptons (1LOS) [28] with a much larger branching ratio of 56% and larger irreducible background of SM processes. Despite the small cross-section within the SM, the  $t\bar{t}t\bar{t}$  SSML final state provides heightened sensitivity to BSM physics and higher signal-to-background ratio than inclusive resonance searches (e.g. in dijet or dilepton final states) due to the distinctive signal signature and suppression of large SM background processes present in  $t\bar{t}$ -associated production i.e. diboson ( $VV$ ),  $t\bar{t}$  production with an additional boson ( $t\bar{t}V/ttH+jets$ ) or with additional light leptons from heavy-flavor decays ( $t\bar{t} + HF$ ). The cross-section for  $t\bar{t}t\bar{t}$  production can be enhanced by many proposed BSM models including supersymmetric gluino pair-production [29, 30], scalar gluon pair-production [31, 32], top-quark-compositeness models [33, 34], effective field theory (EFT) operators [26, 35–38] and two-Higgs-doublet models (2HDM) [39–43]. Searching within this channel is particularly motivated by the recent observed excess in the measurement of four-top production in the SSML final state at the LHC by the ATLAS detector [44] with a measured cross-section of  $24^{+7}_{-6}$  fb, almost double the SM prediction of  $13.4^{+1.0}_{-1.8}$  fb.

A simplified color-singlet vector boson model [45] is employed for the search to minimize parameter dependency on model choice. Data-driven background estimation methods are implemented for  $t\bar{t}W$ - one of the dominant irreducible backgrounds in the analysis - and

437 the charge misidentification background to rectify mismodeling related to jet multiplicity  
438 in simulated background that were not covered in the previous 1LOS search [28]. These  
439 methods are employed similarly to that in previous SM  $t\bar{t}t\bar{t}$  analyses [44, 46].

440 This dissertation is organized as follows. Chapter 2 presents the formalism of the SM and  
441 relevant BSM concepts. Chapter 3 provides an introduction to the LHC and ATLAS detector.  
442 Chapter 4 describes the reconstruction and identification of physics object from detector  
443 signals. Chapter 5 defines the data and simulated samples used in the analysis. Chapter 6  
444 describes the analysis strategy, including object definition, analysis region description and  
445 background estimation methods. Chapter 7 summarizes the uncertainties involved in the  
446 analysis. Chapter 8 presents the statistical interpretation and analysis results. Finally,  
447 Chapter 9 discusses a summary of the analysis and future outlook.

# <sup>448</sup> Chapter 2. Theoretical Overview

## <sup>449</sup> 2.1 The Standard Model

<sup>450</sup> The Standard Model of Physics (SM) [47] is currently the most successful formalism to  
<sup>451</sup> describe the physical world at a microscopic scale by providing descriptions for all currently  
<sup>452</sup> known elementary particles, along with three out of four fundamental forces (electromag-  
<sup>453</sup> netism, weak force, strong force) with the exception of gravity. The SM is however not  
<sup>454</sup> perfect, and there remains unanswered questions that require development and discovery  
<sup>455</sup> of new physics beyond the Standard Model (BSM). This chapter describes an overview of  
<sup>456</sup> important components within the SM and relevant BSM aspects for this analysis.

### <sup>457</sup> 2.1.1 Elementary particles

<sup>458</sup> Elementary particles in the SM can be classified into two groups: bosons consisting  
<sup>459</sup> of particles following Bose-Einstein statistics with integer spin, and fermions consisting of  
<sup>460</sup> particles following Fermi-Dirac statistics with half-integer spin. Fermions are the building  
<sup>461</sup> blocks of composite particles and consequently all known matter, and can be further classified  
<sup>462</sup> into quarks & leptons. Bosons act as force mediators for all fundamental forces described by  
<sup>463</sup> the SM, and can either be a scalar boson with spin 0 or vector gauge bosons with spin 1. For  
<sup>464</sup> each elementary particle, there also exists a corresponding antiparticle with identical mass  
<sup>465</sup> and opposite charge (electric or color). Figure 2.1 shows all known elementary particles in  
<sup>466</sup> the SM.

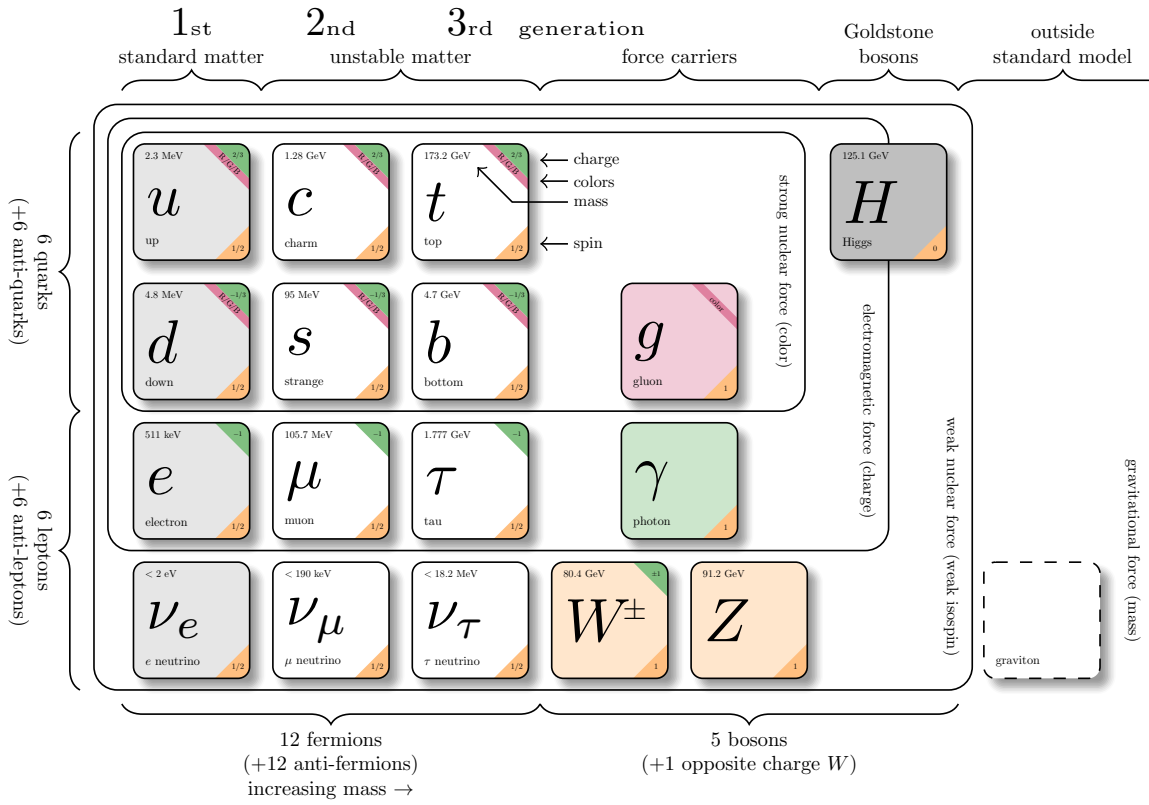


Figure 2.1: Particles within the SM and their properties [48].

## 467 Fermions

Fermions consist of quarks and leptons with six flavors each, grouped into three generations of doublets. The six quark flavors are up ( $u$ ), down ( $d$ ), charm ( $c$ ), strange ( $s$ ), bottom ( $b$ ) and top ( $t$ ), arranged in increasing order of mass. The quark flavors form three doublets ( $u, d$ ), ( $c, s$ ) and ( $t, b$ ), with each doublet containing one quark with electric charge of  $+2/3$  ( $u, s, t$ ), and the other with charge of  $-1/3$  ( $d, c, b$ ). Each quark also possesses a property known as color charge, with possible values of red ( $R$ ), green ( $G$ ), blue ( $B$ ) or their corresponding anticolor ( $\bar{R}, \bar{G}, \bar{B}$ ). Color charge follows color confinement rules, which allows only configurations of quarks with total neutral color charge to exist in isolation. Neutral

476 charge configurations can be formed from either a set of three colors ( $R, G, B$ ), a set of a  
477 color and its anticolor, or any combination of the two. Consequently, quarks can only exist  
478 in bound states called hadrons and no isolated quark can be found in a vacuum. Quarks are  
479 the only elementary particles in the SM that can interact with all four fundamental forces.

480 The three leptons doublets consist of three charged leptons: electron ( $e$ ), muon ( $\mu$ ), tau  
481 ( $\tau$ ), and their respective neutrino flavors: electron neutrino ( $\nu_e$ ), muon neutrino ( $\nu_\mu$ ), tau  
482 neutrino ( $\nu_\tau$ ). Charged leptons carry an electric charge of  $-1$ , while their antiparticles carry  
483 the opposite charge ( $+1$ ) and their corresponding neutrino flavors carry no charge. Charged  
484 leptons interact with all fundamental forces except the strong force, while neutrinos only  
485 interact with the weak force and gravity.

## 486 **Bosons**

487 The SM classifies bosons into two types: one scalar boson with spin 0 known as the  
488 Higgs ( $H$ ) boson, and vector gauge bosons with spin 1 known as gluons ( $g$ ), photon ( $\gamma$ ),  $W^\pm$   
489 and  $Z$  bosons [22]. Gluons and photon are massless, while the  $W^\pm$ ,  $Z$  and  $H$  bosons are  
490 massive. Each vector gauge boson serves as the mediator for a fundamental force described  
491 by the SM. Gluons are massless particles mediating the strong interaction by carrying color  
492 charges between quarks following quantum chromodynamics (QCD). Each gluon carries a  
493 non-neutral color charge out of eight linearly independent color states in the gluon color octet  
494 [49]. The photon is the massless and charge-neutral mediator particle for the electromagnetic  
495 interaction following quantum electrodynamics (QED). The  $W^\pm$  and  $Z$  bosons are massive  
496 mediator particles for the weak interaction, with the  $W^\pm$  boson carrying an electric charge  
497 of  $\pm 1$  while the  $Z$  boson is charge neutral.

498 Other than the vector gauge boson, the only scalar boson in the SM is the massive and

499 charge neutral Higgs boson [22]. The Higgs boson does not mediate any fundamental force  
 500 like vector bosons, but serve to provide the rest mass for all massive elementary particles in  
 501 the SM through the Higgs mechanism described in section 2.1.2.3.

502 **Top quark**

503 As of now, the top quark ( $t$ ) is the heaviest particle in the SM with mass of about 173 GeV  
 504 [50], approaching the EW symmetry breaking scale. Its high mass gives the top quark the  
 505 strongest Yukawa coupling to the Higgs boson ( $y_t \approx 1$ ) [24] and exotic resonances in many  
 506 proposed BSM models [51–54], making the top quark and its processes attractive vehicles  
 507 with which to probe new physics.

508 Due to its mass, the top quark has a  
 509 very short lifetime of  $10^{-24}$  s [22] and de-  
 510 cays before it can hadronize following color  
 511 confinement. The top quark decays to a  $W$   
 512 boson and a  $b$ -quark with a branching ratio  
 513 of almost 100%. The  $W$  boson can subse-  
 514 quently decay to a quark-antiquark pair or  
 515 to a lepton-neutrino pair (Figure 2.2), with  
 516 branching ratios of approximately 68% and  
 517 32% respectively. All lepton flavors have  
 518 similar branching ratios during a leptonic  $W$   
 519 decay, assuming lepton universality.

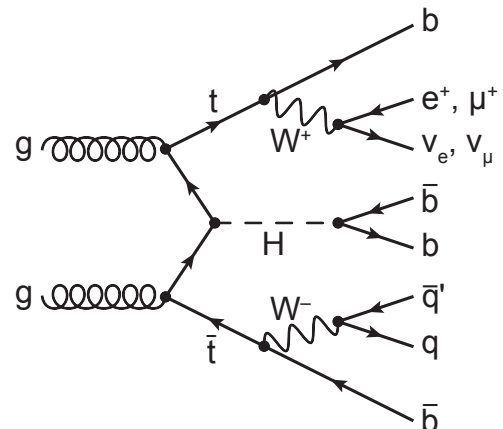


Figure 2.2: Feynman diagram for  $t\bar{t}$  production and subsequent decay processes [55]. Top quark decays into a  $W$ -boson and  $b$ -quarks, and  $W$ -boson can decay to a  $q\bar{q}$  or a  $\ell\nu_\ell$  pair.

## 520 2.1.2 Mathematical formalism

521 The SM can be described within the formalism of quantum field theory (QFT) with the  
522 Lagrangian [56]

$$\mathcal{L}_{\text{SM}} = \mathcal{L}_{\text{QCD}} + \underbrace{(\mathcal{L}_{\text{gauge}} + \mathcal{L}_{\text{fermion}} + \mathcal{L}_{\text{Higgs}} + \mathcal{L}_{\text{Yukawa}})}_{\mathcal{L}_{\text{EW}}} \quad (2.1)$$

523 where  $\mathcal{L}_{\text{QCD}}$  is the QCD term and  $\mathcal{L}_{\text{EW}}$  is the electroweak (EW) term of the Lagrangian.  
524 Formalism of QFT within the SM treats particles as excitations [57] of their corresponding  
525 quantum fields i.e. fermion field  $\psi$ , electroweak boson fields  $W_{1,2,3}$  &  $B$ , gluon fields  $G_\alpha$  and  
526 Higgs field  $\phi$ .

527 The foundation of modern QFT involves gauge theory. A quantum field has gauge sym-  
528 metry if there exists a continuous gauge transformation that when applied to every point in  
529 a field (local gauge transformation) leaves the field Lagrangian unchanged. The set of gauge  
530 transformations of a gauge symmetry is the symmetry group of the field which comes with  
531 a set of generators, each with a corresponding gauge field. Under QFT, the quanta of these  
532 gauge fields are called gauge bosons.

533 The SM Lagrangian is gauge invariant under global Poincaré symmetry and local  $SU(3)_C \times$   
534  $SU(2)_L \times U(1)_Y$  gauge symmetry, with the  $SU(3)_C$  symmetry group corresponding to the  
535 strong interaction and  $SU(2)_L \times U(1)_Y$  to the EW interaction. Global Poincaré symmetry  
536 ensures that  $\mathcal{L}_{\text{SM}}$  satisfies translational symmetry, rotational symmetry and Lorentz boost  
537 frame invariance [58]. These symmetries give rise to corresponding conservation laws, which  
538 lead to conservation of momentum, angular momentum and energy in the SM as a result of  
539 Noether's theorem [59].

540 **2.1.2.1 Quantum chromodynamics**

541     Quantum chromodynamics is a non-Abelian gauge theory i.e. Yang-Mills theory [6, 7]  
 542   describing the strong interaction between quarks in the SM with the gauge group  $SU(3)_C$ ,  
 543   where  $C$  represents conservation of color charge under  $SU(3)_C$  symmetry. According to  
 544   QFT, quarks can be treated as excitations of the corresponding quark fields  $\psi$ . The free Dirac  
 545   Lagrangian for the quark fields  $\mathcal{L}_0 = \bar{\psi}(i\gamma^\mu\partial_\mu - m)\psi$  is invariant under global  $SU(3)$  sym-  
 546   metry, but not under local  $SU(3)_C$  symmetry. To establish invariance under local  $SU(3)_C$   
 547   symmetry, the gauge covariant derivative  $D_\mu$  is defined so that

$$D_\mu\psi = (\partial_\mu - ig_s G_\mu^a T_a)\psi, \quad (2.2)$$

548   where  $g_s = \sqrt{4\pi\alpha_s}$  is the QCD coupling constant,  $G_\mu^a(x)$  are the eight gluon fields, and  
 549    $T_a$  are generators of  $SU(3)_C$ , represented as  $T_a = \lambda_a/2$  with  $\lambda_a$  being the eight Gell-Mann  
 550   matrices [49]. Let the gluon field strength tensors  $G_{\mu\nu}^a$  be

$$G_{\mu\nu}^a \equiv \partial_\mu G_\nu^a - \partial_\nu G_\mu^a - g_s f^{abc} G_\mu^b G_\nu^c, \quad (2.3)$$

551   where  $f^{abc}$  are the structure constants of  $SU(3)_C$ . The gauge invariant QCD Lagrangian  
 552   can then be written as

$$\begin{aligned} \mathcal{L}_{\text{QCD}} &= \bar{\psi}(i\gamma^\mu D_\mu - m)\psi - \frac{1}{4}G_{\mu\nu}^a G_a^{\mu\nu} \\ &= \underbrace{-\frac{1}{4}G_{\mu\nu}^a G_a^{\mu\nu}}_{\text{gluon kinematics}} + \underbrace{\bar{\psi}(i\gamma^\mu\partial_\mu - m)\psi}_{\text{quark kinematics}} + \underbrace{\bar{\psi}^i(g_s\gamma^\mu(T_a)_{ij}G_\mu^a)\bar{\psi}^j}_{\text{quark-gluon interaction}}, \end{aligned} \quad (2.4)$$

553 where  $i, j$  are color indices with integer values from 1 to 3. Gluons are forced to be massless  
 554 from the lack of a gluon mass term to maintain gauge invariance for the Lagrangian.

555 **2.1.2.2 Electroweak theory**

556 The electroweak interaction is the unified description of the weak interaction and electro-  
 557 magnetism under the  $SU(2)_L \times U(1)_Y$  symmetry group, where  $L$  represents the left-handed  
 558 chirality of the weak interaction and  $Y$  represents the weak hypercharge quantum number.  
 559 Fermions can have either left-handed or right-handed chirality with the exception of neutrili-  
 560 nos which can only have left-handed chirality in the SM, and can be divided into left-handed  
 561 doublets and right-handed singlets

$$\psi_L = \begin{pmatrix} \nu_e \\ e_L \end{pmatrix}, \begin{pmatrix} \nu_\mu \\ \mu_L \end{pmatrix}, \begin{pmatrix} \nu_\tau \\ \tau_L \end{pmatrix}, \begin{pmatrix} u_L \\ d_L \end{pmatrix}, \begin{pmatrix} c_L \\ s_L \end{pmatrix}, \begin{pmatrix} t_L \\ b_L \end{pmatrix} \quad (2.5)$$

$$\psi_R = e_R, \mu_R, \tau_R, u_R, d_R, c_R, s_R, t_R, b_R.$$

562 where  $g'$  is the  $B_\mu$  coupling constant and  $B_\mu(x)$  is a vector gauge field that transforms under  
 563  $U(1)_Y$  as

$$B_\mu \rightarrow B_\mu + \frac{1}{g'} \partial_\mu \theta(x). \quad (2.6)$$

564 Right-handed fermion singlets are not affected by  $SU(2)_L$  transformation, so the fermion  
 565 fields  $\psi$  transform under  $SU(2)_L$  as

$$\psi_L \rightarrow e^{i I_3 \vec{\theta}(x) \cdot \vec{\sigma}/2} \psi_L \quad (2.7)$$

$$\psi_R \rightarrow \psi_R.$$

566 where  $\vec{\sigma}/2$  are generators of  $SU(2)_L$  with  $\vec{\sigma}$  being the Pauli matrices. In order to preserve  
 567 local symmetry, the gauge covariant derivative for  $SU(2)_L$  and  $U(1)_Y$  can be defined [60] so

<sup>568</sup> that the gauge covariant derivative for  $SU(2)_L \times U(1)_Y$  can be written as

$$\begin{aligned} D_\mu \psi_L &= \left( \partial_\mu - ig' \frac{Y_L}{2} B_\mu - ig \frac{\sigma_i}{2} W_\mu^i \right) \psi_L \\ D_\mu \psi_R &= \left( \partial_\mu - ig' \frac{Y_R}{2} B_\mu \right) \psi_R. \end{aligned} \quad (2.8)$$

<sup>569</sup> where  $B_\mu(x)$  is a vector gauge field associated with  $U(1)_Y$  and  $W_\mu^i(x)$  ( $i = 1, 2, 3$ ) are three  
<sup>570</sup> vector gauge fields associated with  $SU(2)_L$ . The  $B_\mu$  and  $W_\mu^i$  gauge fields transform under  
<sup>571</sup> their corresponding symmetry groups  $U(1)_Y$  and  $SU(2)_L$  as

$$\begin{aligned} B_\mu &\rightarrow B_\mu + \frac{1}{g'} \partial_\mu \theta(x) \\ W_\mu^i &\rightarrow W_\mu^i + \frac{2}{g} \partial_\mu \theta_a(x) + \epsilon^{ijk} \theta_j(x) W_\mu^k, \end{aligned} \quad (2.9)$$

<sup>572</sup> where  $g'$  is the  $B_\mu$  gauge coupling constant,  $g$  is the  $W_\mu^i$  gauge coupling constants and  $\epsilon^{ijk}$   
<sup>573</sup> is the  $SU(2)_L$  structure constant. Similar to section 2.1.2.1, the kinetic term is added by  
<sup>574</sup> defining field strengths for the four gauge fields

$$\begin{aligned} B_{\mu\nu} &\equiv \partial_\mu B_\nu - \partial_\nu B_\mu \\ W_{\mu\nu}^i &\equiv \partial_\mu W_\nu^i - \partial_\nu W_\mu^i - g e^{ijk} W_\mu^j W_\nu^k. \end{aligned} \quad (2.10)$$

<sup>575</sup> The local  $SU(2)_L \times U(1)_Y$  invariant EW Lagrangian [60] is then

$$\begin{aligned} \mathcal{L}_{\text{EW}} &= i \bar{\psi} (\gamma^\mu D_\mu) \psi - \frac{1}{4} W_{\mu\nu}^i W_i^{\mu\nu} - \frac{1}{4} B_{\mu\nu} B^{\mu\nu} \\ &= \underbrace{i \bar{\psi} (\gamma^\mu \partial_\mu) \psi}_{\text{fermion kinematics}} - \underbrace{\bar{\psi} \left( \gamma^\mu g' \frac{Y}{2} B_\mu \right) \psi}_{\text{fermion-gauge boson interaction}} - \underbrace{\bar{\psi}_L \left( \gamma^\mu g \frac{\sigma_i}{2} W_\mu^i \right) \psi_L}_{\text{boson kinematics \& self-interaction}} - \frac{1}{4} W_{\mu\nu}^i W_i^{\mu\nu} - \frac{1}{4} B_{\mu\nu} B^{\mu\nu}. \end{aligned} \quad (2.11)$$

Under  $\approx 159.5$  GeV, the EW symmetry  $SU(2)_L \times U(1)_Y$  undergoes spontaneous symmetry breaking [61] into  $U(1)_{\text{QED}}$  symmetry, which corresponds to a separation of the weak and electrodynamic forces. Electroweak spontaneous symmetry breaking replaces the four massless and similarly-behaved EW gauge bosons  $B_\mu$  and  $W_\mu^i$  with the EM boson  $\gamma$  and the weak bosons  $Z/W^\pm$ , as well as giving the  $Z$  and  $W^\pm$  bosons masses via the Higgs mechanism. This is due to a specific choice of gauge for the Higgs field leading to the reparameterization of the EW bosons  $B_\mu$  and  $W_\mu^i$  to  $W^\pm/Z/\gamma$  using the relations

$$\begin{aligned}
 W_\mu^\pm &\equiv \frac{1}{\sqrt{2}} (W_\mu^1 \mp iW_\mu^2) \\
 \begin{pmatrix} A_\mu \\ Z_\mu \end{pmatrix} &\equiv \begin{pmatrix} \cos \theta_W & \sin \theta_W \\ -\sin \theta_W & \cos \theta_W \end{pmatrix} \begin{pmatrix} B_\mu \\ W_\mu^3 \end{pmatrix}
 \end{aligned} \tag{2.12}$$

where  $\theta_W \equiv \cos^{-1} (g/\sqrt{g^2 + g'^2})$  is the weak mixing angle. The boson kinetic term can also be refactorized to extract cubic (three vertices) and quartic (four vertices) self-interactions among the gauge bosons [60]. The Lagrangian can then be rewritten as

$$\begin{aligned}
 \mathcal{L} = & \underbrace{eA_\mu \bar{\psi} (\gamma^\mu Q) \psi}_{\text{electromagnetism}} + \underbrace{\frac{e}{2\sin \theta_W \cos \theta_W} \bar{\psi} \gamma^\mu (v_f - a_f \gamma_5) \psi Z_\mu}_{\text{neutral current interaction}} \\
 & + \underbrace{\frac{g}{2\sqrt{2}} \sum_{\psi_L} [\bar{f}_2 \gamma^\mu (1 - \gamma_5) f_1 W_\mu^+ + \bar{f}_1 \gamma^\mu (1 - \gamma_5) f_2 W_\mu^-]}_{\text{charged current interaction}} \\
 & + \underbrace{\mathcal{L}_{\text{kinetic}} + \mathcal{L}_{\text{cubic}} + \mathcal{L}_{\text{quartic}}}_{\text{boson self-interaction}}
 \end{aligned} \tag{2.13}$$

where  $\gamma_5 = i\gamma^0\gamma^1\gamma^2\gamma^3$  is the chirality projection operator,  $a_f = I_3$ ,  $v_f = I_3(1 - 4|Q|\sin^2 \theta_W)$  and  $f_1, f_2$  are up and down type fermions of a left-handed doublet.

588    **2.1.2.3 Higgs mechanism**

589    So far, the EW bosons are massless since the mass terms  $-m\bar{\psi}\psi$  for fermions and  
 590     $-mA^\mu A_\mu$  for bosons are not invariant under the EW Lagrangian symmetries. The parti-  
 591    cles must then acquire mass under another mechanism. The Brout-Engler-Higgs mechanism  
 592    [11–13] was introduced in 1964 to rectify this issue and verified in 2012 with the discovery  
 593    of the Higgs boson [20, 21].

594    The Higgs potential is expressed as

$$V(\phi^\dagger \phi) = \mu^2 \phi^\dagger \phi + \lambda (\phi^\dagger \phi)^2 \quad (2.14)$$

595    where  $\mu^2$  and  $\lambda > 0$  are arbitrary parameters, and the  $SU(2)_L$  doublet  $\phi = \begin{pmatrix} \phi^+ \\ \phi^0 \end{pmatrix}$  is the Higgs  
 596    field with complex scalar fields  $\phi^+$  and  $\phi^0$  carrying +1 and 0 electric charge respectively.

597    The Lagrangian for the scalar Higgs field is

$$\mathcal{L}_H = (\partial_\mu \phi)^\dagger (\partial^\mu \phi) - V(\phi^\dagger \phi). \quad (2.15)$$

598    Since the potential  $V(\phi^\dagger \phi)$  is constrained by  $\lambda > 0$ , the ground state is solely controlled by  
 599     $\mu$ . If  $\mu^2 > 0$ , the ground state energy is  $\phi = 0$ , and the EW bosons would remain massless.  
 600    If  $\mu^2 < 0$ , the ground state is

$$|\phi|^2 = -\frac{\mu^2}{2\lambda} \equiv \frac{v^2}{\sqrt{2}}, \quad (2.16)$$

601    where  $v$  is defined as the vacuum expectation value (VEV). The standard ground state for  
 602    the Higgs potential without loss of generality can be chosen as  $\phi(0) = 1/\sqrt{2}(0)_v$ .

603    Having  $U(1)$  symmetry allows any  $-e^{i\theta} \sqrt{\mu^2/\lambda}$  to be a ground state energy for the Higgs

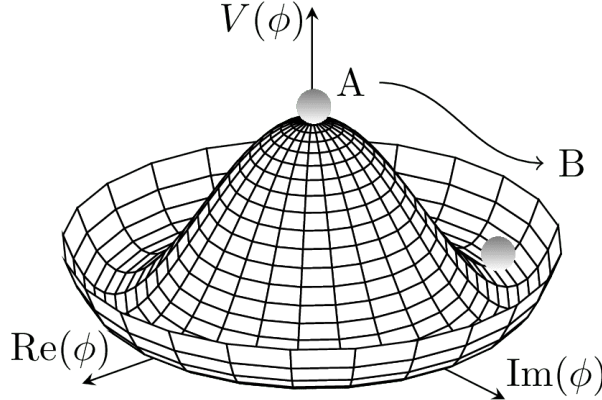


Figure 2.3: Illustration of a common representation of the Higgs potential [62]. Before SSB, the ground state  $\phi(0)$  is located at A which is symmetric with respect to the potential. A perturbation to this state fixes the ground state energy  $|\phi(0)|^2$  to a particular value at B, "spontaneously" breaking the symmetry and degeneracy in  $|\phi(0)|^2$ .

604 Lagrangian. This degeneracy results in spontaneous symmetry breaking of the  $SU(2)_L \times$   
 605  $U(1)_Y$  symmetry into  $U(1)_{\text{EM}}$  symmetry when the Higgs field settles on a specific vacuum  
 606 state as a result of a perturbation or excitation (Figure 2.3). The spontaneous symmetry  
 607 breaking introduces three massless (Nambu-Goldstone [63]) vector gauge boson  $\xi$  and a  
 608 massive scalar boson  $\eta$ , each corresponds to a generator of the gauge group. The vector field  
 609 for  $\xi$  and  $\eta$  are real fields parameterized as  $\xi \equiv \phi^+ \sqrt{2}$  and  $\eta \equiv \phi^0 \sqrt{2} - v$  [64]. The Higgs  
 610 field now becomes

$$\phi = \frac{v + \eta + i\xi}{\sqrt{2}} = \frac{1}{\sqrt{2}} e^{i\xi} \begin{pmatrix} 0 \\ v + \eta \end{pmatrix}. \quad (2.17)$$

611 Due to  $U(1)_{\text{EM}}$  invariance, a unitary gauge with the transformation  $\phi \rightarrow \exp(-i\xi \cdot) \frac{\sigma}{2v}$  can  
 612 be chosen for the Higgs field to eliminate the massless bosons and incorporate them into the  
 613 EM/weak bosons via Equation 2.12. This leaves the massive  $\eta$  which can now be observed as  
 614 an excitation of the Higgs field from the standard ground state and must be the Higgs boson  
 615  $h$ . Using the EW covariant derivative from Equation 2.8, the Higgs Lagrangian around the

616 vacuum state becomes

$$\begin{aligned}\mathcal{L}_H &= (D_\mu \phi)^\dagger (D^\mu \phi) - \mu^2 \left( \frac{v+h}{\sqrt{2}} \right)^2 - \lambda \left( \frac{v+h}{\sqrt{2}} \right)^4 \\ &= (D_\mu \phi)^\dagger (D^\mu \phi) - \frac{1}{2} \mu^2 h^2 - \lambda v h^3 - \frac{\lambda}{4} h^4 - \dots\end{aligned}\tag{2.18}$$

617 The Higgs mass can be extracted from the quadratic term as  $m_H = \sqrt{-2\mu^2}$ . The kinetic

618 term in the Lagrangian can be written as

$$\begin{aligned}(D_\mu \phi)^\dagger (D^\mu \phi) &= \frac{1}{2} (\partial_\mu h)^2 + \frac{g^2}{8} (v+h)^2 \left| W_\mu^1 - i W_\mu^2 \right|^2 + \frac{1}{8} (v+h)^2 (g' W_\mu - g B_\mu) \\ &= \frac{1}{2} (\partial_\mu h)^2 + (v+h)^2 \left( \frac{g^2}{4} W_\mu^+ W^{-\mu} + \frac{1}{8} (g^2 + g'^2) Z_\mu^0 Z^{0\mu} \right).\end{aligned}\tag{2.19}$$

619 Masses for the EW bosons can be extracted from the quadratic terms

$$m_{W^\pm} = \frac{v}{2} g, \quad m_Z = \frac{v}{2} \sqrt{g^2 + g'^2}, \quad m_\gamma = 0.\tag{2.20}$$

620 However, the fermion mass term  $-m\bar{\psi}\psi$  still breaks EW invariance after spontaneous symmetry breaking. Instead, fermions acquire mass by replacing the mass term with a gauge invariant Yukawa term in the EW Lagrangian representing fermions' interactions with the Higgs field [64]

$$\begin{aligned}\mathcal{L}_{\text{Yukawa}} &= -c_f \frac{v+h}{\sqrt{2}} (\bar{\psi}_R \psi_L + \bar{\psi}_L \psi_R) \\ &= -\underbrace{\frac{c_f}{\sqrt{2}} v (\bar{\psi} \psi)}_{\text{fermion mass}} - \underbrace{\frac{c_f}{\sqrt{2}} (h \bar{\psi} \psi)}_{\text{fermion-Higgs interaction}},\end{aligned}\tag{2.21}$$

624 where  $c_f$  is the fermion-Higgs Yukawa coupling. The fermion mass is then  $m_f = c_f v / \sqrt{2}$ .

## 625 2.2 Beyond the Standard Model: $t\bar{t}Z' \rightarrow t\bar{t}t\bar{t}$

626 This analysis uses the  $t\bar{t}t\bar{t}$  final state signal signature to search for the existence of a heavy  
627 neutral BSM resonance that couples strongly to the top quark, nominally named  $Z'$ . Cross-  
628 section for  $t\bar{t}t\bar{t}$  production can be enhanced by many possible BSM models, in particular  
629 production of heavy scalars and pseudoscalar bosons predicted in Type-II two-Higgs-doublet  
630 models (2HDM) [39–43] or possible production of a heavy neutral resonance boson  $Z'(\rightarrow t\bar{t})$   
631 in association with a  $t\bar{t}$  pair [65, 66]. The  $t\bar{t}Z'$  production mode and consequently  $t\bar{t}t\bar{t}$  signal  
632 signature can provide a more sensitive channel for searches by avoiding contamination from  
633 the large SM  $gg \rightarrow t\bar{t}$  background in an inclusive  $Z' \rightarrow t\bar{t}$  search.

### 634 2.2.1 Top-philic vector resonance

635 Many BSM models extend the SM by adding to the SM gauge group additional  $U(1)'$   
636 gauge symmetries [67, 68], each with an associated vector gauge boson ( $Z'$ ). In the case of  
637 a BSM global symmetry group with rank larger than the SM gauge group, the symmetry  
638 group can spontaneously break into  $G_{\text{SM}} \times U(1)'^n$ , where  $G_{\text{SM}}$  is the SM gauge group  
639  $SU(3)_C \times SU(2)_L \times U(1)_Y$  and  $U(1)'^n$  is any  $n \geq 1$  number of  $U(1)'$  symmetries. The  
640 existence of additional vector boson(s)  $Z'$  would open up many avenues of new physics e.g.  
641 extended Higgs sectors from  $U(1)'$  symmetry breaking [69, 70], existence of flavor-changing  
642 neutral current (FCNC) mediated by  $Z'$  [71], and possible exotic production from heavy  $Z'$   
643 decays [72].

644 Due to the top quark having the largest mass out of all known elementary particles in the  
645 SM, many BSM models [38–43, 73, 74] predict ‘top-philic’ vector resonances that have much  
646 stronger coupling to the top quark compared to other quarks. Previous BSM  $t\bar{t}t\bar{t}$  search for

647 top-philic resonances [28] with a similar model in the single-lepton final state and similar  
 648 mass ranges set upper limits on observed (expected)  $Z'$  production cross section between 21  
 649 (14) fb to 119 (86) fb depending on parameter choice. This analysis is also motivated by the  
 650 recent observation of SM  $t\bar{t}t\bar{t}$  production in the same-sign multilepton (SSML) channel by  
 651 ATLAS [44] and CMS [75] at  $6.1\sigma$  and  $5.6\sigma$  discovery significance respectively.

652 A simplified top-philic color-singlet vector particle model [45, 73] is employed in the  
 653 search. The interaction Lagrangian assumes the  $Z'$  couples dominantly the top quark and  
 654 has the form

$$\begin{aligned}
 \mathcal{L}_{Z'} &= \bar{t}\gamma_\mu (c_L P_L + c_R P_R) t Z'^\mu \\
 &= c_t \bar{t}\gamma_\mu (\cos\theta P_L + \sin\theta P_R) t Z'^\mu,
 \end{aligned} \tag{2.22}$$

655 where  $c_t = \sqrt{c_L^2 + c_R^2}$  is the  $Z'$ -top coupling strength,  $P_{L/R} = (1 \mp \gamma_5)/2$  are the chirality  
 656 projection operators, and  $\theta = \tan^{-1}(c_R/c_L)$  is the chirality mixing angle. Expanding the  
 657 Lagrangian results in

$$\mathcal{L}_{Z'} = \frac{1}{\sqrt{2}} \bar{t}\gamma_\mu \left[ \sin\left(\theta + \frac{\pi}{4}\right) - \left( \sqrt{2} \cos\left(\theta + \frac{\pi}{4}\right) \right) \gamma_5 \right] t Z'^\mu, \tag{2.23}$$

658 which bears striking resemblance to the EW Lagrangian neutral current interaction term in  
 659 Equation 2.13, showing the similarity between the  $Z'$  and the  $Z$  boson that acquires mass  
 660 from  $SU(2)_L \times U(1)_Y$  spontaneous symmetry breaking. Assuming the  $Z'$  mass  $m_{Z'}$  is much  
 661 larger than the top mass ( $m_t^2/m_{Z'}^2 \approx 0$ ), the  $Z'$  decay width at leading-order (LO) can be  
 662 approximated as

$$\Gamma(Z' \rightarrow t\bar{t}) \approx \frac{c_t^2 m_{Z'}}{8\pi}. \tag{2.24}$$

663 It can be observed that  $\Gamma/m_{Z'} \approx c_t^2/8\pi \ll 1$  for  $c_t \approx 1$ , which suggests a very narrow and

664 well-defined resonance peak, validating the narrow-width approximation for the choice of

665  $c_t = 1$ .

## 666 2.2.2 Production channels

667 The main production channels for the aforementioned heavy topophilic color singlet  $Z'$

668 are at tree level and loop level, with the one-loop level being the dominant processes [45].

669 Loop level processes are dependent on the chirality angle  $\theta$ , where  $\theta = \pi/4$  suppresses all

670 but gluon-initiated box sub-processes. To minimize model dependence, only the tree level

671 production was considered for this analysis by choosing  $\theta = \pi/4$ . Figure 2.4 illustrates

672 several tree level  $Z'$  production processes.

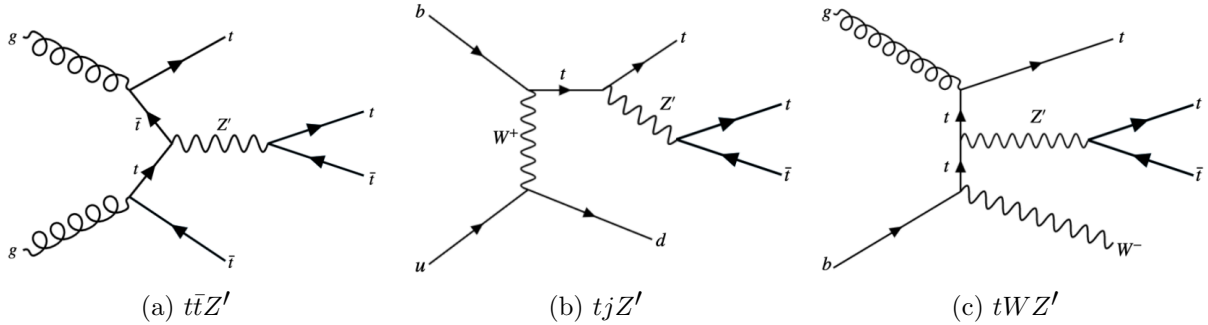


Figure 2.4: Feynman diagrams for tree level  $Z'$  production in association with (a)  $t\bar{t}$ , (b)  $tj$  (light quark) and (c)  $tW$ , decaying to final states containing (a)  $t\bar{t}t\bar{t}$  or (b)(c)  $t\bar{t}t$  [45].

673 The tree level  $t\bar{t}$ -associated process  $t\bar{t}Z'$  is the targeted production channel for the search

674 in this dissertation. Contributions from the single-top-associated channels  $tjZ'$  and  $tWZ'$

675 are not considered due to a smaller cross-section by a factor of two compared to  $t\bar{t}Z'$  due

676 to suppression in the three-body phase space [45]. Additionally,  $t\bar{t}Z' \rightarrow t\bar{t}t\bar{t}$  production is

677 independent of  $\theta$  while  $tjZ'$  and  $tWZ'$  are minimally suppressed under pure left-handed

678 interactions ( $\theta = 0$ ) and maximally suppressed under pure right-handed interactions ( $\theta =$

679  $\pi/2$ ); both channels are affected by the choice of  $\theta = \pi/4$  to suppress loop level production.

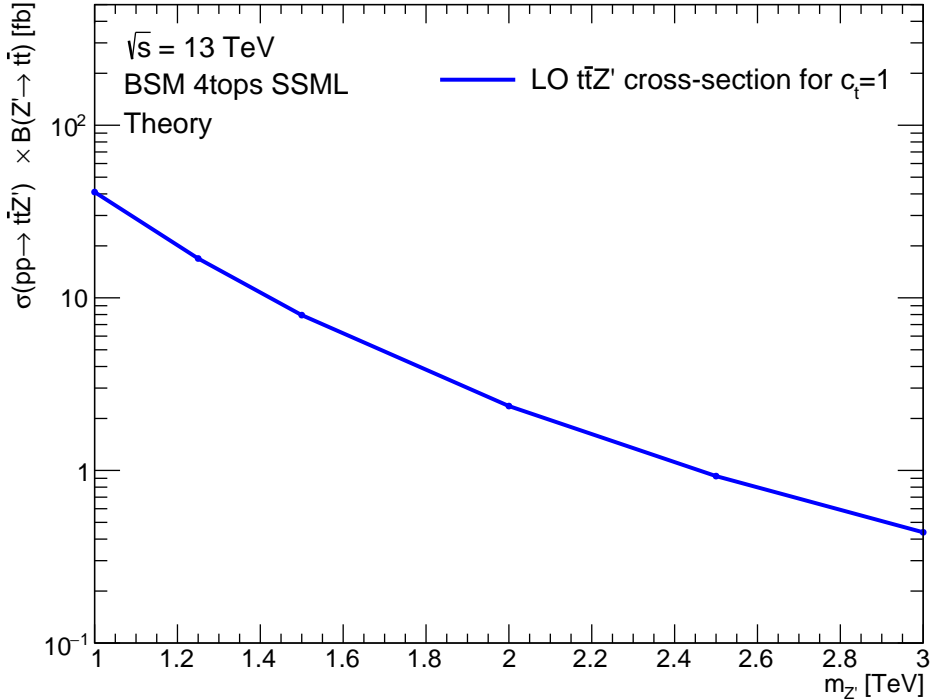


Figure 2.5: Theoretical  $t\bar{t}Z'$  production cross-section times  $Z' \rightarrow t\bar{t}$  branching ratio as a function of the  $Z'$  mass at LO in QCD coupling to top with  $c_t = 1$  under a simplified topophilic model [45, 73, 76].

### 680 2.2.3 Decay modes

681 The different  $W$  boson decay modes shown in Figure 2.2 result in many different final  
 682 states for  $t\bar{t}Z'/t\bar{t}t\bar{t}$  decay, which can each be classified into one of three channels shown in  
 683 Figure 2.6: all hadronic decays; exactly one lepton or two opposite-sign leptons (1LOS);  
 684 exactly two same-sign leptons or three or more leptons (SSML). The branching ratio for  
 685 each channel is shown in Figure 2.6. The all hadronic and 1LOS channels have much larger  
 686 branching ratios compared to SSML channel but suffer heavily from  $gg \rightarrow t\bar{t}$  background  
 687 contamination, giving the SSML channel better sensitivity at the cost of lower statistics.  
 688 This is also the targeted channel for this analysis.

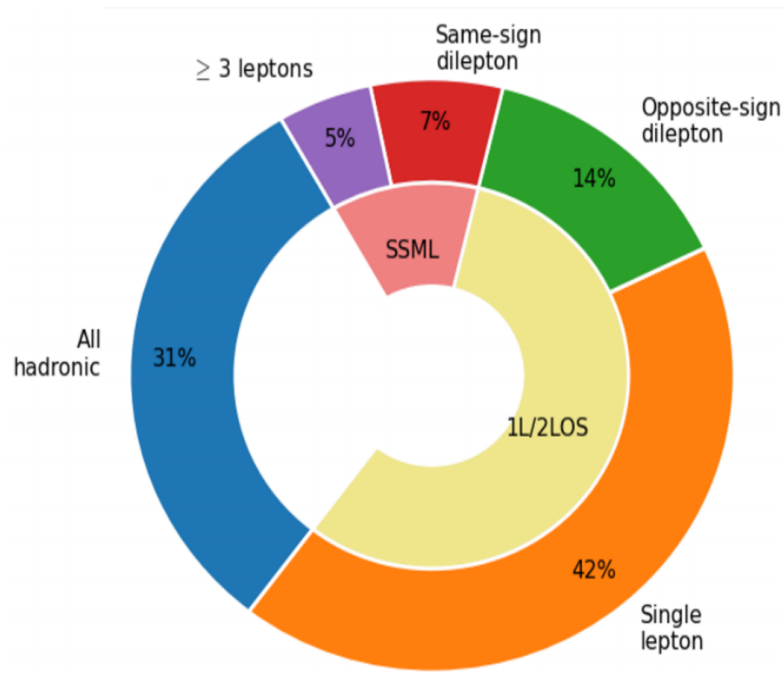


Figure 2.6: Branching ratios for  $t\bar{t}t\bar{t}$  decay [77]. The same-sign dilepton and multilepton channels together forms the SSML channel.

# 689 Chapter 3. LHC & ATLAS Experiment

## 690 3.1 The Large Hadron Collider

691 Predictions from theoretical models are evaluated against experimental data collected  
692 from particle detectors. This chapter provides a detailed overview of the Large Hadron  
693 Collider (LHC) and the ATLAS detector, one of the key experiments designed to study  
694 high-energy collisions at the LHC.

### 695 3.1.1 Overview

696 The Large Hadron Collider [78] (LHC) is currently the world's largest particle collider  
697 with a circumference of almost 27 km. Built by CERN on the border of Switzerland and  
698 France, the LHC is designed as a particle collider for proton-proton ( $pp$ ), sometimes heavy  
699 ions i.e. lead-lead (PbPb) and proton-lead ( $pPb$ ) beams at TeV-scale energies. Two beams  
700 of particles are injected into the LHC in opposite directions and allowed to collide at the  
701 center of four major experiments:

- 702 • **A Toroidal LHC ApparatuS** (ATLAS) [27] and **Compact Muon Solenoid** (CMS)  
703 [79]: multi-purpose detectors, designed to target a variety of phenomena including SM,  
704 BSM and heavy-ion physics.
- 705 • **Large Ion Collider Experiment** (ALICE) [80]: specialized detector to record ion  
706 collisions and study heavy-ion physics.
- 707 • **Large Hadron Collider beauty** (LHCb) [81]: detector dedicated to study properties  
708 of  $b$ -quarks and  $b$ -hadrons.

709      Aside from the four major experiments, the LHC also houses smaller experiments e.g.  
 710     AWAKE [82], FASER [83], KATRIN [84], that either share an interaction point with one of  
 711     the above experiments or make use of particle beams pre-LHC injection.

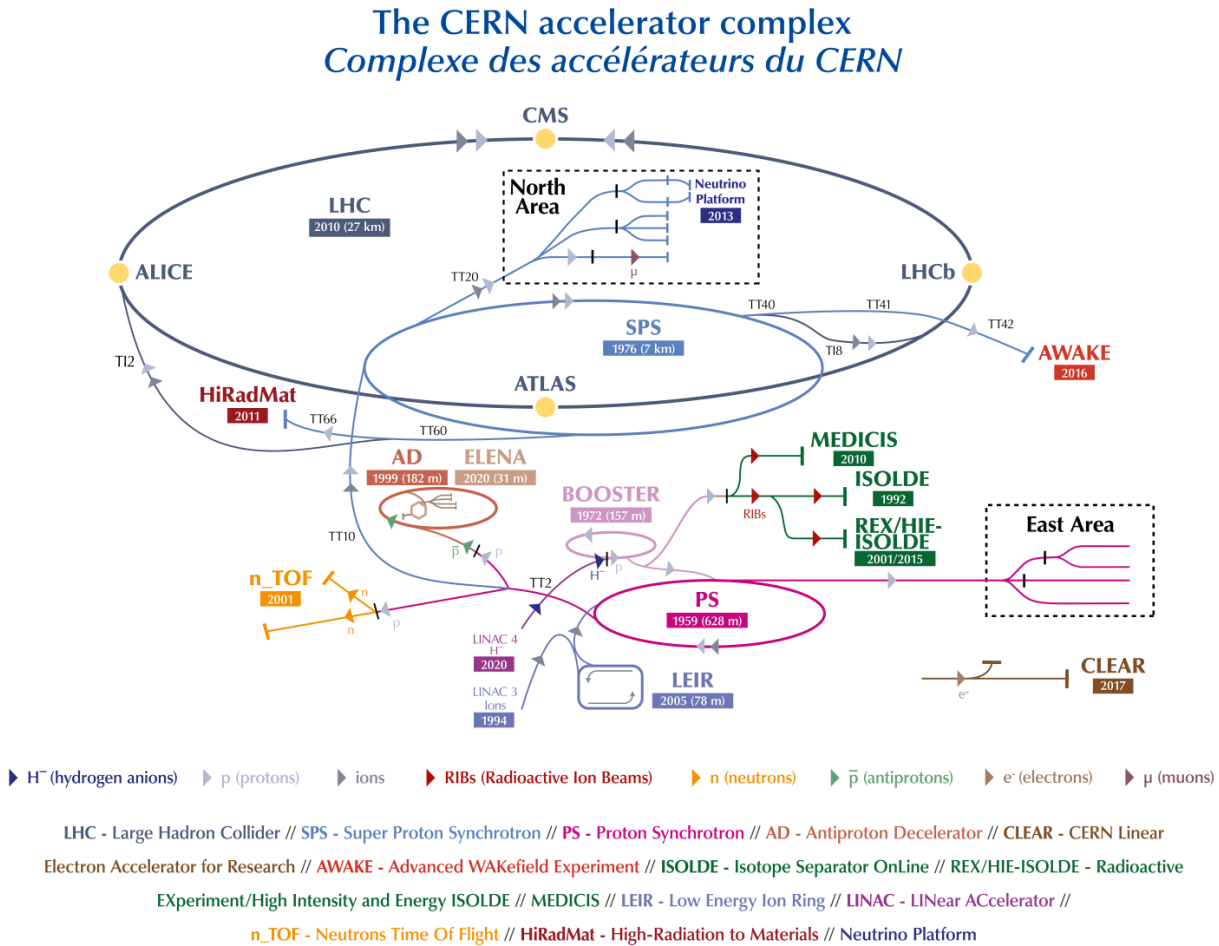


Figure 3.1: The full CERN accelerator complex as of 2022 [85].

712      The majority of the LHC operational time is dedicated to studying  $pp$  collisions of up to  
 713      $\sim 13$  TeV center-of-mass energy, denoted as  $\sqrt{s}$ . Reaching collision energy requires a sequence  
 714     of accelerators within the CERN accelerator complex, shown in Figure 3.1. Proton produc-  
 715     tion starts at LINAC 4, where hydrogen atoms are accelerated to 160 MeV then stripped  
 716     of electrons. The leftover proton beams are injected into the Proton Synchrotron Booster

717 (PSB) and accelerated to 2 GeV before being transferred into the Proton Synchrotron (PS).  
 718 Here, the beams are ramped up to 26 GeV then injected into the Super Proton Synchrotron  
 719 (SPS) to further raise the energy threshold to 450 GeV. The beams are finally injected into  
 720 the LHC in opposite directions, continuously increasing in energy up to 6.5 TeV per beam,  
 721 reaching the 13 TeV center-of-mass energy threshold necessary for collision during Run 2.  
 722 As of the start of Run 3 in 2022, proton beams can now be ramped up to 6.8 TeV per beam  
 723 for a total of  $\sqrt{s} = 13.6$  TeV.

### 724 3.1.2 LHC operations

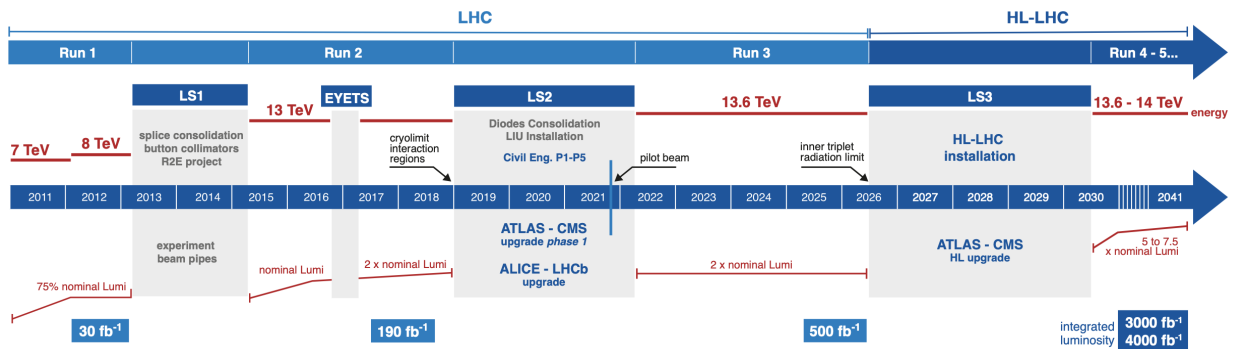


Figure 3.2: Current and future timeline of LHC operations with corresponding center-of-mass energies and projected integrated luminosities. [86].

725 Operations at the LHC are defined in periods of data-taking and shut-down known as  
 726 runs and long shutdowns respectively; the first period (Run 1) started with first collisions  
 727 at the LHC in 2010 at  $\sqrt{s} = 7$  TeV [87]. Upgrades are usually carried out for detectors and  
 728 accelerators during long shutdowns, raising the maximum energy threshold in preparation  
 729 for the next run. An overview of the LHC runtime and corresponding center-of-mass energies  
 730 are summarized in Figure 3.2. During Run 2 from 2015-2018, the ATLAS detector recorded  
 731 a total of  $1.1 \times 10^{16}$   $pp$  collisions at  $\sqrt{s} = 13$  TeV, which corresponds to an integrated

732 luminosity of  $140 \pm 0.83\% \text{ fb}^{-1}$  that passed data quality control and are usable for analyses  
733 [88]. This is also the data set used for the analysis in this dissertation.

### 734 3.1.3 Physics at the LHC

735 The majority of physics studied at the LHC focus primarily on QCD proton-proton hard  
736 scattering processes and the resulting products. Hard scattering processes involve large  
737 momentum transfer compared to the proton mass e.g. top pair production ( $gg \rightarrow t\bar{t}$ ) and  
738 Higgs production ( $gg \rightarrow H$ ), and can be predicted using perturbative QCD [89]. Hard  
739 processes probe distance scales much lower than the proton radius and can be considered  
740 collisions between the constituent quarks and gluons i.e. partons. Soft processes involve  
741 lower momentum transfer between partons and are dominated by less well-understood non-  
742 perturbative QCD effects. The hard interaction between two partons are represented by a  
743 parton distribution function (PDF)  $f_i(x, Q^2)$ , which describes the probability of interacting  
744 with a constituent parton  $i$  that carries a fraction  $x$  of the external hadron's momentum  
745 when probed at a momentum scale of  $Q^2$  [90]. Other partons within the hadron that did  
746 not participate in the collision can still interact via lower momentum underlying-events  
747 (UE). The probability of a particular interaction occurring is defined as its cross-section  
748  $\sigma[b]$ . Figure 3.3 gives an overview of SM processes produced within the LHC and their  
749 cross-sections.

## 750 3.2 The ATLAS detector

751 One of the four main experiments at the LHC is ATLAS [27], designed as a multi-purpose  
752 detector for the role of studying high-energy physics in  $pp$  and heavy-ion collisions. ATLAS

## Standard Model Production Cross Section Measurements

Status: October 2023

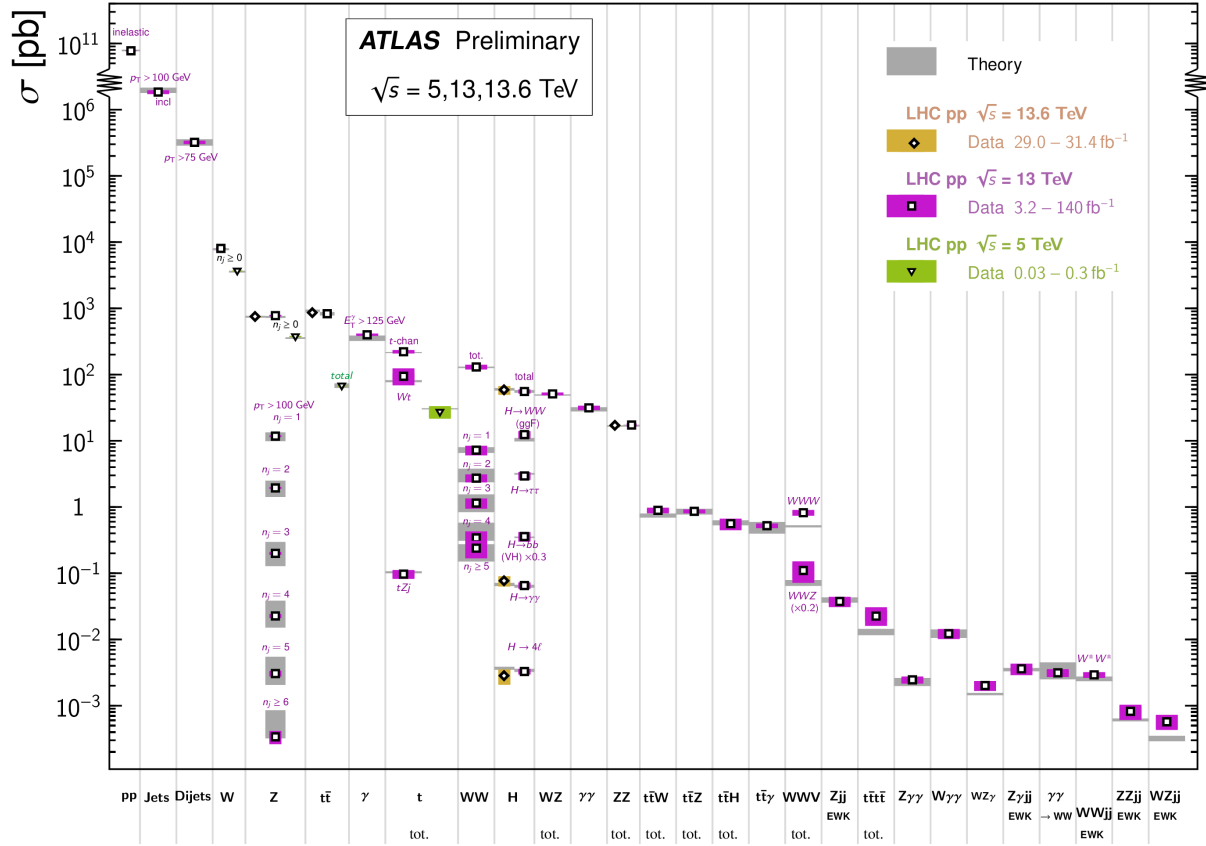


Figure 3.3: Summary of predicted and measured cross-section for SM processes at the LHC at different center-of-mass energies [91].

753 is a detector with symmetric cylindrical geometry with dimensions of 44 m in length and 25  
 754 m in diameter, covering a solid angle of almost  $4\pi$  around the collision point. The detector is  
 755 built concentrically around the beamline with the collision point at the center to maximally  
 756 capture signals produced by interactions. Figure 3.4 shows a slice of the ATLAS detector.  
 757 From the inside out, the main ATLAS subdetector system consists of the inner detector  
 758 (ID), calorimeter systems (electromagnetic and hadronic) and the muon spectrometer (MS).  
 759 The ATLAS detector uses a right-handed coordinate system [27] designed to align with  
 760 the geometry of a collision interaction, with the origin set at the interaction point, the  $z$ -axis

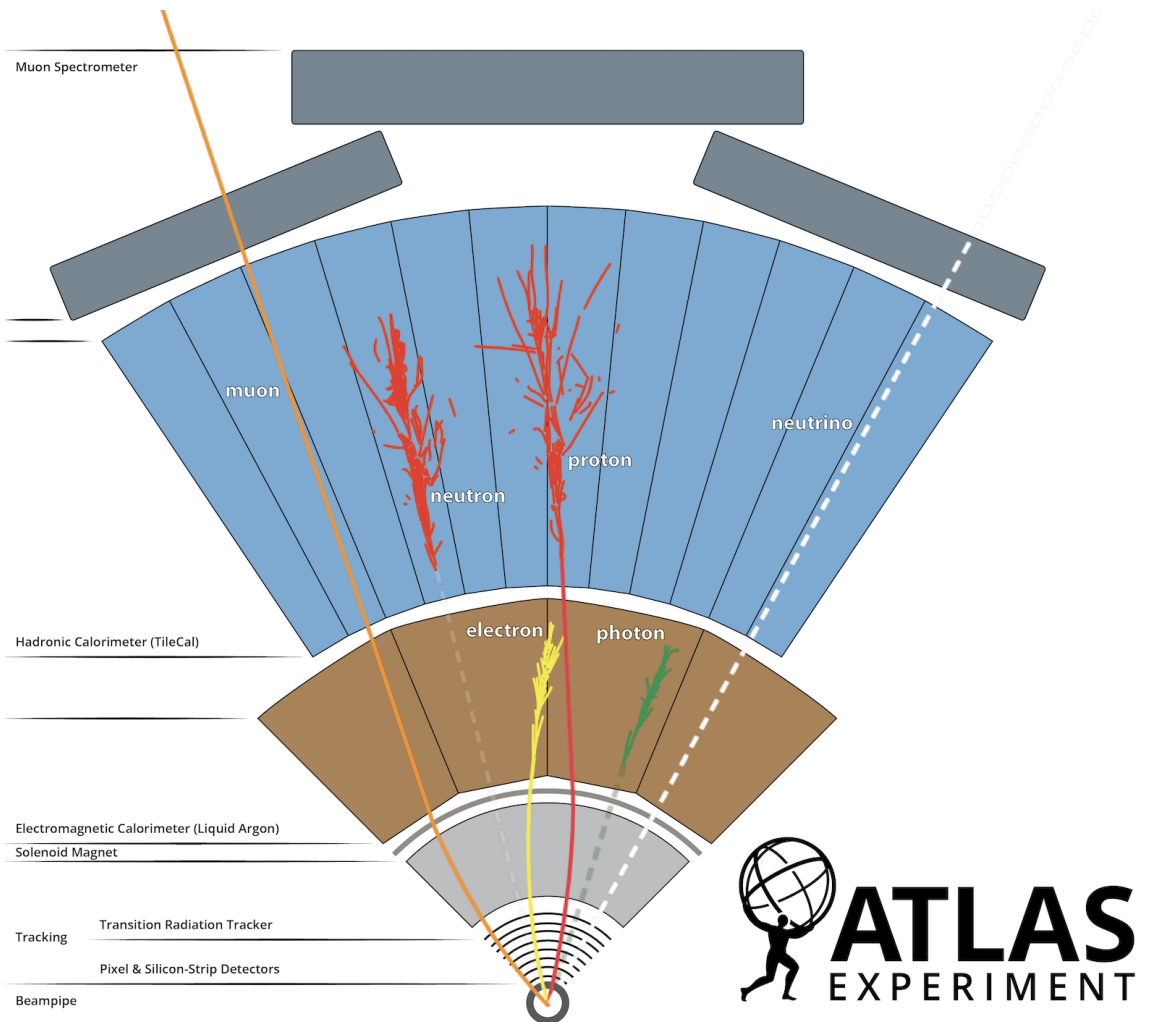


Figure 3.4: A cross section slice of the ATLAS detector showing different subsystems along with visualization of different types of particles traveling through the detector [92].

761 following (either of) the beamline and the  $x$ -axis pointing towards the center of the LHC  
 762 ring. In cylindrical coordinates, the polar angle  $\theta$  is measured from the beam axis, and  
 763 the azimuthal angle  $\phi$  is measured along the transverse plane ( $xy$ -plane) starting at the  $x$ -  
 764 axis. Additional observables are defined for physics purposes: the pseudorapidity defined as  
 765  $\eta = -\ln \tan(\theta/2)$ ; angular distance within the detector defined as  $\Delta R = \sqrt{\Delta\eta^2 + \Delta\phi^2}$ ; and  
 766 transverse momentum  $p_T$  (transverse energy  $E_T$ ) defined as the component of the particle's  
 767 momentum (energy) projected onto the transverse plane.

### 768 3.2.1 Inner detector

769 The innermost part of ATLAS is the inner detector (ID) [27], constructed primarily for  
770 the purpose of measuring and reconstructing charged tracks within the  $|\eta| < 2.5$  region with  
771 high momentum resolution ( $\sigma_{p_T}/p_T = 0.05\% \pm 1\%$ ). Figure 3.5 shows the composition of  
772 the ID with three subsystems, the innermost being the pixel detector, then Semiconductor  
773 Tracker (SCT), and the Transition Radiation Tracker (TRT) on the outermost layer; all of  
774 which are surrounded by a solenoid magnet providing a magnetic field of 2 T.

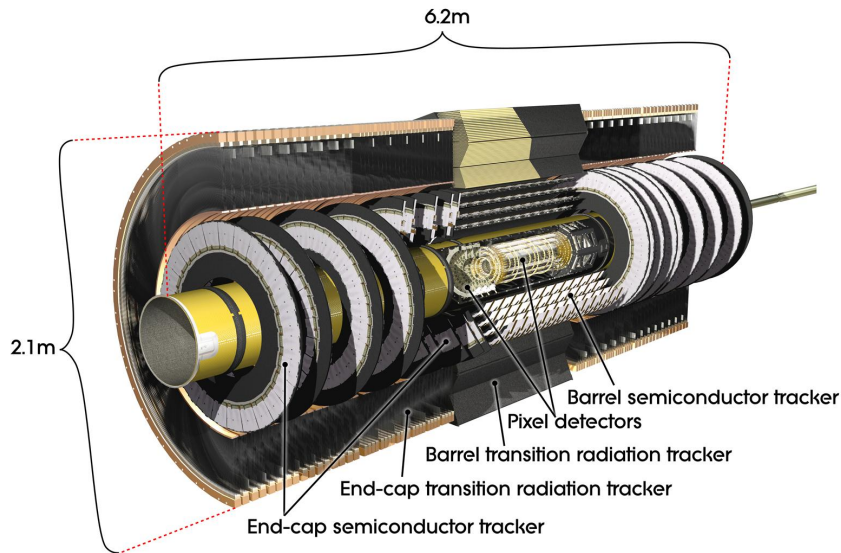


Figure 3.5: Cutaway illustration of the inner detector along with its subsystems [93].

### 775 Pixel detector

776 The pixel detector subsystem [27] consists of 250  $\mu\text{m}$  silicon semiconductor pixel layers  
777 with about 80.4 million readout channels, reaching a spatial resolution of 10  $\mu\text{m}$  in the  
778  $R - \phi$  (transverse) plane and 115  $\mu\text{m}$  in the  $z$ -direction for charged tracks. Charged particles  
779 passing through the pixel detector ionize the silicon layers and produce electron-hole pairs;

780 the electrons drift towards the detector's electrode under an applied electric field and the  
781 resulting electric signals are collected in read-out regions. The pixel detector is used primarily  
782 for impact parameter measurement, pile-up suppression, vertex finding and seeding for track  
783 reconstruction.

#### 784 Semiconductor Tracker

785 The Semiconductor Tracker (SCT) [27] functions similarly to the pixel detector, using  
786 silicon semiconductor microstrips totaling about 6.3 million read-out channels, reaching a  
787 per layer resolution of 17  $\mu\text{m}$  in the  $R\text{-}\phi$  plane and 580  $\mu\text{m}$  in the  $z$ -direction [27]. The  
788 SCT plays an important role in precise  $p_{\text{T}}$  measurement of charged particles as well as track  
789 reconstruction.

#### 790 Transition Radiation Tracker

791 The outermost layer of the ID, the Transition Radiation Tracker (TRT) [27], consists of  
792 layers of 4 mm diameter straw tubes filled with a xenon-based gas mixture and a 30  $\mu\text{m}$   
793 gold-plated wire in the center. The TRT contains a total of about 351 thousand readout  
794 channels with a resolution of 130  $\mu\text{m}$  for each straw tube in the  $R\text{-}\phi$  plane, and provides  
795 extended track measurement, particularly estimation of track curvature under the solenoidal  
796 magnetic field. Importantly, the TRT also serves to identify electrons through absorption of  
797 emitted transition-radiation within the Xe-based gas mixture.

### 798 3.2.2 Calorimeter systems

799 Surrounding the ID is the ATLAS calorimeter system [27] with electromagnetic (EM) and  
800 hadronic calorimeters, covering a range of  $|\eta| < 4.9$ . The calorimeters are sampling calorime-

801 ters with alternating absorbing layers to stop incoming particles and active layers to collect  
 802 read-out signals from energy deposits. Incoming particles passing through the calorimeters  
 803 interact with the absorbing layers, producing EM or hadronic showers of secondary particles.  
 804 The particle showers deposit energy in the corresponding layer of the calorimeters, which  
 805 are collected and aggregated to identify and reconstruct the original particle's energy and  
 806 direction. Figure 3.6 shows a schematic overview of the ATLAS calorimeter system.

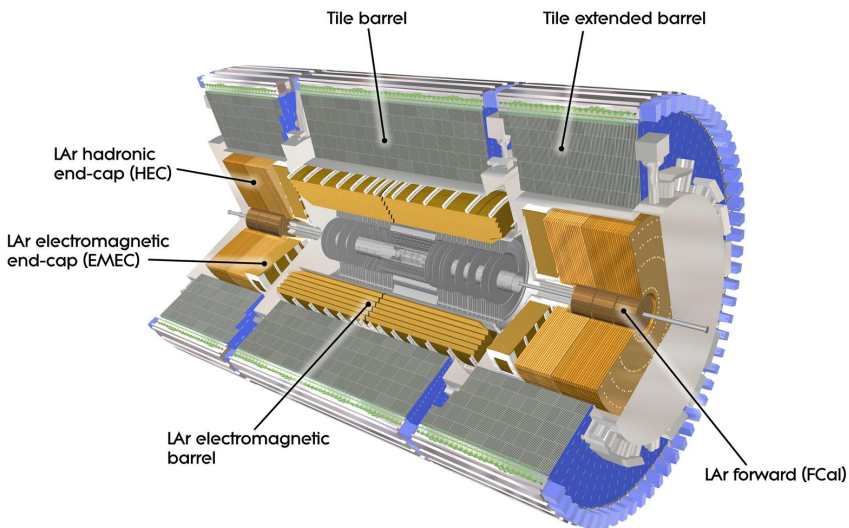


Figure 3.6: Cutaway illustration of the calorimeter system including the EM, hadronic and LAr forward calorimeters [94].

## 807 Electromagnetic calorimeter

808 The EM calorimeter [27] covers the innermost part of the calorimeter system, with lead  
 809 (Pb) absorbing layers and liquid argon (LAr) active layers to capture the majority of electrons  
 810 and photons exiting the ID. The EM calorimeter is divided into regions depending on  $\eta$   
 811 coverage: a barrel region ( $|\eta| < 1.475$ ), two endcap regions ( $1.375 < |\eta| < 3.2$ ) and a  
 812 transition region ( $1.372 < |\eta| < 1.52$ ). The endcap calorimeters are further divided into an

813 outer wheel region ( $1.372 < |\eta| < 2.5$ ) and an inner wheel region ( $2.5 < |\eta| < 3.2$ ) in order  
814 to provide precise coverage within the same  $\eta$  range as the ID. Overlap between the barrel  
815 and endcap regions compensates for the lower material density in the transition region.

816 **Hadronic calorimeter**

817 The hadronic calorimeter [27] covers up to  $|\eta| < 4.9$  and is comprised of three parts: the  
818 tile calorimeter with a barrel region ( $|\eta| < 1.0$ ) and extended barrel regions ( $0.8 < |\eta| < 1.7$ );  
819 the hadronic endcap calorimeter (HEC) covering  $1.5 < |\eta| < 3.2$ ; and the forward calorimeter  
820 (FCal) covering  $3.2 < |\eta| < 4.9$ . The tile calorimeter covers the EM calorimeter barrel region  
821 and uses steel as material for the absorbing layers with scintillating tiles for the active layers.  
822 Signals captured by scintillating tiles are read out from both sides using photomultiplier  
823 tubes. The HEC calorimeter covers the endcap regions of the EM calorimeter and uses a  
824 copper-LAr calorimeter layer scheme. The FCal is located close to the beamline providing  
825 coverage for particles traveling close to parallel with the beam axis. The subdetector contains  
826 three modules: one with copper absorbing layers optimized for EM measurements, and two  
827 with tungsten absorbing layers targeting hadronic cascades. All modules in the FCal use  
828 LAr as the active layer.

829 **3.2.3 Muon spectrometer**

830 Generally, the only particles that penetrate past the calorimeter layer are muons and  
831 neutrinos. The muon spectrometer (MS) [27] is situated on the outermost of the ATLAS  
832 detector and aims to track and measure muons within  $|\eta| < 2.7$ . The MS utilizes an array of  
833 toroid magnets to provide a magnetic field perpendicular to the muon trajectory, bending  
834 the track in order to measure its curvature. The magnetic field is powered by a large barrel

835 toroid ( $|\eta| < 1.4$ ) with strength of 0.5 T and two endcap toroid magnets ( $1.6 < |\eta| < 2.7$ ) of  
836 1 T. Both types contribute to the magnetic field in the transition region ( $1.4 < |\eta| < 1.6$ ).

837 To measure the muon itself, four types of large gas-filled chambers known as muon cham-  
838 bers [27] are designed and constructed for two main goals: triggering on potential muon  
839 candidates entering the MS and tracking their trajectories through the detector with high  
840 precision. The tracking system include Monitored Drift Tubes (MDTs), which record muon  
841 track information over the entire MS  $\eta$  range ( $|\eta| < 2.7$ ). The MDTs are built with multi-  
842 ple layers of drift tubes and filled with a mixture of 93% Ar and 7% CO<sub>2</sub>. Muons passing  
843 through drift tubes in the MDT ionize the gas within each tube; signals are then recorded  
844 as freed electrons drift to read-out channels under an applied electric field. In the forward  
845 region ( $2.0 < |\eta| < 2.7$ ), Cathode Strip Chambers (CSCs) are included along with MDTs.  
846 The CSCs are multiwire proportional chambers built with higher granularity and shorter  
847 drift time than the MDTs to handle tracking in an environment with high background rates

848 .

849 The MS trigger system includes Resistive Plate Chambers (RPCs) [27], which provide  
850 triggering in the barrel region ( $|\eta| < 1.05$ ) using parallel electrode plates made of resistive  
851 materials with a gas mixture inbetween. High voltage is applied to the plates, accelerat-  
852 ing the electrons freed from ionized gas and creating a fast avalanche of charge, which is  
853 collected on external read-out strips almost instantaneously. Triggering and coarse position  
854 measurements in the endcap region ( $1.05 < |\eta| < 2.5$ ) is handled by Thin-Gap Chambers  
855 (TGCs). Similar to CSCs, TGCs are multiwire proportional chambers with a small wire gap  
856 ("thin-gap") and high applied voltage across the gap, resulting in fast response time giving  
857 TGCs the capabilities to identify muon candidates in real time.

858    **3.2.4 Trigger & data acquisition**

859    The LHC produces a colossal amount of collision data at a bunch crossing rate of 40 MHz  
860    with bunch spacing of 25 ns. The ATLAS Trigger and Data Acquisition (TDAQ) system [95]  
861    synchronously identifies and records interesting events for in-depth analysis. The ATLAS  
862    trigger system in Run 2 consists of two steps: Level-1 (L1) trigger and High-Level Trigger  
863    (HLT). Events failing any step in the trigger chain are permanently lost.

864    The L1 trigger hardware is divided into L1 calorimeter triggers (L1Calo) and L1 muon  
865    triggers (L1Muon) [95]. L1Calo trigger uses information from ATLAS calorimeter system  
866    to quickly identify signs of high  $p_T$  objects e.g. EM clusters, jets and missing transverse  
867    energy  $E_T^{\text{miss}}$  (section 4.4). Similarly, L1Muon uses information from the RPCs and TGCs  
868    of the MS to make quick decisions on potentially interesting muon candidates. Outputs  
869    from L1Calo and L1Muon are fed into the L1 topological trigger (L1Topo) for additional  
870    filtering based on event topology and multi-object correlation, allowing for more selective  
871    and physics-motivated triggering. Decisions from all three types of L1 triggers are provided  
872    as inputs for the Central Trigger Processor (CTP) for a final Level-1 Accept (L1A) decision.

873    The entire L1 trigger chain results in a 2.5  $\mu\text{s}$  latency and reduces the event rate to 100 kHz.

874    Events passing L1 triggers are sent to HLTs before being saved to offline storage at  
875    CERN data centers. HLTs are software-based triggers used for more complex and specific  
876    selections on physics objects required by targeted analysis goals, in turn requiring more  
877    computing power with longer latency. After HLT selections, the event rate is reduced to 1  
878    kHz on average [95]. Overall, the full trigger chain reduces the event rate for ATLAS by  
879    approximately a factor of  $4 \times 10^4$ .

# 880 Chapter 4. Particle Reconstruction & Identifi- 881 fication

882 Activity within the ATLAS detector is recorded as raw electronic signals, which can  
883 be utilized by ATLAS reconstruction software to derive physics objects for analysis. This  
884 chapter describes the reconstruction and identification of basic objects (e.g. interaction  
885 vertices, tracks, topological clusters of energy deposits) and subsequently of complex physics  
886 objects i.e. particles and particle signatures.

## 887 4.1 Primary reconstruction

### 888 4.1.1 Tracks

889 Charged particles traveling through the ATLAS detector deposit energy in different layers  
890 of the ID and MS. The ID track reconstruction software consists of two algorithm chains:  
891 inside-out and outside-in track reconstruction [96–98].

892 The inside-out algorithm is primarily used for the reconstruction of primary particles  
893 i.e. particles directly produced from  $pp$  collisions or decay products of short-lived particles.  
894 The process starts by forming space points from seeded hits in the silicon detectors within  
895 the pixel & SCT detectors. Hits further away from the interaction vertex are added to  
896 the track candidate using a combinatorial Kalman filter [99] pattern recognition algorithm.  
897 Track candidates are then fitted with a  $\chi^2$  filter [100] and loosely matched to a fixed-sized  
898 EM cluster. Successfully matched track candidates are re-fitted with a Gaussian-sum filter  
899 (GSF) [101], followed by a track scoring strategy to resolve fake tracks & hit ambiguity

900 between different tracks [102]. The track candidate is then extended to the TRT to form  
901 final tracks satisfying  $p_T > 400$  MeV. The outside-in algorithm handles secondary tracks  
902 mainly produced from long-lives particles or decays of primary particles by back-tracking  
903 from TRT segments, which are then extended inward to match silicon hits in the pixel and  
904 SCT detectors to form track reconstruction objects.

### 905 4.1.2 Vertices

906 Vertices represent the point of interaction or decay for particles within the ATLAS de-  
907 tector. Primary vertices (PVs) are defined as the point of collision for hard-scattering  $pp$   
908 interactions, while secondary or displaced vertices result from particle decays occurring at a  
909 distance from its production point.

910 Reconstruction of PVs is crucial to accurately profile the kinematic information of an  
911 event and form a basis for subsequent reconstruction procedures. Primary vertex recon-  
912 struction occurs in two stages: vertex finding and vertex fitting [103]. The vertex finding  
913 algorithm uses the spatial coordinates of reconstructed tracks to form the seed for a vertex  
914 candidate. An adaptive vertex fitting algorithm [104] then iteratively evaluates track-vertex  
915 compatibility to estimate a new best vertex position. Less compatible tracks are down-  
916 weighted in each subsequent iteration, and incompatible tracks are removed and can be  
917 used for another vertex seed; the process is repeated until no further PV can be found.  
918 All reconstructed vertices without at least two matched tracks are considered invalid and  
919 discarded.

920 Secondary vertex reconstruction uses the Secondary Vertex Finder (SVF) algorithm [105]  
921 which is primarily designed to reconstruct  $b$ - and  $c$ -hadrons for flavor tagging purposes. The  
922 SVF aims to reconstruct one secondary vertex per jet and only considers tracks that are

923 matched to a two-track vertex and contained within a  $p_T$ -dependent cone around the jet  
924 axis. The tracks are then used to reconstruct a secondary vertex candidate using an iterative  
925 process similar to the PV vertex fitting procedure.

926 **Pile-up**

927 At high luminosities, multiple interactions can be associated with one bunch crossing,  
928 resulting in many PVs. The effect is called pile-up [106], and usually result from soft QCD  
929 interactions. Pile-up can be categorized into two types: in-time pile-up, stemming from  
930 additional  $pp$  collisions in the same bunch crossing that is not the hard-scatter process; out-  
931 of-time pile-up, resulting from leftover energy deposits in the calorimeters from other bunch  
932 crossings.

933 **4.1.3 Topological clusters**

934 Topological clusters (topo-clusters) [107] consist of clusters of spatially related calorimeter  
935 cell signals. Topo-clusters are primarily used to reconstruct hadron- and jet-related objects  
936 in an effort to extract signal while minimizing electronic effects and physical fluctuations, and  
937 also allow for recovery of energy lost through bremsstrahlung or photon conversions. Cells  
938 with signal-to-noise ratio  $\zeta_{\text{cell}}^{\text{EM}}$  passing a primary seed threshold are seeded into a dynamic  
939 topological cell clustering algorithm as part of a proto-cluster. Neighboring cells satisfying a  
940 cluster growth threshold are collected into the proto-cluster. If a cell is matched to two proto-  
941 clusters, the clusters are merged. Two or more local signal maxima in a cluster satisfying  
942  $E_{\text{cell}}^{\text{EM}} > 500 \text{ MeV}$  suggest the presence of multiple particles in close proximity, and the cluster  
943 is split accordingly to maintain good resolution of the energy flow. The process continues  
944 iteratively until all cells with  $\zeta_{\text{cell}}^{\text{EM}}$  above a principal cell filter level have been matched to a

945 cluster.

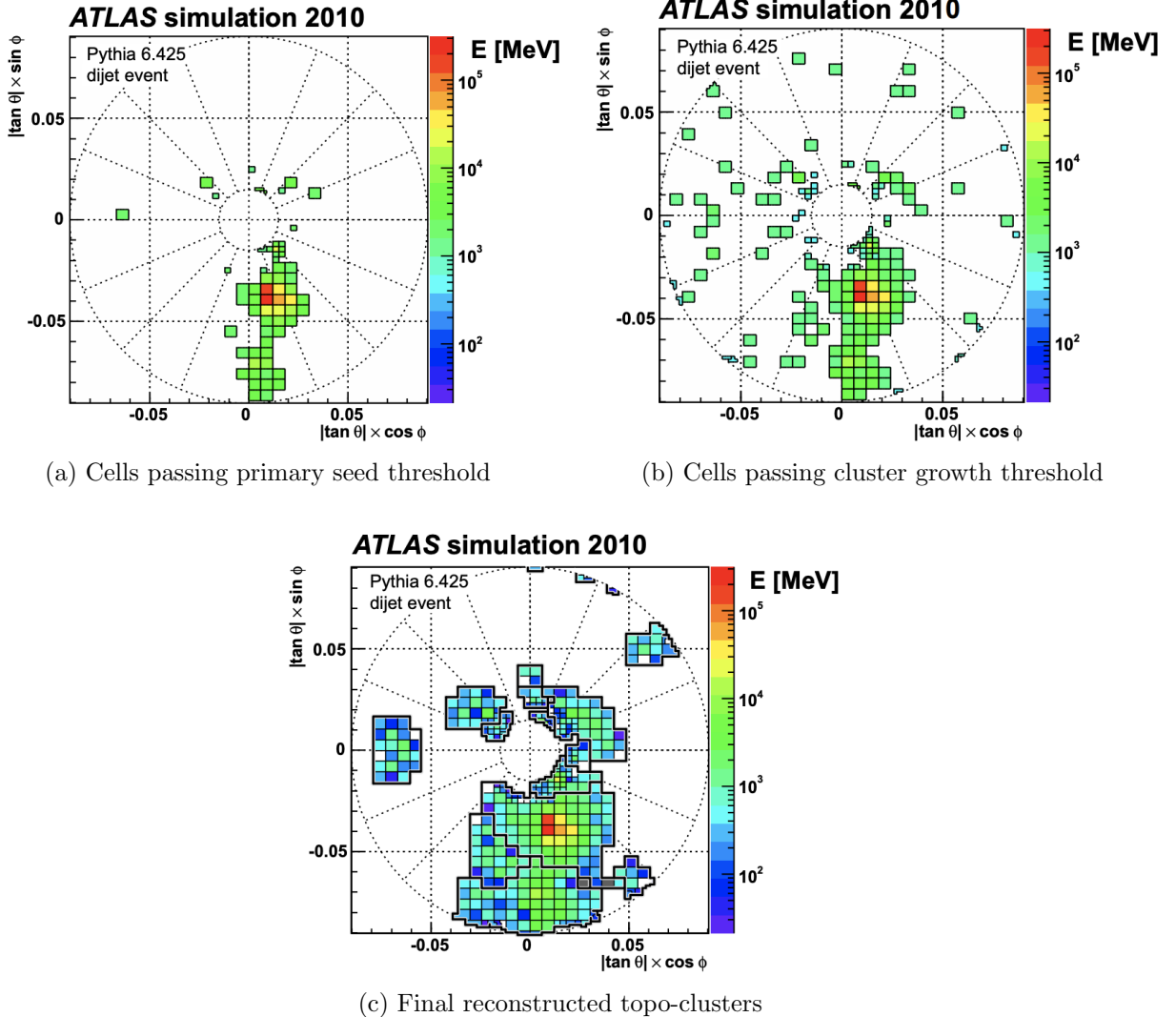


Figure 4.1: Stages of topo-cluster formation corresponding to each threshold. In (a), proto-clusters are seeded from cells with adequate signal significance  $\zeta_{\text{cell}}^{\text{EM}}$ . The clusters are further merged and split in (b) following a predefined cluster growth threshold. The process stops in (c) when all sufficiently significant signal hits have been matched to a cluster [107].

## 946 4.2 Jets

947 Quarks, gluons and other hadrons with non-neutral color charge cannot be observed  
948 individually due to QCD color confinement, which forces a non-color-neutral hadron to

949 almost immediately undergo hadronization, producing a collimated cone of color-neutral  
950 hadrons defined as a jet. Jet signals can be used to reconstruct and indirectly observe the  
951 quarks or gluons from which the jet originated in the original hard-scattering process.

### 952 4.2.1 Jet reconstruction

953 The ATLAS jet reconstruction pipeline is largely carried out using a particle flow (PFlow)  
954 algorithm combined with an anti- $k_t$  jet clustering algorithm. The PFlow algorithm [108]  
955 utilizes topo-clusters along with information from both the calorimeter systems and the ID in  
956 order to make use of the tracker system’s advantages in low-energy momentum resolution and  
957 angular resolution. First, the energy from charged particles is removed from the calorimeter  
958 topo-clusters; then, it is replaced by particle objects created using the remaining energy in  
959 the calorimeter and tracks matched to topo-clusters. The ensemble of ”particle flow objects”  
960 and corresponding matched tracks are used as inputs for the iterative anti- $k_t$  algorithm [109].

961 The main components of the anti- $k_t$  algorithm involve the distance  $d_{ij}$  between two  
962 jet candidates  $i$  and  $j$ , and the distance  $d_{iB}$  between the harder jet candidate of the two  
963 (defined as  $i$ ) and the beamline  $B$ . If  $d_{ij} < d_{iB}$ , then the two jet candidates are combined  
964 and returned to the pool of candidates; otherwise, jet candidate  $i$  is considered a jet and  
965 removed from the pool. The distance  $d_{ij}$  is inversely proportional to a predefined radius  
966 parameter  $\Delta R$  in order to control reconstruction quality for small- $R$  and large- $R$  jets. This  
967 analysis uses  $\Delta R = 0.4$  to better handle heavily collimated small- $R$  jets resulting from parton  
968 showers.

969 The anti- $k_t$  jets so far have only been reconstructed at the EM level and need to be  
970 calibrated to match the energy scale of jets reconstructed at particle level. This is done  
971 via a MC-based jet energy scale (JES) calibration sequence, along with further calibrations

972 to account for pile-up effects and energy leakage. The full JES calibration sequence is  
 973 shown in Figure 4.2. All calibrations except origin correction are applied to the jet's four-  
 974 momentum i.e. jet  $p_T$ , energy and mass. Afterwards, a jet energy resolution (JER) [110]  
 975 calibration step is carried out in a similar manner to JES to match the resolution of jets in  
 976 dijet events. To further suppress pile-up effects, a neural-network based jet vertex tagger  
 977 (NNJvt) discriminant was developed based on the previous jet vertex tagger (JVT) algorithm  
 978 [106] and applied to low- $p_T$  reconstructed jets.

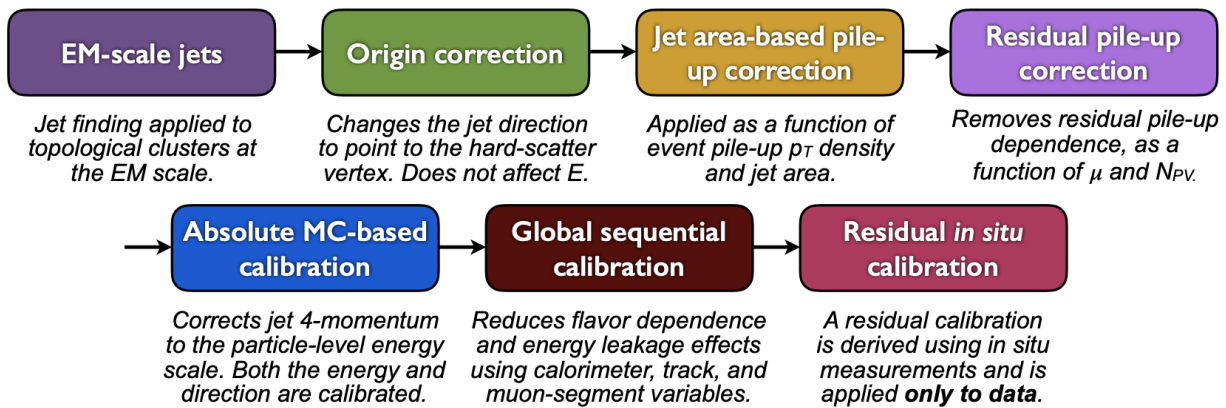


Figure 4.2: Jet energy scale calibration sequence for EM-scale jets [111].

### 979 4.2.2 Flavor tagging

980 Identifying and classifying hadronic jets are important tasks for ATLAS physics, for  
 981 example analyses involving Higgs decays  $H \rightarrow b\bar{b}$  or top quarks. Flavor tagging or  $b$ -tagging  
 982 is the process of identifying jets containing  $b$ -hadrons,  $c$ -hadrons, light-hadrons ( $uds$ -hadrons)  
 983 or jets from hadronically decaying  $\tau$  leptons. Distinguishing  $b$ -jets is possible due to their  
 984 characteristically long lifetime ( $\tau \approx 1.5$  ps), displaced secondary decay vertex and high decay  
 985 multiplicity.

986 Usage of  $b$ -tagging in this analysis is done via five operating points (OPs), corresponding

987 to 65%, 70%, 77%, 85% and 90%  $b$ -jet tagging efficiency  $\varepsilon_b$  in simulated  $t\bar{t}$  events, in order  
988 from the tightest to loosest discriminant cut point. The OPs are defined by placing selections  
989 on the tagger output to provide a predefined  $\varepsilon_b$  level; the selection cuts act as a variable  
990 trade-off between  $b$ -tagging efficiency and  $b$ -jet purity i.e.  $c$ - or light-jet rejection. For this  
991 analysis, a jet is considered  $b$ -tagged if it passes the 85% OP. The  $b$ -tagged jet is then  
992 assigned a pseudo-continuous  $b$ -tagging (PCBT) score, which quantifies a jet's ability to  
993 satisfy different OPs. The score can take integer values between 1 and 6, where a score of 6  
994 is assigned to jets passing all OP thresholds; a score of 2 for jets that pass only the tightest  
995 OP (90%); and a score of 1 for jets that pass no OP. A value of -1 is also defined for any jet  
996 that does not satisfy  $b$ -tagging criteria. Since the targeted  $t\bar{t}t\bar{t}$  final states contain at least  
997 four  $b$ -hadrons from top and  $W$  decays, a  $b$ -tagging OP of 85% is used to maintain high  
998 purity during  $b$ -tagged jet selections in the signal region.

999 **GN2  $b$ -tagging algorithm**

1000 For this analysis,  $b$ -jets are identified and tagged with the GN2v01  $b$ -tagger [112]. The  
1001 GN2 algorithm uses a Transformer-based model [113] modified to incorporate domain knowl-  
1002 edge and additional auxiliary physics objectives: grouping tracks with a common vertex and  
1003 predicting the underlying physics process for a track. The network structure is shown in  
1004 Figure 4.3. The GN2  $b$ -tagger form the input vector by concatenating 2 jet variables and  
1005 19 track reconstruction variables (for up to 40 tracks), normalized to zero mean and unit  
1006 variance. The output consists of a track-pairing output layer of size 2, a track origin clas-  
1007 sification layer of 7 categories, and a jet classification layer of size 4 for the probability of  
1008 each jet being a  $b$ -,  $c$ -, light- or  $\tau$ -jet respectively. For  $b$ -tagging purpose, a discriminant is

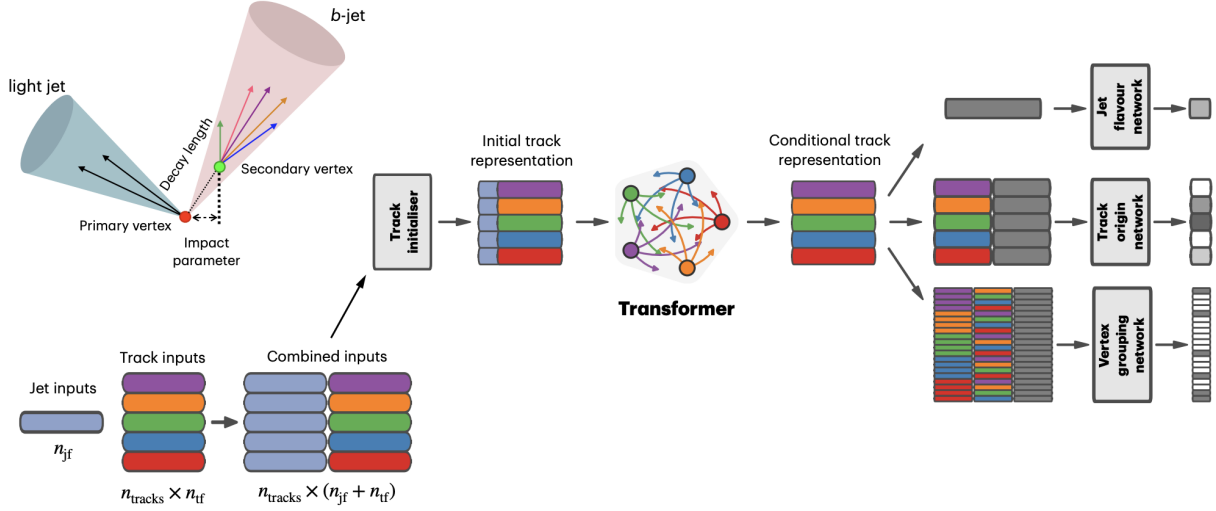


Figure 4.3: Overview of the GN2 architecture. The number of jet and track features are represented by  $n_{jf}$  and  $n_{tf}$  respectively. The global jet representation and track embeddings output by the Transformer encoder are used as inputs for three task-specific networks [112].

1009 defined using these four outputs

$$D_b = \ln \left( \frac{p_b}{f_c p_c + f_\tau p_\tau + (1 - f_c - f_\tau)p_{\text{light}}} \right) \quad (4.1)$$

1010 where  $p_x$  is the probability of the jet being an  $x$ -jet as predicted by GN2, and  $f_c$ ,  $f_\tau$  are tun-  
 1011 able free parameters controlling balance between  $c$ - and light-jet rejection. Simulated SM  $t\bar{t}$   
 1012 and BSM  $Z'$  events from  $pp$  collisions were used as training and evaluation samples. In order  
 1013 to minimize bias, both  $b$ - and light-jet samples are re-sampled to match  $c$ -jet distributions.  
 1014 Figure 4.4 shows the performance of GN2 compared to the previous convolutional neural  
 1015 network-based standard  $b$ -tagging algorithm DL1d, in terms of  $c$ -, light- and  $\tau$ -jet rejection  
 1016 as a function of  $b$ -tagging efficiency. The network gives a factor of 1.5-4 improvement in  
 1017 experimental applications compared to DL1d [112], without dependence on the choice of  
 1018 MC event generator or inputs from low-level flavor tagging algorithm.

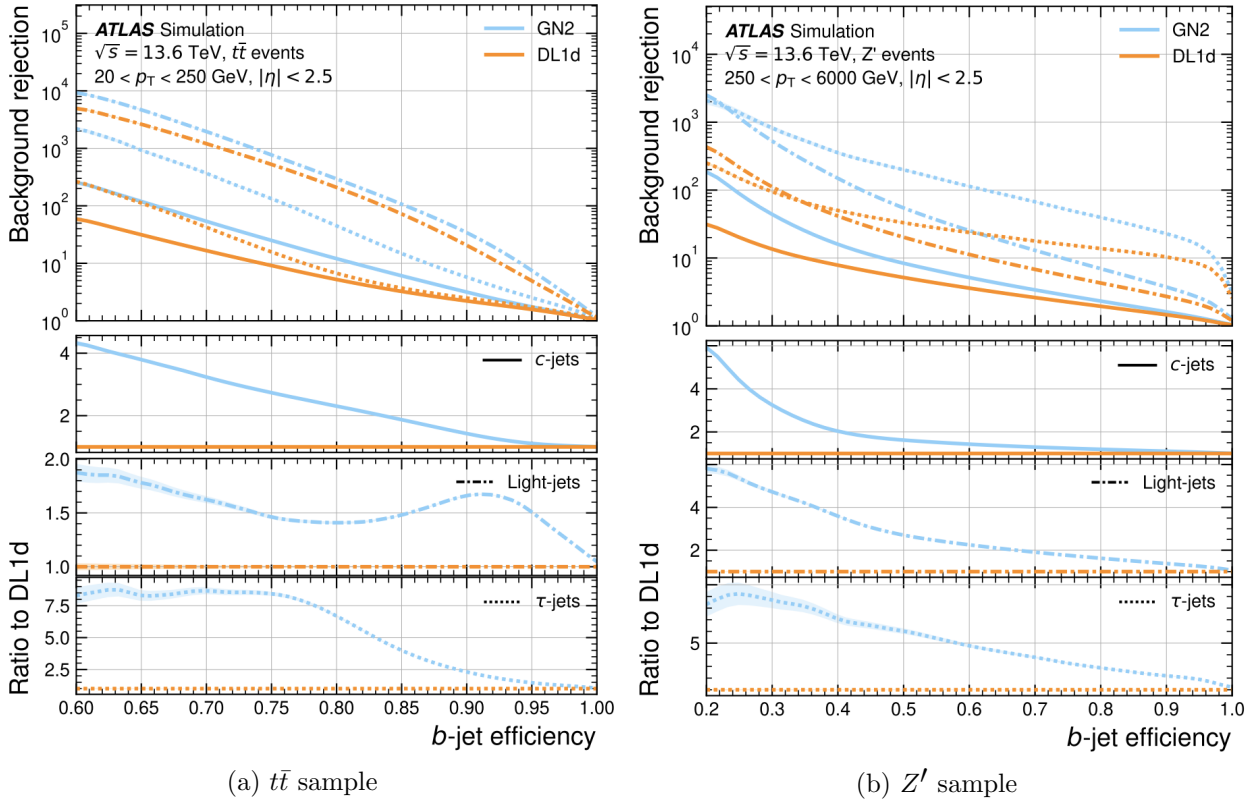


Figure 4.4: The  $c$ -, light- and  $\tau$ -jet rejection rate as a function of  $b$ -tagging efficiency for GN2 and DL1d using (a) jets in the  $t\bar{t}$  sample, and (b) jets in the  $Z'$  sample. The performance ratios of GN2 to DL1d are shown in the bottom panels [112].

## 1019 Efficiency calibration

1020 Due to imperfect description of detector response and physics modeling effects in simu-  
 1021 lation, the  $b$ -tagging efficiency predicted by MC simulation  $\varepsilon_b^{\text{sim}}$  requires a correction factor  
 1022 to match the efficiency measured in collision data  $\varepsilon_b^{\text{data}}$ . The correction scale factors (SFs)  
 1023 are defined as  $\text{SF} = \varepsilon_b^{\text{data}} / \varepsilon_b^{\text{sim}}$  and are determined by data-to-MC calibration using samples  
 1024 enriched in dileptonic  $t\bar{t}$  decays [114]. The resulting SFs are applied to MC simulated jets  
 1025 individually.

## 1026 4.3 Leptons

1027 Lepton reconstruction in ATLAS involves electron and muon reconstruction since tau  
1028 decays quickly, and depending on decay mode can be reconstructed using either jets or light  
1029 leptons. From here on out within this dissertation, leptons will be used exclusively to refer to  
1030 electrons and muons. Leptons can be classified into two categories: prompt leptons resulting  
1031 from heavy particle decays and non-prompt leptons resulting from detector or reconstruction  
1032 effects, or from heavy-flavor hadron decays.

### 1033 4.3.1 Electrons

1034 Electrons leave energy signature in the detector by interacting with the detector materials  
1035 and losing energy in the form of bremsstrahlung photons. A bremsstrahlung photon can  
1036 produce an electron-positron pair which can itself deposit signals in the detector, creating a  
1037 cascade of particles that can leave multiple of either tracks in the ID or EM showers in the  
1038 calorimeters, all of which are considered part of the same EM topo-cluster. Electron signal  
1039 signature has three characteristic components: localized energy deposits in the calorimeters,  
1040 multiple tracks in the ID and compatibility between the above tracks and energy clusters in  
1041 the  $\eta \times \phi$  plane [115]. Electron reconstruction in ATLAS follows these steps accordingly.

1042 Seed-cluster reconstruction and track reconstruction are performed sequentially in ac-  
1043 cordance with the iterative topo-clustering algorithm and track reconstruction method de-  
1044 scribed in section 4.1. The seed-cluster and GSF-refitted track candidate not associated  
1045 with a conversion vertex are matched to form an electron candidate. The cluster energy is  
1046 then calibrated using multivariate techniques on data and simulation to match the original  
1047 electron energy.

1048 **Electron identification**

1049 Additional LH-based identification selections using ID and EM calorimeter information  
1050 are implemented to further improve the purity of reconstructed electrons in the  $|\eta| < 2.47$  re-  
1051 gion of the detector [115]. The electron LH function is built with the signal being prompt elec-  
1052 trons and background being objects with similar signature to prompt electrons i.e. hadronic  
1053 jet deposits, photon conversions or heavy-flavor hadron decays. Three identification OPs  
1054 are defined for physics analyses: *Loose*, *Medium* and *Tight*, optimized for 9 bins in  $|\eta|$  and  
1055 12 bins in  $E_T$  with each OP corresponding to a fixed efficiency requirement for each bin.  
1056 For typical EW processes, the target efficiencies for *Loose*, *Medium* and *Tight* start at 93%,  
1057 88% and 80% respectively and increase with  $E_T$ . Similar to  $b$ -tagging OPs, the electron  
1058 identification OPs represent a trade-off in signal efficiency and background rejection. The  
1059 electron efficiency are estimated using tag-and-probe method on samples of  $J/\Psi \rightarrow ee$  and  
1060  $Z \rightarrow ee$  [115]. The *Tight* electron identification OP is used for this analysis.

1061 **Electron isolation**

1062 A characteristic distinction between prompt electrons and electrons from background  
1063 processes is the relative lack of activity in both the ID and calorimeters within an  $\Delta\eta \times \Delta\phi$   
1064 area surrounding the reconstruction candidate. Calorimeter-based and track-based electron  
1065 isolation variables [115] are defined to quantify the amount of activity around the electron  
1066 candidate using topo-clusters and reconstructed tracks respectively.

1067 Calorimeter-based isolation variables  $E_T^{\text{cone}XX}$  are computed by first summing the energy  
1068 of topo-clusters with barycenters falling within a cone of radius  $\Delta R = \sqrt{(\Delta\eta)^2 + (\Delta\phi)^2} =$   
1069  $XX/100$  around the direction of the electron candidate. The final isolation variables are

obtained by subtracting from the sum the energy belonging to the candidate electron at the core of the cone, then applying corrections for pile-up effects and energy leakage outside of the core. Similar to calorimeter-based variables, track-based isolation variables  $p_T^{\text{varcone}XX}$  are calculated by summing all track  $p_T$  within a cone of radius  $\Delta R$  around the electron candidate, minus the candidate's contribution. The cone radius is variable as a function of  $p_T$  and is described as

$$\Delta R \equiv \min \left( \frac{10}{p_T}, \Delta R_{\max} \right), \quad (4.2)$$

where  $p_T$  is expressed in GeV and  $\Delta R_{\max}$  is the maximum cone size, defined to account for closer proximity of decay products to the electron in high-momentum heavy particle decays. Four isolation operating points are implemented to satisfy specific needs by physics analyses: *Loose*, *Tight*, *HighPtCaloOnly* and *Gradient* [115]. For this analysis, electrons isolation uses *Tight* requirements.

## 1081 Electron charge misidentification

Charge misidentification is a crucial irreducible background, particularly for analyses with electron charge selection criteria. Electron charge is determined by the curvature of the associated reconstructed track, and misidentification of charge can occur via either an incorrect curvature measurement or an incorrectly matched track. Inaccurate measurement is more likely for high energy electrons due to the small curvature in track trajectories at high  $p_T$ , while track matching error usually results from bremsstrahlung pair-production generating secondary tracks in close proximity [115]. Suppression of charge misidentification background in Run 2 is additionally assisted by a boosted decision tree discriminant known

1090 as the Electron Charge ID Selector (ECIDS). For this analysis, all electrons are required to  
1091 pass the ECIDS criterion.

1092 **4.3.2 Muons**

1093 Muons act as minimum-ionizing particles, leaving tracks in the MS or characteristics  
1094 energy deposits in the calorimeter and can be reconstructed globally using information from  
1095 the ID, MS and calorimeters. Five reconstruction strategies corresponding to five muon  
1096 types [116] are utilized in ATLAS:

- Combined (CB): the primary ATLAS muon reconstruction method. Combined muons  
1097 are first reconstructed using MS tracks then extrapolated to include ID tracks (outside-in strategy). A global combined track fit is performed on both MS and ID tracks.
- Inside-out combined (IO): complementary to CB reconstruction. IO muon tracks are  
1100 extrapolated from ID to MS, then fitted with MS hits and calorimeter energy loss in a  
1101 combined track fit.
- MS extrapolated (ME): ME muons are defined as muons with a MS track that cannot  
1103 be matched to an ID track using CB reconstruction. ME muons allow extension of  
1104 muon reconstruction acceptance to regions not covered by the ID ( $2.5 < |\eta| < 2.7$ )
- Segment-tagged (ST): ST muons are defined as a successfully matched ID track that  
1106 satisfies tight angular matching criteria to at least one reconstructed MDT or CSC  
1107 segment when extrapolated to the MS. MS reconstruction is used primarily when  
1108 muons only crossed one layer of MS chambers.
- Calorimeter-tagged (CT): CT muons are defined as an ID track that can be matched to  
1110

1111 energy deposits consistent with those of a minimum-ionizing particle when extrapolated  
1112 through the calorimeter. CT reconstruction extends acceptance range to regions in the  
1113 MS with sparse instrumentation ( $|\eta| < 0.1$ ) with a higher  $p_T$  threshold of 5 GeV,  
1114 compared to the 2 GeV threshold used by other muon reconstruction algorithms due  
1115 to large background contamination at the low  $p_T$  range of  $15 < p_T < 100$  GeV [117].

## 1116 Muon identification

1117 Reconstructed muons are further filtered by identification criteria to select for high-  
1118 quality prompt muons. Requirements include number of hits in the MS and ID, track fit  
1119 properties and compatibility between measurements of the two systems. Three standard  
1120 OPs (*Loose*, *Medium*, *Tight*) are defined to better match the needs of different physics  
1121 analyses concerning prompt muon  $p_T$  resolution, identification efficiency and non-prompt  
1122 muon rejection. The default identification OP for ATLAS physics and also the OP used in  
1123 this analysis is *Medium*, which provides efficiency and purity suitable for a wide range of  
1124 studies while minimizing systematic uncertainties [116].

## 1125 Muon isolation

1126 Muons from heavy particle decays are often produced in an isolated manner compared to  
1127 muons from semileptonic decays, and is therefore an important tool for background rejection  
1128 in many physics analyses. Muon isolation strategies are similar to that of electron in section  
1129 4.3.1, with track-based and calorimeter-based isolation variables. Seven isolation OPs are  
1130 defined using either or both types of isolation variables, balancing between prompt muon  
1131 acceptance and non-prompt muon rejection. The full definition and description for the muon  
1132 isolation OPs are detailed in Ref. [116].

## 1133 4.4 Missing transverse momentum

1134 Collisions at the LHC happen along the  $z$ -axis of the ATLAS coordination system between  
1135 two particle beam of equal center-of-mass energy. By conservation of momentum, the sum of  
1136 transverse momenta of outgoing particles should be zero. A discrepancy between measured  
1137 momentum and zero would then suggest the presence of undetectable particles, which would  
1138 consist of either SM neutrinos or some unknown BSM particles, making missing transverse  
1139 momentum ( $E_T^{\text{miss}}$ ) an important observable to reconstruct.

1140 Reconstructing  $E_T^{\text{miss}}$  utilizes information from fully reconstructed leptons, photons, jets  
1141 and other matched track-vertex objects not associated with a prompt object (soft signals),  
1142 defined with respect to the  $x(y)$ -axis as

$$E_{x(y)}^{\text{miss}} = - \sum_{i \in \{\text{hard objects}\}} p_{x(y),i} - \sum_{j \in \{\text{soft signals}\}} p_{x(y),j}, \quad (4.3)$$

1143 where  $p_{x(y)}$  is the  $x(y)$ -component of  $p_T$  for each particle [118]. The following observables  
1144 can then be defined:

$$\begin{aligned} \mathbf{E}_T^{\text{miss}} &= (E_x^{\text{miss}}, E_y^{\text{miss}}), \\ E_T^{\text{miss}} &= |\mathbf{E}_T^{\text{miss}}| = \sqrt{(E_x^{\text{miss}})^2 + (E_y^{\text{miss}})^2}, \\ \phi^{\text{miss}} &= \tan^{-1}(E_y^{\text{miss}}/E_x^{\text{miss}}), \end{aligned} \quad (4.4)$$

<sub>1145</sub> where  $E_T^{\text{miss}}$  represents the magnitude of the missing transverse energy vector  $\mathbf{E}_T^{\text{miss}}$ , and  
<sub>1146</sub>  $\phi^{\text{miss}}$  its direction in the transverse plane. The vectorial sum  $\mathbf{E}_T^{\text{miss}}$  can be broken down into

$$\mathbf{E}_T^{\text{miss}} = - \underbrace{\sum_{\text{selected electrons}} \mathbf{p}_T^e - \sum_{\text{selected muons}} \mathbf{p}_T^\mu - \sum_{\text{accepted photons}} \mathbf{p}_T^\gamma - \sum_{\text{accepted } \tau\text{-leptons}} \mathbf{p}_T^\tau}_{\text{hard term}} - \underbrace{\sum_{\text{accepted jets}} \mathbf{p}_T^{\text{jet}} - \sum_{\text{unused tracks}} \mathbf{p}_T^{\text{track}}}_{\text{soft term}}. \quad (4.5)$$

<sub>1147</sub> Two OPs are defined for  $E_T^{\text{miss}}$ , *Loose* and *Tight*, with selections on jet  $p_T$  and JVT criteria  
<sub>1148</sub> [119]. The *Tight* OP is used in this analysis; *Tight* reduces pile-up dependence of  $E_T^{\text{miss}}$   
<sub>1149</sub> by removing the phase space region containing more pile-up than hard-scatter jets, at the  
<sub>1150</sub> expense of resolution and scale at low pile-up,

## <sub>1151</sub> 4.5 Overlap removal

<sub>1152</sub> Since different objects are reconstructed independently, it is possible for the same de-  
<sub>1153</sub> tector signals to be used to reconstruct multiple objects. An overlap removal strategy is  
<sub>1154</sub> implemented to resolve ambiguities; the overlap removal process for this analysis applies  
<sub>1155</sub> selections in Table 4.1 sequentially, from top to bottom.

Table 4.1: Overlap removal process for this analysis, applied sequentially from top to bottom.

Remove	Keep	Matching criteria
Electron	Electron	Shared ID track, $p_{T,1}^e < p_{T,2}^e$
Muon	Electron	Shared ID track, CT muon
Electron	Muon	Shared ID track
Jet	Electron	$\Delta R < 0.2$
Electron	Jet	$\Delta R < 0.4$
Jet	Muon	( $\Delta R < 0.2$ or ghost-associated) & $N_{\text{track}} < 3$
Muon	Jet	$\Delta R < \min(0.4, 0.04 + 10\text{GeV}/p_T^\mu)$

## 1156 4.6 Object definition

1157 Table 4.2 summarizes the selections on physics objects used in this analysis. Each se-  
1158 lection comes with associated calibration scale factors (SFs) to account for discrepancies  
1159 between data and MC simulation, and are applied multiplicatively to MC event weights.

Table 4.2: Summary of object selection criteria used in this analysis.  $\ell_0$  refers to the leading lepton in the event.

Selection	Electrons	Muons	Jets
$p_T$ [GeV]	$> 15$ $p_T(\ell_0) > 28$	$> 15$	$> 20$
$ \eta $	$1.52 \leq  \eta  < 2.47$ $< 1.37$	$< 2.5$	$< 2.5$
Identification	<i>TightLH</i> pass ECIDS ( $ee/e\mu$ )	<i>Medium</i>	NNJvt <i>FixedEffPt</i> ( $p_T < 60$ , $ \eta  < 2.4$ )
Isolation	<i>Tight_VarRad</i>	<i>PflowTight_VarRad</i>	
Track-vertex assoc.			
$ d_0^{\text{BL}}(\sigma) $	$< 5$	$< 3$	
$ \Delta z_0^{\text{BL}} \sin \theta $ [mm]	$< 0.5$	$< 0.5$	

# 1160 Chapter 5. Data & Simulated Samples

## 1161 5.1 Data samples

1162 Data samples used in this analysis were collected by the ATLAS detector during Run  
1163 2 data-taking campaign between 2015-2018. The samples contain  $pp$  collisions at center-of-  
1164 mass energy of  $\sqrt{s} = 13$  TeV with 25 ns bunch-spacing, which corresponds to an integrated  
1165 luminosity of  $140 \text{ fb}^{-1}$  with an uncertainty of 0.83% [88]. The HLT trigger strategy is similar  
1166 to that of previous  $t\bar{t}t\bar{t}$  observation analysis [44] and include single lepton and dilepton  
1167 triggers. Calibration for di-muon and electron-muon triggers were not ready for the samples  
1168 used in this analysis, and are therefore not included. Events are also required to contain at  
1169 least one lepton matched to the corresponding object firing the trigger. Triggers used are  
1170 summarized in Table 5.1.

## 1171 5.2 Monte Carlo samples

1172 Monte Carlo simulated samples are used to estimate signal acceptance before unblinding,  
1173 profile the physics background for the analysis and to study object optimizations. Simulated  
1174 samples for this analysis use are generated from ATLAS generalized MC20a/d/e samples for  
1175 Run 2, using full detector simulation (FS) and fast simulation (AF3) to simulate detector  
1176 response. MC samples used and simulation processes are summarized in Table 5.2.

Table 5.1: Summary of all HLT triggers used in this analysis. Events are required to pass at least one trigger.

Trigger	Data period			
	2015	2016	2017	2018
Single electron triggers				
HLT_e24_lhmedium_L1EM20VH	✓	-	-	-
HLT_e60_lhmedium	✓	-	-	-
HLT_e120_lhloose	✓	-	-	-
HLT_e26_lhtight_nod0_ivarloose	-	✓	✓	✓
HLT_e60_lhmedium_nod0	-	✓	✓	✓
HLT_e140_lhloose_nod0	-	✓	✓	✓
Di-electron triggers				
HLT_2e12_lhloose_L12EM10VH	✓	-	-	-
HLT_2e17_lhvloose_nod0	-	✓	-	-
HLT_2e24_lhvloose_nod0	-	-	✓	✓
HLT_2e17_lhvloose_nod0_L12EM15VHI	-	-	-	✓
Single muon trigger				
HLT_mu20_iloose_L1MU15	✓	-	-	-
HLT_mu40	✓	-	-	-
HLT_mu26_ivarmedium	-	✓	✓	✓
HLT_mu50	-	✓	✓	✓

### <sup>1177</sup> 5.2.1 $t\bar{t}Z'$ signal samples

<sup>1178</sup> Signal  $t\bar{t}Z'$  samples were generated based on the simplified topophilic resonance model in  
<sup>1179</sup> section 2.2.1. Six  $Z'$  mass points were utilized for the generation of the signal sample: 1000,  
<sup>1180</sup> 1250, 1500, 2000, 2500 and 3000 GeV. The top- $Z'$  coupling  $c_t$  is chosen to be 1 for a narrow  
<sup>1181</sup> resonance peak, and the chirality angle  $\theta$  is chosen to be  $\pi/4$  to suppress loop production  
<sup>1182</sup> of  $Z'$ . The samples were then generated with MADGRAPH5\_AMC@NLO v.3.5.0 [120] at  
<sup>1183</sup> LO with the NNPDF3.1LO [121] PDF set interfaced with PYTHIA8 [122] using A14 tune  
<sup>1184</sup> and NNPDF2.3lo PDF set for parton showering and hadronization. The resonance width is  
<sup>1185</sup> calculated to be 4% for  $c_t = 1$ .

Table 5.2: Summary of all Monte-Carlo samples used in this analysis.  $V$  refers to an EW ( $W^\pm/Z/\gamma^*$ ) or Higgs boson. Matrix element (ME) order refers to the order in QCD of the perturbative calculation. Tune refers to the underlying-event tune of the parton shower (PS) generator.

Process	ME Generator	ME Order	ME PDF	PS	Tune	Sim.
<b>Signals</b>						
$t\bar{t}Z'$	MADGRAPH5_AMC@NLO LO		NNPDF3.1LO		PYTHIA8 A14	FS
<b><math>t\bar{t}t\bar{t}</math> and <math>t\bar{t}\bar{t}</math></b>						
$t\bar{t}t\bar{t}$	MADGRAPH5_AMC@NLO NLO		NNPDF3.0nlo		PYTHIA8 A14	AF3
	MADGRAPH5_AMC@NLO NLO		MMHT2014 LO		HERWIG7 H7-UE-MMHT	AF3
	SHERPA	NLO	NNPDF3.0nnlo		HERWIG7 SHERPA	FS
$t\bar{t}\bar{t}$	MADGRAPH5_AMC@NLO LO		NNPDF2.3lo		PYTHIA8 A14	AF3
<b><math>t\bar{t}V</math></b>						
$t\bar{t}H$	POWHEGBOX v2	NLO	NNPDF3.0nlo		PYTHIA8 A14	FS
	POWHEGBOX v2	NLO	NNPDF3.0nlo		HERWIG7 H7.2-Default	FS
$t\bar{t}(Z/\gamma^*)$	MADGRAPH5_AMC@NLO NLO		NNPDF3.0nlo		PYTHIA8 A14	FS
	SHERPA	NLO	NNPDF3.0nnlo		SHERPA SHERPA	FS
$t\bar{t}W$	SHERPA	NLO	NNPDF3.0nnlo		SHERPA SHERPA	FS
	SHERPA	LO	NNPDF3.0nnlo		SHERPA SHERPA	FS
<b><math>t\bar{t}</math> and Single-Top</b>						
$t\bar{t}$	POWHEGBOX v2	NLO	NNPDF3.0nlo		PYTHIA8 A14	FS
$tW$	POWHEGBOX v2	NLO	NNPDF3.0nlo		PYTHIA8 A14	FS
$t(q)b$	POWHEGBOX v2	NLO	NNPDF3.0nlo (s)		PYTHIA8 A14	FS
			NNPDF3.0nlo 4f (t)			FS
$tWZ$	MADGRAPH5_AMC@NLO NLO		NNPDF3.0nlo		PYTHIA8 A14	FS
$tZ$	MADGRAPH5_AMC@NLO LO		NNPDF3.0nlo 4f		PYTHIA8 A14	FS
<b><math>t\bar{t}VV</math></b>						
$t\bar{t}WW$	MADGRAPH5_AMC@NLO LO		NNPDF3.0nlo		PYTHIA8 A14	FS
$t\bar{t}WZ$	MADGRAPH	LO	NNPDF3.0nlo		PYTHIA8 A14	AF3
$t\bar{t}HH$	MADGRAPH	LO	NNPDF3.0nlo		PYTHIA8 A14	AF3
$t\bar{t}WH$	MADGRAPH	LO	NNPDF3.0nlo		PYTHIA8 A14	AF3
$t\bar{t}ZZ$	MADGRAPH	LO	NNPDF3.0nlo		PYTHIA8 A14	AF3
<b><math>V(VV)+\text{jets}</math> and <math>VH</math></b>						
$V+\text{jets}$	SHERPA	NLO	NNPDF3.0nnlo		SHERPA SHERPA	FS
$VV+\text{jets}$	SHERPA	NLO	NNPDF3.0nnlo		SHERPA SHERPA	FS
		LO ( $gg \rightarrow VV$ )				FS
$VVV+\text{jets}$	SHERPA	NLO	NNPDF3.0nnlo		SHERPA SHERPA	FS
$VH$	POWHEGBOX v2	NLO	NNPDF3.0aznlo		PYTHIA8 A14	FS

<sub>1186</sub> **5.2.2 Background samples**

<sub>1187</sub> **SM  $t\bar{t}t\bar{t}$  background**

<sub>1188</sub> The nominal SM  $t\bar{t}t\bar{t}$  sample was generated with MADGRAPH5\_AMC@NLO [120] at  
<sub>1189</sub> NLO in QCD with the NNPDF3.0nlo [121] PDF set and interfaced with PYTHIA8.230 [122]  
<sub>1190</sub> using A14 tune [123]. Decays for top quarks are simulated at LO with MADSPIN [124,  
<sub>1191</sub> 125] to preserve spin information, while decays for  $b$ - and  $c$ -hadrons are simulated with  
<sub>1192</sub> EVTGEN v1.6.0 [126]. The renormalization and factorization scales  $\mu_R$  and  $\mu_F$  are set  
<sub>1193</sub> to  $1/4\sqrt{m^2 + p_T^2}$ , which represents the sum of transverse mass of all particles generated  
<sub>1194</sub> from the ME calculation [127]. The ATLAS detector response was simulated with AF3.  
<sub>1195</sub> Additional auxiliary  $t\bar{t}t\bar{t}$  samples are also generated to evaluate the impact of generator and  
<sub>1196</sub> PS uncertainties as shown in 5.2.

<sub>1197</sub>  **$t\bar{t}W$  background**

<sub>1198</sub> Nominal  $t\bar{t}W$  sample was generated using SHERPA v2.2.10 [128] at NLO in QCD with  
<sub>1199</sub> the NNPDF3.0nnlo [121] PDF with up to one extra parton at NLO and two at LO, which  
<sub>1200</sub> are matched and merged with the SHERPA PS based on Catani-Seymour dipole factorization  
<sub>1201</sub> [129] using the MEPS@NLO prescription [130–133] and a merging scale of 30 GeV. Higher-  
<sub>1202</sub> order ME corrections are provided in QCD by the OpenLoops 2 library [134–136] and in  
<sub>1203</sub> EW from  $\mathcal{O}(\alpha^3) + \mathcal{O}(\alpha_S^2\alpha^2)$  (LO3 & NLO2) via two sets of internal event weights. An  
<sub>1204</sub> alternative sample with only EW corrections at LO from  $\mathcal{O}(\alpha_S\alpha^3)$  (NLO3) diagrams were  
<sub>1205</sub> also simulated with the same settings.

1206  **$t\bar{t}(Z/\gamma^*)$  background**

1207 Nominal  $t\bar{t}(Z/\gamma^*)$  samples were generated separately for different ranges of dilepton in-  
1208 variant mass  $m_{\ell\ell}$  to account for on-shell and off-shell  $Z/\gamma^*$  production. Sample for  $m_{\ell\ell}$   
1209 between 1 and 5 GeV was produced using MADGRAPH5\_AMC@NLO [120] at NLO with  
1210 the NNPDF3.0nlo [121] PDF set, interfaced with PYTHIA8.230 [122] using A14 tune [123] and  
1211 NNPDF2.3l0 PDF set. Sample for  $m_{\ell\ell} < 5$  GeV was produced with SHERPA v2.2.10 [128]  
1212 at NLO using NNPDF3.0nnlo PDF set. To account for generator uncertainty, an alternative  
1213  $m_{\ell\ell} > 5$  GeV sample was generated with identical settings to the low  $m_{\ell\ell}$  sample. The  
1214 ATLAS detector response was simulated with full detector simulation (FS).

1215  **$t\bar{t}H$  background**

1216 Generation of  $t\bar{t}H$  background was done using POWHEGBox [137–140] at NLO in QCD  
1217 with the NNPDF3.0nlo PDF [121] set. The nominal sample is interfaced with PYTHIA8.230  
1218 [122] using the A14 tune [123] and the NNPDF2.3l0 [141] PDF set. Detector response is  
1219 simulated using FS. An alternative  $t\bar{t}H$  sample generated similarly, but instead interfaced  
1220 with HERWIG7.2.3 [142, 143] to study the impact of parton shower and hadronization model.  
1221 Detector response for the alternative sample is simulated using AF3.

1222  **$t\bar{t}t$  background**

1223 The  $t\bar{t}t$  sample is generated using MADGRAPH5\_AMC@NLO [120] at LO in QCD, inter-  
1224 faced with PYTHIA8 [122] using the A14 tune [123]. The sample is produced in the five-flavor  
1225 scheme [144] to prevent LO interference with  $t\bar{t}t\bar{t}$ .

1226  **$t\bar{t}$  background**

1227 The  $t\bar{t}$  sample is modeled with POWHEGBox [137–140] at NLO in QCD with the NNPDF3.0nlo  
1228 [121] PDF set and the  $h_{\text{damp}}$  parameter set to  $1.5m_{\text{top}}$  [145]. Events are interfaced with  
1229 PYTHIA8.230 [122] using the A14 tune [123] and the NNPDF2.3lō [141] PDF set.

1230 **Single-top ( $tW$  &  $t(q)b$ ) background**

1231 Single-top  $tW$ -associated production is modeled using the POWHEGBox generator [137–  
1232 140] at NLO in QCD in the five-flavor scheme [144] with the NNPDF3.0nlo [121] PDF set. In-  
1233 terference with  $t\bar{t}$  production [145] is handled using the diagram removal scheme [146]. Single-  
1234 top  $t(q)b$  production is modeled using the POWHEGBox generator at NLO in QCD with the  
1235 s-channel production modeled in the five-flavor scheme with the NNPDF3.0nlo PDF set, while  
1236 the t-channel production is modeled in the four-flavor scheme with the NNPDF3.0nlo 4f [121]  
1237 PDF set. The  $t\bar{t}WW$  contributions are normalized to NLO theoretical cross section. All  
1238 single-top samples are interfaced with PYTHIA8.230 [122] using the A14 tune [123] and the  
1239 NNPDF2.3lō [141] PDF set.

1240  **$tWZ$  +jets background**

1241 The  $tWZ$  sample is generated using MADGRAPH5\_AMC@NLO [120] at NLO in QCD  
1242 with the NNPDF3.0nlo [121] PDF set, interfaced with PYTHIA8.212 [122] using the A14 tune  
1243 [123] and the NNPDF2.3lō [141] PDF set.

1244  **$tZ$  &  $t\bar{t}VV$  background**

1245 Production of  $tZ$  is modeled using MADGRAPH5\_AMC@NLO [120] at NLO in QCD  
1246 with scale of  $H_T/6$  and the NNPDF3.0nlo 4f [121] PDF set. Production of  $t\bar{t}WW$  is modeled

1247 using `MADGRAPH5_AMC@NLO` [120] at LO, while production of  $t\bar{t}WZ$ ,  $t\bar{t}HH$ ,  $t\bar{t}WH$  and  
1248  $t\bar{t}ZZ$  are modeled using `MADGRAPH` at LO. All  $t\bar{t}VV$  samples use the `NNPDF3.0nlo` [121]  
1249 PDF set, and all samples in this section are interfaced with `PYTHIA8` [122] using the A14  
1250 tune [123].

### 1251 Single boson ( $V$ ) +jets background

1252 Production of  $V$ +jets is modeled with `SHERPA v2.2.10` [128] using NLO ME for up to two  
1253 jets and LO ME for up to four jets, with the `NNPDF3.0nlo` [121] PDF set. Matrix elements  
1254 are calculated with the Comix [147] and OpenLoops libraries [134, 135] and matched with  
1255 the `SHERPA` PS based on Catani-Seymour dipole factorization [129] using the MEPS@NLO  
1256 prescription [130–133]. The sample is normalized to NNLO [148] theoretical cross section.

### 1257 Diboson ( $VV$ ) +jets background

1258 Diboson samples are simulated with `SHERPA v2.2.14` [128] with the `NNPDF3.0nlo` [121]  
1259 PDF set. Fully leptonic and semileptonic final states are generated using NLO ME for up to  
1260 one extra parton and LO ME for up to three extra parton emissions. Loop-induced processes  
1261 are generated using LO ME for up to one extra parton. Matrix elements are matched and  
1262 merged with the `SHERPA` PS based on Catani-Seymour dipole factorization [129] using the  
1263 MEPS@NLO prescription [130–133]. Virtual QCD ME corrections are provided by the  
1264 OpenLoops library [134, 135].

### 1265 Triboson ( $VVV$ ) +jets background

1266 The triboson sample is modeled with `SHERPA v2.2.10` [128] using factorized gauge boson  
1267 decays. Matrix elements for the inclusive process at NLO and up to two extra partons at

1268 LO are matched and merged with the SHERPA PS based on Catani-Seymour dipole factor-  
1269 ization [129] using the MEPS@NLO prescription [130–133]. Virtual QCD ME corrections  
1270 are provided by the OpenLoops library [134, 135].

1271 ***VH* background**

1272 Generation of  $WH$  and  $ZH$  samples is performed using PowhegBox [137–140] at NLO  
1273 with the NNPDF3.0aznlo [121] PDF set, interfaced with PYTHIA8.230 [122] using the A14  
1274 tune [123] and the NNPDF2.3lō [141] PDF set. The samples are normalized to theoretical  
1275 cross sections at NNLO in QCD and NLO in EW accuracies.

<sub>1276</sub> **Chapter 6. Analysis Strategy**

<sub>1277</sub> **6.1 Event selection**

<sub>1278</sub> Events for the analysis first are preselected following a list of criteria to optimize for event  
<sub>1279</sub> quality and background rejection. The following criteria are applied sequentially from top  
<sub>1280</sub> to bottom along with cleaning and veto cuts

- <sub>1281</sub> 1. **Good Run List (GRL)**: data events must be part of a predefined list of suitable  
<sub>1282</sub> runs and luminosity blocks [[149](#)].
- <sub>1283</sub> 2. **Primary vertex**: events must have at least one reconstructed vertex matched to 2 or  
<sub>1284</sub> more associated tracks with  $p_T > 500$  MeV.
- <sub>1285</sub> 3. **Trigger**: events must be selected by at least one trigger in Table 5.1.
- <sub>1286</sub> 4. **Kinematic selection**: events must have exactly two *Tight* leptons with the same  
<sub>1287</sub> electric charge, or at least three *Tight* leptons of any charge. The leading lepton must  
<sub>1288</sub> have  $p_T > 28$  GeV, and all leptons must satisfy  $p_T > 15$  GeV.

<sub>1289</sub> Events are separated into two channels based on the number of leptons: same-sign di-  
<sub>1290</sub> lepton (SS2L) for events with exactly two leptons of the same charge, or multilepton (ML)  
<sub>1291</sub> for events with three or more leptons. The channels are further separated into regions defined  
<sub>1292</sub> in section 6.2 to prepare for analysis.

<sub>1293</sub> Additional selections are applied based on the lepton flavors present. In the SS2L channel,  
<sub>1294</sub> if both leptons are electrons, the invariant mass  $m_{ll}$  must satisfy  $m_{ll} < 81$  GeV and  $m_{ll} > 101$   
<sub>1295</sub> GeV to suppress background involving  $Z$ -bosons. In the ML channel, the same criteria must  
<sub>1296</sub> be satisfied for every opposite-sign same-flavor pair of leptons in an event.

### 1297 6.1.1 Event categorization

1298 Simulated events are categorized using truth information of leptons ( $e/\mu$ ) and their orig-  
1299 inating MC particle (mother-particle). Each lepton can be classified as either prompt or  
1300 non-prompt, with non-prompt leptons further categorized for background estimation pur-  
1301 poses. If an event contains only prompt leptons, the event is classified as its correspond-  
1302 ing process. If the event contains one non-prompt lepton, the event is classified as the corre-  
1303 sponding type of the non-prompt lepton. If the event contains more than one non-prompt  
1304 lepton, the event is classified as other.

1305 • **Prompt:** if the lepton originates from  $W/Z/H$  boson decays, or from a mother-  
1306 particle created by a final state photon.

1307 • **Non-prompt:**

1308 – **Charge-flip ( $e$  only):** if the reconstructed charge of the lepton differs from that  
1309 of the first mother-particle.

1310 – **Material conversion ( $e$  only):** if the lepton originated from a photon conversion  
1311 and the mother-particle is an isolated prompt photon, non-isolated final state  
1312 photon, or heavy boson.

1313 –  **$\gamma^*$ -conversion ( $e$  only):** if the lepton originated from a photon conversion and  
1314 the mother-particle is a background electron.

1315 – **Heavy flavor decay:** if the lepton originated from a  $b$ - or  $c$ -hadron.

1316 – **Fake:** if the lepton originated from a light- or  $s$ -hadron, or if the truth type of  
1317 the lepton is hadron.

1318 – **Other:** any lepton that does not belong to one of the above categories.

## 1319 6.2 Analysis regions

1320 Events are selected and categorized into analysis regions belonging to one of two types:  
 1321 control regions (CRs) enriched in background events, and signal regions (SRs) enriched in  
 1322 signal events. This allows for the examination and control of backgrounds and systematic  
 1323 uncertainties, as well as study of signal sensitivities. The signal is then extracted from the  
 1324 SRs with a profile LH fit using all regions. The full selection criteria for each region are  
 1325 summarized in Table 6.1. The post-fit background compositions in different CRs and SR  
 1326 sub-regions are shown in Figure 6.1.

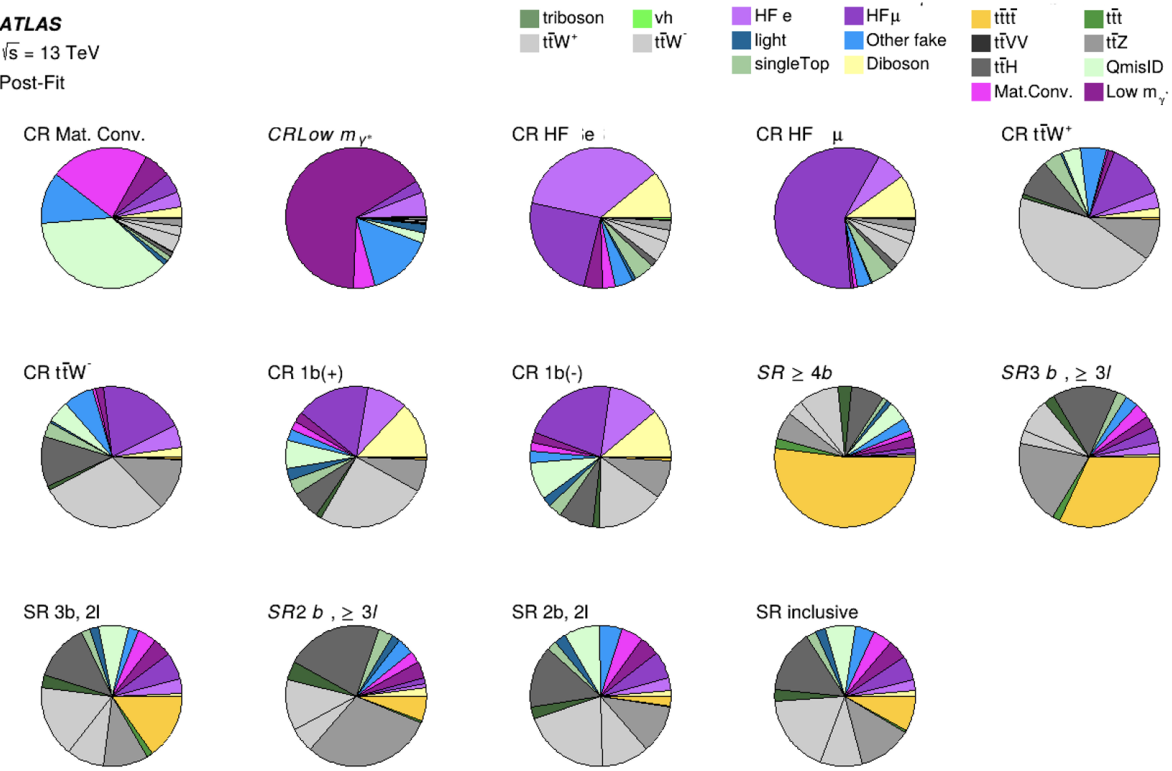


Figure 6.1: Post-fit background composition in each analysis region and sub-region. The fit was performed using ideal pseudo-datasets (Asimov data) in the SR.

Table 6.1: Definitions of signal, control and validation regions (VR) used in this analysis.  $N_{\text{jets}}$  and  $N_b$  refers to the number of jets and number of  $b$ -tagged jets respectively.  $\ell_1$  refers to the leading lepton,  $\ell_2$  refers to the subleading lepton and so on.  $H_T$  refers to the  $p_T$  scalar sum of all leptons and jets in the event.  $m_{\ell\ell}$  refers to the dilepton invariant mass, which must not coincide with the  $Z$ -boson mass range of 81-101 GeV for SS2L+3L events.

Region	Channel	$N_{\text{jets}}$	$N_b$	Other selections	Fitted variable
CR Low $m_{\gamma^*}$	SS $e\ell$	[4, 6)	$\geq 1$	$\ell_1/\ell_2$ is from virtual photon decay $\ell_1 + \ell_2$ not from material conversion	event yield
CR Mat. Conv.	SS $e\ell$	[4, 6)	$\geq 1$	$\ell_1/\ell_2$ is from material conversion $\ell_1 + \ell_2$ not conversion candidates	event yield
CR HF $\mu$	$\ell\mu\mu$	$\geq 1$	1	$100 < H_T < 300$ GeV $E_T^{\text{miss}} > 35$ GeV total charge = $\pm 1$	$p_T(\ell_3)$
CR HF $e$	$e\ell\ell$	$\geq 1$	1	$\ell_1 + \ell_2$ not conversion candidates $100 < H_T < 275$ GeV $E_T^{\text{miss}} > 35$ GeV total charge = $\pm 1$	$p_T(\ell_3)$
CR $t\bar{t}W^+$	SS $\ell\mu$	$\geq 4$	$\geq 2$	$ \eta(e)  < 1.5$ for $N_b = 2$ : $H_T < 500$ GeV or $N_{\text{jets}} < 6$ for $N_b \geq 3$ : $H_T < 500$ GeV total charge > 0	$N_{\text{jets}}$
CR $t\bar{t}W^-$	SS $\ell\mu$	$\geq 4$	$\geq 2$	$ \eta(e)  < 1.5$ for $N_b = 2$ : $H_T < 500$ GeV or $N_{\text{jets}} < 6$ for $N_b \geq 3$ : $H_T < 500$ GeV total charge < 0	$N_{\text{jets}}$
CR 1b(+)	SS2L+3L	$\geq 4$	1	$\ell_1 + \ell_2$ not from material conversion $H_T > 500$ GeV total charge > 0	$N_{\text{jets}}$
CR 1b(-)	SS2L+3L	$\geq 4$	1	$\ell_1 + \ell_2$ not from material conversion $H_T > 500$ GeV total charge < 0	$N_{\text{jets}}$
VR $t\bar{t}Z$	3L $\ell^\pm\ell^\mp$	$\geq 4$	$\geq 2$	$m_{\ell\ell} \in [81, 101]$ GeV	$N_{\text{jets}}, m_{\ell\ell}$
VR $t\bar{t}W +1b$	SS2L+3L			CR $t\bar{t}W^\pm$    CR 1b( $\pm$ )	$N_{\text{jets}}$
VR $t\bar{t}W +1b+SR$	SS2L+3L			CR $t\bar{t}W^\pm$    CR 1b( $\pm$ )    SR	$N_{\text{jets}}$
SR	SS2L+3L	$\geq 6$	$\geq 2$	$H_T > 500$ GeV $m_{\ell\ell} \notin [81, 101]$ GeV	$H_T$

### 1327 6.2.1 Signal regions

1328 All events selected for the SR must satisfy the following criteria:

- 1329 Contains 6 or more jets, with at least 2 jets  $b$ -tagged at the 85% OP.
- 1330 Scalar sum of the transverse momenta of all leptons and jets  $H_T > 500$  GeV.
- 1331 Dilepton invariant mass  $m_{\ell\ell}$  does not coincide with the  $Z$ -boson mass range of 81 – 101 1332 GeV

1333 The SR is further divided into sub-regions by the number of  $b$ -tagged jets and leptons 1334 present to study signal behavior and sensitivity with respect to the selection variables.

Table 6.2: Definitions of SR sub-regions. Events are sorted into different sub-regions based on the number of  $b$ -tagged jets and leptons present.

Sub-region	Selection criteria	
	$b$ -jets	leptons
SR 2b2l	$N_b = 2$	$N_l = 2$
SR 2b3l4l	$N_b = 2$	$N_l \geq 3$
SR 3b2l	$N_b = 3$	$N_l = 2$
SR 3b3l4l	$N_b = 3$	$N_l \geq 3$
SR 4b	$N_b \geq 4$	

### 1335 Signal extraction

1336 Signal extraction in the SR is performed via a binned profile likelihood (LH) fit as de-  
1337 scribed in section 8.1 using  $H_T$  as the discriminant observable. The discriminant observable

1338 for a LH fit serves as the set of observed data upon which the LH function is constructed.

1339 Ideally, the chosen observable shows significant separation between the functional forms of  
1340 the signal and background distributions, allowing for effective separation of the two. Fig-

1341 ure 6.2 shows several pre-fit kinematic distributions in the inclusive SR. From empirical

1342 optimization studies,  $H_T$  possesses good discriminating power compared to other observ-  
1343 ables constructed using event-level information.

1344 **6.2.2 Control regions**

1345 Control regions are defined for each background to be enriched in the targeted process, in  
1346 order to maximize the background's purity and minimize contamination from other sources  
1347 within the region. This helps to constrain and reduce correlation between background nor-  
1348 malization factors in the final fit. Fit variables and selection criteria are determined via  
1349 optimization studies performed on CRs that aimed to achieve the largest discriminating  
1350 power possible between the target background and other event types.

1351  **$t\bar{t}W$  background CRs**

1352 Theoretical modeling for  $t\bar{t}W + \text{jets}$  background in the phase space of this analysis suffers  
1353 from large uncertainties, especially at high jet multiplicities [150]. A data-driven method was  
1354 employed in a similar manner to the SM  $t\bar{t}\bar{t}\bar{t}$  observation analysis [44] to mitigate this effect,  
1355 and are described in further details in section 6.3.3. The method necessitates the definition  
1356 of two groups of dedicated CRs to estimate the flavor composition and normalization of  $t\bar{t}W$   
1357 + jets background: CR  $t\bar{t}W + \text{jets}$  to constrain flavor composition, and CR 1b to constrain  
1358 the jet multiplicity spectrum. These are further split into CR  $t\bar{t}W^\pm$  and CR 1b( $\pm$ ) due to  
1359 the pronounced asymmetry in  $t\bar{t}W$  production from  $pp$  collisions, with  $t\bar{t}W^+$  being produced  
1360 at approximately twice the rate of  $t\bar{t}W^-$  [151].

1361 Events in CR  $t\bar{t}W^\pm$  are required to contain at least two  $b$ -tagged jets similar to the SR  
1362 to determine the  $t\bar{t}W$  normalization within an SR-related phase space. Orthogonality with  
1363 SR is ensured by requiring  $H_T < 500$  GeV or  $N_{\text{jets}} < 6$  when  $N_b = 2$ , and  $H_T < 500$

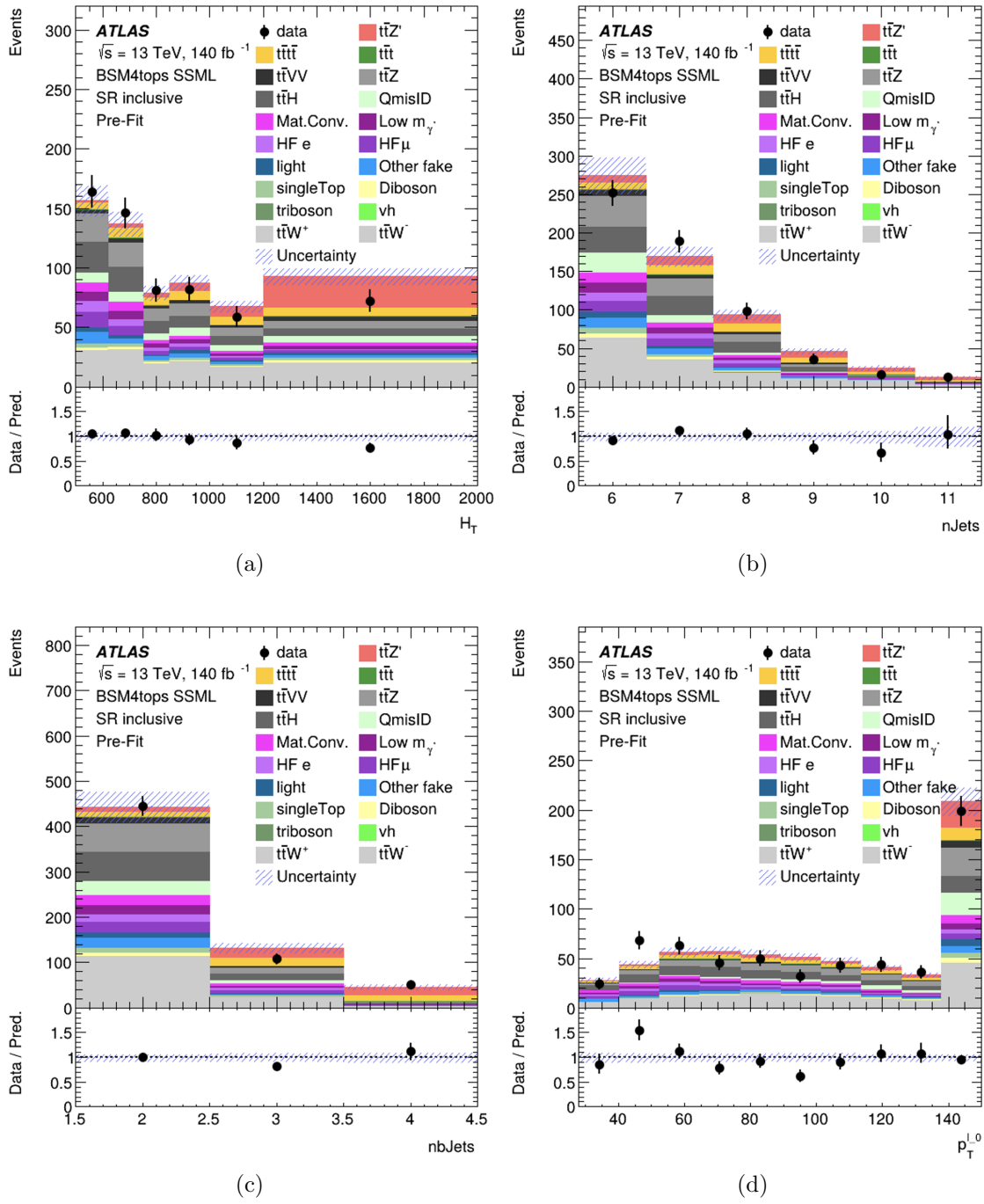


Figure 6.2: Pre-fit kinematic distributions and event compositions in the inclusive SR for (a)  $H_T$  i.e. scalar sum of  $p_T$  of all objects in the event, (b) jet multiplicity, (c)  $b$ -jet multiplicity, (d) leading lepton  $p_T$ . The shaded band represents the uncertainty in the total distribution. The first and last bins of each distribution contain underflow and overflow events respectively.

1364 GeV when  $N_b \geq 3$ . Events in CR 1b( $\pm$ ) are required to have  $H_T > 500$  GeV and at least  
 1365 four jets to encompass events with high  $N_{\text{jets}}$ , which can be used to determine the  $t\bar{t}W$  jet  
 1366 multiplicity spectrum for fitting  $a_{0,1}$ . The selection criteria also include exactly one  $b$ -tagged  
 1367 jet to maintain orthogonality with the SR.

### 1368 **Fake/non-prompt background CRs**

1369 Selection for fake/non-prompt CRs are determined using the `DFCommonAddAmbiguity`  
 1370 (`DFCAA`) variable for reconstructed leptons.

Table 6.3: List of possible assigned values for DFCAA.

DFCAA	Description
-1	No 2nd track found
0	2nd track found, no conversion found
1	Virtual photon conversion candidate
2	Material conversion candidate

1371 Four CRs are defined for the three main types of fake/non-prompt backgrounds in the  
 1372 analysis - virtual photon ( $\gamma^*$ ) conversion, photon conversion in detector material (Mat.  
 1373 Conv.) and heavy flavor decays (HF). The full selection criteria for fake/non-prompt CRs  
 1374 are shown in Table 6.1.

- 1375 • **Low  $m_\gamma^*$ :** events with an  $e^+e^-$  pair produced from a virtual photon.

1376 Events are selected if there are two same-sign leptons with at least one electron recon-  
 1377 structed as an internal conversion candidate, and neither reconstructed as a material  
 1378 conversion candidate.

- 1379 • **Mat. Conv.:** events with an electron originating from photon conversion within the  
 1380 detector material.

1381 Events are selected if there are two same-sign leptons with at least one electron recon-  
1382 structed as a material conversion candidate.

1383 • **HF  $e(\mu)$ :** events with a reconstructed non-prompt lepton from semi-leptonic decays of  
1384  $b$ - and  $c$ -hadrons (heavy flavor decays).

1385 Events are selected if there are three leptons with at least two electrons (muons), with  
1386 no lepton reconstructed as a conversion candidate.

## 1387 6.3 Background estimation

1388 Background in this analysis consist of SM processes that can result in a signal signature  
1389 similar to a  $t\bar{t}t\bar{t}$  SSML final state and can be divided into two types, reducible and irreducible.

1390 Reducible background consists of processes that do not result in a SSML final state physically,  
1391 but are reconstructed as such due to detector and reconstruction effects. The main types  
1392 of reducible background considered are charge misidentification (QmisID) and fake/non-  
1393 prompt leptons. Fake/non-prompt lepton backgrounds contaminate the SR when a non-  
1394 prompt lepton is reconstructed as a prompt lepton in a  $t\bar{t}$ -associated process, leading to  
1395 a similar final state to that of SSML  $t\bar{t}t\bar{t}$ . These backgrounds are estimated using the  
1396 template fitting method described in subsection 6.3.1, where MC simulations are normalized  
1397 to their theoretical SM cross section via floating normalization factors (NFs) constrained by  
1398 the corresponding CRs. Lepton charge misidentification background contaminates the SR  
1399 similarly when one of the two leptons in a  $t\bar{t}$ -associated process with two opposite-sign leptons

1400 is misidentified, producing a SS2L  $t\bar{t}t\bar{t}$  final state. Charge misidentification background is  
1401 estimated using a data-driven method described in section 6.3.2 along with ECIDS described  
1402 in section 4.3.1.

1403 Irreducible background consists of SM processes that result in SSML final states physi-  
1404 cally with all leptons being prompt. The dominating background in the SR are SM  $t\bar{t}t\bar{t}$ ,  $t\bar{t}W$ ,  
1405  $t\bar{t}Z$ , and  $t\bar{t}H$  production with smaller contributions from  $VV$ ,  $VVV$ ,  $VH$  and rarer processes  
1406 like  $t\bar{t}VV$ ,  $tWZ$ ,  $tZq$  and  $t\bar{t}t$ . Most irreducible backgrounds are estimated using template  
1407 fitting method, with the exception of  $t\bar{t}W + \text{jets}$  background. The  $t\bar{t}W + \text{jets}$  background is  
1408 instead given four dedicated CRs, and estimated using a data-driven method with a fitted  
1409 function parameterized in  $N_{\text{jets}}$ . All CRs and SR are included in the final profile LH fit to  
1410 data.

### 1411 6.3.1 Template fitting for fake/non-prompt estimation

1412 Template fitting method is a semi-data-driven approach [150] that estimates fake/non-  
1413 prompt background distributions by fitting the MC kinematic profile of background processes  
1414 arising from fake/non-prompt leptons to data. The four main sources of fake/non-prompt  
1415 leptons are generated from  $t\bar{t} + \text{jets}$  samples and are constrained by four CRs enriched with  
1416 the corresponding backgrounds. Each of the aforementioned background is assigned a free-  
1417 floating NF resulting in  $\text{NF}_{\text{HF } e}$ ,  $\text{NF}_{\text{HF } \mu}$ ,  $\text{NF}_{\text{Mat. Conv.}}$  and  $\text{NF}_{\text{Low } m_{\gamma^*}}$ . The NFs are fitted  
1418 simultaneously with the signal within their constraining CRs.

### 1419 6.3.2 Charge misidentification data-driven estimation

1420 The  $ee$  and  $e\mu$  channels in the SS2L  $t\bar{t}t\bar{t}$  region are contaminated with opposite-sign  
1421 (OS) dilepton  $t\bar{t}$ -associated events where one electron has its charge misidentified. Charge  
1422 misidentification (QmisID) largely affects electrons due to muons' precise curvature informa-  
1423 tion using ID and MS measurements and low bremsstrahlung rate. The charge flip rates are

<sub>1424</sub> significant at higher  $p_T$  and varies with  $|\eta|$  which is proportional to the amount of detector  
<sub>1425</sub> material the electron interacted with.

<sub>1426</sub> The charge flip probability  $\epsilon$  is estimated in this analysis with a data-driven method  
<sub>1427</sub> [152] using a sample of  $Z \rightarrow e^+e^-$  events with additional constraints on the invariant mass  
<sub>1428</sub>  $m_{ee}$  to be within 10 GeV of the  $Z$ -boson mass. The  $Z$ -boson mass window is defined to  
<sub>1429</sub> be within  $4\sigma$  to include most events within the peak, and is determined by fitting the  $m_{ee}$   
<sub>1430</sub> spectrum of the two leading electrons to a Breit-Wigner function, resulting in a range of  
<sub>1431</sub> [65.57, 113.49] for SS events and [71.81, 109.89] for OS events. Background contamination  
<sub>1432</sub> near the peak is assumed to be uniform and subtracted using a sideband method. Since the  
<sub>1433</sub>  $Z$ -boson decay products consist of a pair of opposite-sign electrons, all same-sign electron  
<sub>1434</sub> pairs are considered affected by charge misidentification.

<sub>1435</sub> Let  $N_{ij}^{\text{SS}}$  be the number of events with SS electrons with the leading electron in the  
<sub>1436</sub>  $i^{\text{th}}$  2D bin in  $(p_T, |\eta|)$  and the sub-leading electron in the  $j^{\text{th}}$  bin. Assuming the QmisID  
<sub>1437</sub> probabilities of electrons in an event are uncorrelated,  $N_{ij}^{\text{SS}}$  can be estimated as

$$N_{ij}^{\text{SS}} = N_{ij}^{\text{tot}} [\epsilon_i(1 - \epsilon_j) + \epsilon_j(1 - \epsilon_i)], \quad (6.1)$$

<sub>1438</sub> where  $N_{ij}^{\text{tot}}$  is the total number of events in the  $i^{\text{th}}$  and  $j^{\text{th}}$  bin regardless of charge, and  
<sub>1439</sub>  $\epsilon_{i(j)}$  is the QmisID rate in the  $i^{\text{th}}(j^{\text{th}})$  bin. Assuming  $N_{ij}^{\text{SS}}$  follows a Poisson distribution  
<sub>1440</sub> around the expectation value  $\bar{N}_{ij}^{\text{SS}}$ , the  $(i, n)^{\text{th}}$  rate  $\epsilon$  can be estimated by minimizing a  
<sub>1441</sub> negative-LLH function parameterized in  $p_T$  and  $|\eta|$ ,

$$\begin{aligned}
-\ln(\mathcal{L}(\epsilon|N_{\text{SS}})) &= -\ln \prod_{ij} \frac{(N_{ij}^{\text{tot}})^{N_{ij}^{\text{SS}}} \cdot e^{N_{ij}^{\text{tot}}}}{N_{ij}^{\text{SS}}!} \\
&= -\sum_{ij} \left[ N_{ij}^{\text{SS}} \ln(N_{ij}^{\text{tot}}(\epsilon_i(1-\epsilon_j) + \epsilon_j(1-\epsilon_i))) - N_{ij}^{\text{tot}}(\epsilon_i(1-\epsilon_j) + \epsilon_j(1-\epsilon_i)) \right]. \tag{6.2}
\end{aligned}$$

1442 The QmisID rates are then calculated separately for SR and CRs with different electron  
 1443 definitions i.e. CR Low  $m_{\gamma^*}$ , CR Mat. Conv., CR  $t\bar{t}W^\pm$ , using events from data after  
 1444 applying region-specific lepton selections and ECIDS. The events are required to satisfy  
 1445 SS2L kinematic selections but contains OS electrons. The following weight is applied to OS  
 1446 events to correct for misidentified SS events within the region,

$$w = \frac{\epsilon_i + \epsilon_j - 2\epsilon_i\epsilon_j}{1 - \epsilon_i - \epsilon_j + 2\epsilon_i\epsilon_j}. \tag{6.3}$$

1447 The QmisID rates calculated for SR and CR  $t\bar{t}W$  are shown in Figure 6.3

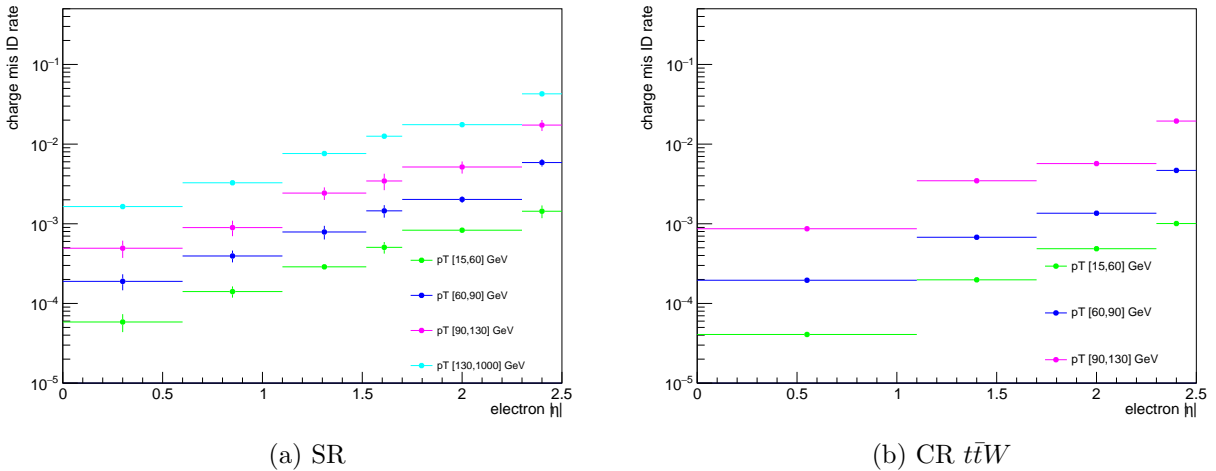


Figure 6.3: Charge flip rate calculated for SR and CR  $t\bar{t}W$  in bins of  $|\eta|$  and  $p_T$ .

1448        The QmisID rates obtained after applying  $w$  contain a dependency on jet multiplicity  
 1449        and are underestimated at higher  $N_{\text{jets}}$ . This dependency affect the SR which require events  
 1450        with  $\geq 6$  jets, and is corrected by applying a correction factor  $SF_{i,n} = \epsilon_{i,n}/\epsilon_{i,N}$  where  $N$  is  
 1451        the inclusive bin containing all  $N_{\text{jets}}$  and  $\epsilon_{i,n}$  is the QmisID rate obtained from Equation 6.2  
 1452        in the  $(i, n)^{\text{th}}$  2D bin in  $(p_{\text{T}}, N_{\text{jets}})$ . Jet multiplicity and consequently the obtained SFs are  
 1453        assumed to be independent of  $|\eta|$ .

### 1454        6.3.3 $t\bar{t}W$ background data-driven estimation

1455        Previously, the  $t\bar{t}W$  background in  $t\bar{t}t\bar{t}$  final state analysis was handled by assigning large  
 1456        ad-hoc systematic uncertainties to  $t\bar{t}W$  events with 7 or more jets [46]. A semi-data-driven  
 1457        method [153] was shown to be effective in the SM  $t\bar{t}t\bar{t}$  observation analysis [44] by improving  
 1458         $t\bar{t}W$  modeling, especially in the showering step and switching  $t\bar{t}W$  systematic uncertainties  
 1459        from predominantly modeling to statistical.

1460        The data-driven method applies correction factors obtained from a fitted function pa-  
 1461        rameterized in  $N_{\text{jets}}$  to  $t\bar{t}W$  MC kinematic distibutions. The QCD scaling patterns [154] can  
 1462        be represented by ratio of successive exclusive jet cross-sections

$$R_{(n+1)/n} = \frac{\sigma_{n+1}}{\sigma_n} = e^{-b} + \frac{\bar{n}}{n+1} = a_0 + \frac{a_1}{1+(j-4)}, \quad (6.4)$$

1463        where  $a_{0(1)}$  and  $b$  are constants,  $n$  is the number of jets in addition to the hard process,  $j$   
 1464        is the inclusive number of jets, and  $\bar{n}$  is the expectation value for the Poisson distribution  
 1465        of exclusive jet cross-section at jet multiplicity  $n$ . The  $t\bar{t}W$  ME for SS2L events gives 4 jets  
 1466        in the hard process, so  $n$  is defined starting from the 5<sup>th</sup> jets and the inclusive number of  
 1467        jets  $j = n + 4$ . The two terms in Equation 6.4 correspond to staircase and Poisson scaling

<sub>1468</sub> in cross section between successive jet multiplicities and are sensitive to high and low jet  
<sub>1469</sub> multiplicity events respectively [154]. The scaling pattern can then be reparameterized in  
<sub>1470</sub>  $a_0$  and  $a_1$  to obtain the  $t\bar{t}W$  yield at  $j' \equiv j + 1$  jets

$$\text{Yield}_{t\bar{t}W(j')} = \text{Yield}_{t\bar{t}W(N_{\text{jets}}=4)} \times \prod_{j=4}^{j'-1} \left( a_0 + \frac{a_1}{1+(j-4)} \right) \quad (6.5)$$

<sub>1471</sub> with  $j \geq 4$ . The  $t\bar{t}W$  yield in the 4-jet bin can be represented by a NF applied to  $t\bar{t}W$  MC  
<sub>1472</sub> simulation

$$\text{Yield}_{t\bar{t}W(N_{\text{jets}}=4)} = \text{NF}_{t\bar{t}W(N_{\text{jets}}=4)} \times \text{MC}_{t\bar{t}W(N_{\text{jets}}=4)}. \quad (6.6)$$

<sub>1473</sub> To account for the asymmetry in  $t\bar{t}W^+$  and  $t\bar{t}W^-$  cross-sections,  $\text{NF}_{t\bar{t}W(N_{\text{jets}}=4)}$  is further  
<sub>1474</sub> split into  $\text{NF}_{t\bar{t}W^\pm(N_{\text{jets}}=4)}$  assuming the scaling is the same for both processes. Both NFs  
<sub>1475</sub> are left free-floating to constrain  $t\bar{t}W$  yields in the 4-jet bin within CR 1b(+) and CR 1b(-).  
<sub>1476</sub> The final  $N_{\text{jets}}$ -parameterized function can then be represented by  $\text{NF}_{t\bar{t}W(j')}$  as

$$\text{NF}_{t\bar{t}W(j')} = \left( \text{NF}_{t\bar{t}W^+(N_{\text{jets}}=4)} + \text{NF}_{t\bar{t}W^-(N_{\text{jets}}=4)} \right) \times \prod_{j=4}^{j'-1} \left( a_0 + \frac{a_1}{1+(j-4)} \right). \quad (6.7)$$

<sub>1477</sub> The normalization is calculated and applied separately for each sub-sample of  $t\bar{t}W^+$  and  
<sub>1478</sub>  $t\bar{t}W^-$  in a  $N_{\text{jets}}$  bin for  $4 \leq N_{\text{jets}} < 10$ . Due to small contributions in the CRs, events  
<sub>1479</sub> with  $N_{\text{jets}} < 4$  and  $N_{\text{jets}} \geq 10$  are not normalized with this scheme. Instead,  $N_{\text{jets}} < 4$   
<sub>1480</sub> events are fitted by propagating the normalization in the 4-jet bin without additional shape  
<sub>1481</sub> correction. The correction factor for  $t\bar{t}W$  events with  $N_{\text{jets}} \geq 10$  is obtained by summing  
<sub>1482</sub> up the overflow from  $N_{\text{jets}} = 10$  to  $N_{\text{jets}} = 12$ , described as  $\sum_{j'=10}^{12} \prod_{j=4}^{j'-1} \left( a_0 + \frac{a_1}{1+(j-4)} \right)$ .  
<sub>1483</sub> Events with  $N_{\text{jets}} \geq 13$  are negligible and are not included in the sum.

1484      The four regions, CR  $t\bar{t}W^\pm$  and CR 1b( $\pm$ ), are constructed to fit  $NF_{t\bar{t}W^\pm(N_{\text{jets}}=4)}$  and  
1485 the scaling parameters  $a_{0(1)}$ , as well as validating the parameterization. Assuming the  $N_{\text{jets}}$   
1486 distribution of  $t\bar{t}W$  is similar across bins of  $N_b$ -jets, a fitted  $N_{\text{jets}}$  distribution in CR 1b( $\pm$ )  
1487 can be used to describe the  $t\bar{t}W$  parameterization at higher  $N_{\text{jets}}$ .

# 1488 Chapter 7. Systematic Uncertainties

1489 Physics analysis inherently incurs uncertainties in the form of statistical and systematic  
1490 uncertainties, depending on the source. Statistical uncertainties occur in this analysis from  
1491 sample size of collected data and simulated MC samples, and from the maximizing of the  
1492 LH function. Systematic uncertainties depend on identifiable sources in the analysis i.e.  
1493 from detector and reconstruction effects (experimental uncertainties) or theoretical modeling  
1494 (theoretical uncertainties). Systematic uncertainties are represented as nuisance parameters  
1495 ( $NP_x$ ) in the profile LH fit. During the fit, systematic uncertainties with negligible impact  
1496 on the final results can be pruned to simplify the statistical model and reduce computational  
1497 complexity. This section outlines all uncertainties considered in this analysis.

## 1498 7.1 Experimental uncertainties

### 1499 7.1.1 Luminosity & pile-up reweighting

1500 The uncertainty on the integrated luminosity of the 2015-2018 Run 2 data set is 0.83%  
1501 [88], obtained by the LUCID-2 detector [155] for the primary luminosity measurements and  
1502 complemented by the ID and calorimeters. Pile-up was modeled in MC and calibrated  
1503 to data through pile-up reweighting, resulting in a set of calibration SFs and associated  
1504 uncertainties.

### 1505 7.1.2 Leptons

1506 In general, calibrating MC simulations to match performance in data incurs uncertainties  
1507 associated obtaining the MC-to-data calibration SFs, which are in turn propagated to observ-

ables in the analysis. The data-to-MC calibration of trigger, reconstruction, identification and isolation efficiencies for electrons and muons incur associated uncertainties, with separate systematic and statistical components for those related to muons. Similarly, electron energy scale, muon momentum scale and resolution are also subjected to calibration uncertainties estimated by re-simulating the events while varying the energy/momenta scale and resolution. Electron has an additional uncertainty related to ECIDS efficiency. Muon has additional uncertainties for charge-independent and charge-dependent momentum scale, as well as detector-specific track resolution. Systematic uncertainties for electron reconstruction, identification, isolation, ECIDS efficiencies and muon ID/MS energy resolution were not ready for the sample version used in this analysis, and are therefore not included.

### 7.1.3 Jets

Experimental uncertainties for jets are dominated by flavor tagging-related uncertainties, with subleading contributions from uncertainties related to JES [111], JER [110] and JVT [156] calibrations.

#### Jet energy scale

Uncertainties associated with JES are determined using data from LHC collisions along with MC simulated samples [111], decomposed into uncorrelated components:

- **Effective NPs:** 15 total  $p_T$ -dependent uncertainty components measured in situ, grouped based on their origin (2 detector-related, 4 modeling-related, 3 mixed, 6 statistical-related)
- **$\eta$  intercalibration:** 6 total components (1 modeling-related, 4 non-closure and 1

1529 statistical-related) associated with the correction of the forward jets' ( $0.8 \leq |\eta| < 4.5$ )  
1530 energy scale to that of the central jets ( $|\eta| < 0.8$ ).

1531 • **Flavor composition & response:** 2 components for relative quark-gluon flavor com-  
1532 positions in background and signal samples, and 2 components for responses to gluon-  
1533 initiated versus quark-initiated jets.

1534 • **Pile-up subtraction:** 4 components, 2 for  $\mu$  (`OffsetMu`) and  $N_{\text{PV}}$  (`OffsetNPV`) mod-  
1535 eling, 1 for residual  $p_{\text{T}}$ -dependency (`PtTerm`) and 1 for topology dependence on the  
1536 per-event  $p_{\text{T}}$  density modeling (`RhoTopology`).

1537 • **Punch-through effect treatment:** 2 terms for GSC punch-through jet response  
1538 deviation between data and MC, one for each detector response simulation method  
1539 (AF3 and FS).

1540 • **Non-closure:** 1 term applied to AF3 sample to account for the difference between  
1541 AF3 and FS simulation.

1542 • **High- $p_{\text{T}}$  single-particle response:** 1 term for the response to high- $p_{\text{T}}$  jets from  
1543 single-particle and test-beam measurements.

1544 •  **$b$ -jets response:** 1 term for the difference between  $b$ -jets and light-jets response.

## 1545 Jet energy resolution

1546 Measurements of JER were performed in bins of  $p_{\text{T}}$  and  $\eta$ , separately in data using in-  
1547 situ techniques and in MC simulation using dijet events [110]. This analysis uses the full  
1548 correlation JER uncertainty scheme provided for Run 2 analysis with 14 total components:

<sub>1549</sub> 12 for effective NPs and 2 for difference between data and MC, separately for AF3 and FS  
<sub>1550</sub> [110].

### <sub>1551</sub> **Jet vertex tagging**

<sub>1552</sub> The uncertainty associated with JVT is obtained by varying the JVT efficiency SFs  
<sub>1553</sub> within their uncertainty range [156]. This uncertainty accounts for remaining contamination  
<sub>1554</sub> from pile-up jets after applying pile-up suppression and MC generator choice.

### <sub>1555</sub> **Flavor tagging**

<sub>1556</sub> Calibration SFs for  $b$ -tagging efficiencies and  $c$ -/light-jets mistagging rates are derived as  
<sub>1557</sub> a function of  $p_T$  for  $b$ -,  $c$ -, light-jets and PCBT score. The full set of flavor tagging-related  
<sub>1558</sub> uncertainties was reduced in dimensions by diagonalizing the uncertainty covariance matrix  
<sub>1559</sub> via eigendecomposition [114], resulting in a compact set of orthogonal NPs for this analysis:  
<sub>1560</sub> 85 for  $b$ -jets, 56 for  $c$ -jets and 42 for light-jets.

#### <sub>1561</sub> **7.1.4 Missing transverse energy**

<sub>1562</sub> Uncertainties on  $E_T^{\text{miss}}$  arise from possible mis-calibration of the soft-track component  
<sub>1563</sub> and are estimated using data-to-MC comparison of the  $p_T$  scale and resolution between  
<sub>1564</sub> the hard and soft  $E_T^{\text{miss}}$  components [118]. These uncertainties are represented by three  
<sub>1565</sub> independent terms: 1 for scale uncertainty and 2 for resolution uncertainty of the parallel  
<sub>1566</sub> and perpendicular components.

<sub>1567</sub> **7.2 Modeling uncertainties**

<sub>1568</sub> **7.2.1 Signal and irreducible background uncertainties**

<sub>1569</sub> The signal and background samples used are modeled using MC simulation. Most uncer-  
<sub>1570</sub> tainties on simulation parameters (e.g. generator choice, PS model) are estimated by varying  
<sub>1571</sub> the relevant parameters and comparing them with the nominal sample. Uncertainties in-  
<sub>1572</sub> volving PDF in particular for most processes in the analysis are set to a flat 1% uncertainty.  
<sub>1573</sub> Cross-section uncertainties were considered for all irreducible background except  $t\bar{t}W$ , which  
<sub>1574</sub> is normalized in dedicated CRs following section 6.3.3. Extra uncertainties for the produc-  
<sub>1575</sub> tion of four or more  $b$ -jets (additional  $b$ -jets) in association with  $t\bar{t}X$  and HF jets were also  
<sub>1576</sub> considered due to a lack of theoretical predictions or dedicated measurements, rendering  
<sub>1577</sub> MC modeling challenging. Uncertainties from missing higher-order QCD corrections in MC  
<sub>1578</sub> simulation are estimated by varying the renormalization scale  $\mu_R$  and factorization scale  $\mu_F$   
<sub>1579</sub> within seven different combinations

$$(\mu_R, \mu_F) = \{(0.5, 0.5), (0.5, 1), (1, 0.5), (1, 1), (1, 2), (2, 1), (2, 2)\}.$$

<sub>1580</sub> Process-specific uncertainty treatments are detailed below.

<sub>1581</sub> **SM  $t\bar{t}t\bar{t}$  background**

<sub>1582</sub> The generator uncertainty for the SM  $t\bar{t}t\bar{t}$  background was evaluated between a nominal  
<sub>1583</sub> sample of MADGRAPH5\_AMC@NLO and SHERPA. The parton shower uncertainty was  
<sub>1584</sub> evaluated between PYTHIA8 and HERWIG. The cross-section uncertainty was estimated to

1585 be 20% computed from a prediction at NLO in QCD+EW [127].

## 1586 $t\bar{t}t$ background

1587 The cross-section uncertainty for  $t\bar{t}t$  was estimated to be 30% computed from a prediction  
1588 at NLO in QCD+EW [127]. Events with additional  $b$ -jets also incur a 50% uncertainty.

## 1589 $t\bar{t}W$ , $t\bar{t}Z$ , $t\bar{t}H$ backgrounds

1590 For  $t\bar{t}W$ ,  $t\bar{t}Z$  and  $t\bar{t}H$  backgrounds, an uncertainty of 50% is assigned to events with one  
1591 additional truth  $b$ -jets that did not originate from a top quark decay, and an added 50%  
1592 uncertainty is assigned to events with two or more [157] additional  $b$ -jets. The generator  
1593 uncertainty was estimated for  $t\bar{t}Z$  using a MADGRAPH5\_AMC@NLO nominal sample and  
1594 a SHERPA sample, and for  $t\bar{t}H$  using POWHEGBOX samples interfaced with PYTHIA8 (nom-  
1595 inal) and HERWIG7. Cross-section uncertainties of 12% and 10% were applied to  $t\bar{t}Z$  and  
1596  $t\bar{t}H$  respectively [158]. No  $t\bar{t}W$  cross-section or PDF uncertainty was considered since the  
1597 normalizations and jet multiplicity spectrum for  $t\bar{t}W$  are estimated using the data-driven  
1598 method described in section 6.3.3.

## 1599 Other backgrounds

1600 Other backgrounds include processes with small overall contribution in the SR. The  
1601 cross-section uncertainty for  $tZ$  and  $tWH$  is considered to be 30% [159, 160]. A conservative  
1602 cross-section uncertainty of 50% is applied to  $t\bar{t}VV$ ,  $VVV$  and  $VH$ . For  $VV$ , the cross-  
1603 section uncertainty is dependent on jet multiplicity and is considered to be 20%/50%/60%  
1604 for events with  $\leq 3/4 \geq 5$  jets [161]. For  $VV$ ,  $t\bar{t}VV$ ,  $VVV$  and  $VH$  events with additional  
1605 truth  $b$ -jets, an uncertainty of 50% is applied.

## 1606 7.2.2 Reducible background uncertainties

1607 Reducible backgrounds consist of  $t\bar{t}/V + \text{HF}$  jets and single top events. Reducible back-  
1608 ground has small contamination within the SR, thus uncertainties related to reducible back-  
1609 ground have minor impact. Treatment for reducible background in this analysis largely  
1610 follows Ref. [44], except for QmisID.

## 1611 Charge misidentification

1612 Uncertainties on the QmisID background originate from the charge flip rates obtained  
1613 using the data-driven method described in section 6.3.2. Four sources of uncertainty were  
1614 considered: statistical uncertainty from the maximum LLH estimation using Equation 6.2;  
1615 uncertainty from choice of the  $Z$ -mass window and sidebands; non-closure uncertainty de-  
1616 fined as the relative difference between the number of SS and OS events; and statistical  
1617 uncertainty from the  $N_{\text{jets}}$  dependency correction SFs. The combined uncertainties from  
1618 all four sources are calculated separately for each region involved in section 6.3.2, and are  
1619 treated as correlated across all regions. Figure 7.1 shows the uncertainty calculated for SR.

## 1620 Internal (low $\gamma^*$ ) and material conversion

1621 The normalization for internal and material conversion backgrounds are free parameters  
1622 in the fit, as a result the only uncertainties evaluated are from the shape of the distributions  
1623 used in the template fit method (see section 6.3.1). The uncertainties on internal (material)  
1624 conversion are estimated based on the difference between data and MC prediction in a region  
1625 enriched in  $Z + \gamma \rightarrow \mu^+\mu^- + e^+e^-$  events.

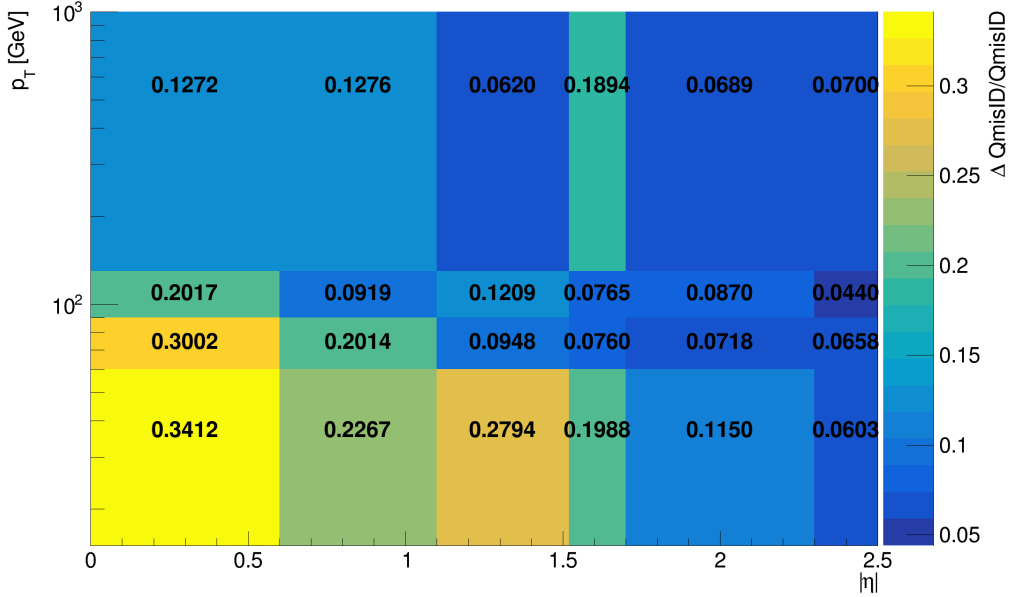


Figure 7.1: Combined QmisID uncertainty rate for SR in bins of  $|\eta|$  and  $p_T$ .

## 1626 Heavy-flavor non-prompt lepton

1627 Similar to the conversion backgrounds, the uncertainties on non-prompt HF decays come  
1628 from the shape of the distributions, and are estimated by comparing data and MC prediction  
1629 between all regions in the analysis on a per bin basis. The events used are required to  
1630 contain at least one *Loose* reconstructed lepton used in the region selection criteria detailed  
1631 in Table 6.1 to maintain orthogonality with the SR.

## 1632 Light-flavor decays and other fake/non-prompt backgrounds

1633 A conservative normalization uncertainty of 100% is assigned for light-flavor non-prompt  
1634 lepton background [150], and an ad-hoc normalization uncertainty of 30% is applied to all  
1635 other fake and non-prompt backgrounds. The shape uncertainties for these backgrounds are  
1636 negligible.

<sub>1637</sub> **Chapter 8. Results**

<sub>1638</sub> **8.1 Statistical interpretation**

<sub>1639</sub> This section provides an overview of the statistical methods needed to interpret the  
<sub>1640</sub> collected and simulated data to estimate unknown physics parameters and determine com-  
<sub>1641</sub> patibility between data and the analysis hypothesis. For the BSM resonance search, the null  
<sub>1642</sub> hypothesis  $H_0$  assumes only SM background contributions and none from any new BSM  
<sub>1643</sub> resonance in the data.

<sub>1644</sub> **8.1.1 Profile likelihood fit**

<sub>1645</sub> Given a set of observed data points  $\mathbf{x} = [x_1, x_2, \dots]$  and unknown parameters  $\boldsymbol{\theta} =$   
<sub>1646</sub>  $[\theta_1, \theta_2, \dots, \theta_n]$ , the maximum likelihood method aims to find an estimate  $\hat{\boldsymbol{\theta}}$  that maximizes  
<sub>1647</sub> the joint probability function  $f(\mathbf{x}, \boldsymbol{\theta})$ , or in other words the set of parameters that gives the  
<sub>1648</sub> highest probability of observing the collected data points for a particular model. The func-  
<sub>1649</sub> tion to be maximized for this purpose is the log-likelihood (LLH) function  $\ln \mathcal{L}(\mathbf{x}, \boldsymbol{\theta})$  where  
<sub>1650</sub>  $\mathcal{L}(\mathbf{x}, \boldsymbol{\theta}) \equiv \prod_i f(x_i, \boldsymbol{\theta})$  is defined as the likelihood (LH) function. The LLH is maximized  
<sub>1651</sub> when  $\partial/\partial\theta_i (\ln \mathcal{L}) = 0$  for each parameter  $\theta_i$ .

<sub>1652</sub> For an usual binned physics analysis, the above variables for the LH function  $\mathcal{L}$  can  
<sub>1653</sub> be expressed as nuisance parameters (NP)  $\boldsymbol{\theta}$  and number of events for a model  $N_i(\mu)$  for  
<sub>1654</sub> the  $i^{\text{th}}$  bin, where  $\mu$  is the targeted parameter of interest (POI). In this analysis,  $N_i$  is  
<sub>1655</sub> assumed to follow a Poisson distribution and depends on the following quantities: the signal  
<sub>1656</sub> strength  $\mu$  defined as the ratio of observed to expected cross sections  $\sigma_{\text{obs}}/\sigma_{\text{exp}}$ ; nuisance  
<sub>1657</sub> parameters  $\boldsymbol{\theta}$  which represents the effects of systematic uncertainties, implemented in the

1658 LH function as Gaussian constraints; and normalization factors (NFs)  $\boldsymbol{\lambda}$  that control the  
 1659 normalization of background components that do not have a well-known cross section. The  
 1660 Poisson probability of observing exactly  $N_i$  events for an expected number of event  $n_i$  is

$$\mathcal{P}(N_i|n_i(\mu, \boldsymbol{\lambda})) = \frac{n_i^{N_i} e^{-n_i}}{N_i!}. \quad (8.1)$$

1661 The expected Poisson event number in a bin  $i$  can be parameterized as

$$n_i = \mu s_i(\boldsymbol{\theta}) + \sum_j \lambda_j b_{ij}(\boldsymbol{\theta}), \quad (8.2)$$

1662 where  $s_i$  is the number of signal events in bin  $i$  of every region, and  $b_{ij}$  is the number of  
 1663 events for a certain background source index  $j$  in bin  $i$ . The LH function in this analysis  
 1664 can be written as

$$\mathcal{L}(\mathbf{N}|\mu, \boldsymbol{\theta}, \boldsymbol{\lambda}) = \left( \prod_i \mathcal{P}(N_i|n_i) \right) \cdot \prod_k \mathcal{G}(\theta_k), \quad (8.3)$$

1665 where  $\mathcal{G}(\theta_k)$  is the Gaussian constraint for a NP  $k$ . The signal significance  $\mu$  and NFs  $\boldsymbol{\lambda}$  are  
 1666 left unconstrained and are fitted simultaneously in the profile LH fit. Define the profile LH  
 1667 ratio [162] as

$$\lambda(\mu) = \frac{\mathcal{L}(\mu, \hat{\boldsymbol{\theta}}_\mu, \hat{\boldsymbol{\lambda}}_\mu)}{\mathcal{L}(\hat{\mu}, \hat{\boldsymbol{\theta}}, \hat{\boldsymbol{\lambda}})}, \quad (8.4)$$

1668 where  $\hat{\mu}$ ,  $\hat{\boldsymbol{\theta}}$  and  $\hat{\boldsymbol{\lambda}}$  are parameter values that optimally maximizes the LH function, and  $\hat{\boldsymbol{\theta}}_\mu$ ,  
 1669  $\hat{\boldsymbol{\lambda}}_\mu$  are NP and NF values respectively that maximize the LH function for a given signal  
 1670 strength  $\mu$ . Using Neyman-Pearson lemma [163], the optimal test statistic for hypothesis  
 1671 testing is

$$q_\mu \equiv -2 \ln \lambda(\mu), \quad (8.5)$$

1672 where  $q_\mu = 0$  or  $\lambda(\mu) = 1$  corresponds to perfect agreement between the optimal parameter  
 1673  $\hat{\mu}$  obtained from data and the hypothesized value  $\mu$ . From Wilks' theorem [164], the test  
 1674 statistic  $q_\mu$  approaches a  $\chi^2$  distribution and can be evaluated as  $q_\mu = (\mu - \hat{\mu})^2 / \sigma_\mu^2$ .

1675 When evaluating against the background-only hypothesis ( $\mu = 0$ ), it can be assumed  
 1676 that the number of events observed under the signal hypothesis is higher than that of the  
 1677 background-only hypothesis, or  $\mu \geq 0$  according to Equation 8.2. This leads to a corre-  
 1678 sponding lower bound on the test statistic

$$q_0 = \begin{cases} -2 \ln \lambda(0), & \text{if } \hat{\mu} \geq 0, \\ 0, & \text{if } \hat{\mu} < 0. \end{cases} \quad (8.6)$$

### 1679 ***p*-value**

1680 To quantify the incompatibility between the observed data and the background-only hy-  
 1681 pothesis, the *p*-value is defined as  $p = P(q_\mu \geq q_{\mu, \text{obs}} | H_0)$  or in other words, the probability  
 1682 of observing data with a test statistic  $q_\mu$  under the null hypothesis  $H_0$  that is less compat-  
 1683 ible with  $H_0$  than the actual observed data with test statistic  $q_{\mu, \text{obs}}$ . The *p*-value can be  
 1684 expressed in terms of  $q_\mu$  as

$$p_\mu = \int_{q_{\mu, \text{obs}}}^{\infty} f(q_\mu | \mu) dq_\mu, \quad (8.7)$$

1685 where  $f(q_\mu | \mu) dq_\mu$  is the conditional probability density function of  $q_\mu$  given  $\mu$ .

1686 In some cases, it is more convenient to evaluate compatibility using the *Z*-value, defined  
 1687 as the number of standard deviations between the observed data and the mean in a Gaussian

1688 distribution. The  $p$ -value can be converted to  $Z$ -value via the relation

$$Z = \Phi^{-1}(1 - p), \quad (8.8)$$

1689 where  $\Phi$  is the quantile of the standard Gaussian. Rejecting the signal hypothesis usually  
1690 requires a 95% confidence level (CL) which corresponds to a  $p$ -value of 0.05 or a  $Z$ -value of  
1691 1.64, while rejecting the background-only hypothesis generally requires a  $Z$ -value of 5 or a  
1692  $p$ -value of  $2.84 \times 10^{-7}$ .

### 1693 8.1.2 Exclusion limit

1694 If the signal hypothesis is rejected, the exclusion upper limits can still be computed at  
1695 a certain CL (usually 95%) to establish the maximum value of  $\mu$  that is not excluded by  
1696 the observed data. The exclusion limits are calculated based on the  $\text{CL}_s$  method [165, 166]  
1697 under which the test statistic is defined as  $q_\mu = -2 \ln \frac{\mathcal{L}_{s+b}}{\mathcal{L}_b}$  with  $\mathcal{L}_{s+b}$  being the LH function  
1698 for the signal and background hypothesis ( $\mu > 0$ ) and  $\mathcal{L}_b$  being the LH function for the  
1699 background-only hypothesis ( $\mu = 0$ ). The  $p$ -value for both hypotheses can then be expressed  
1700 as

$$\begin{aligned} p_{s+b} &= P(q \geq q_{\text{obs}} | s + b) = \int_{q_{\text{obs}}}^{\infty} f(q | s + b) dq \\ p_b &= P(q \geq q_{\text{obs}} | b) = \int_{-\infty}^{q_{\text{obs}}} f(q | b) dq. \end{aligned} \quad (8.9)$$

1701 The signal hypothesis is excluded for a CL  $\alpha$  when the following condition is satisfied

$$\text{CL}_s \equiv \frac{p_{s+b}}{p_b} \geq 1 - \alpha. \quad (8.10)$$

1702 The value of  $\mu$  such that the signal hypothesis leads to  $\text{CL}_s = 1 - \alpha = 0.05$  is then the  
1703 exclusio upper limit at a 95% CL.

## 1704 8.2 Fit results

1705 The signal strength  $\mu$ , background NFs,  $t\bar{t}W$  scaling factors and uncertainty NPs are  
1706 simultaneously fitted using a binned profile LLH fit under the background-only hypothesis  
1707 to the  $H_T$  distribution in the SR and to corresponding distributions shown in Table 6.1 for  
1708 CRs.

1709 Before fitting to real data (unblinded fit), the fit was first performed in both the SR  
1710 and CRs using Asimov pseudo-datasets, in which the simulated data match exactly to MC  
1711 prediction with nominal  $\mu$  set to 0. This is done for the purpose of optimizing object selection  
1712 criteria and region definition, refining background estimation techniques and testing the  
1713 statistical interpretation model for signal extraction described in section 8.1. The fit is then  
1714 performed with Asimov data in the SR and real data in CRs to validate background modeling,  
1715 estimate sensitivity and assess the influence of statistical effects on fitted parameters. Finally,  
1716 the fully unblinded fit is performed with real data in all regions.

1717 The unblinded fit results are presented below. No significant excess over SM predictions  
1718 is observed, and the fitted signal strength  $\mu$  is compatible with zero for all  $Z'$  mass points.  
1719 Figure 8.1 shows the observed and expected upper limits at 95% confidence level on the  
1720 cross-section of  $pp \rightarrow t\bar{t}Z'$  production times the branching ratio of  $Z' \rightarrow t\bar{t}$  as a function of  
1721 the  $Z'$  resonance mass. The exclusion limits range from 7.9 fb to 9.44 fb depending on  $m_{Z'}$ .

1722 No significant variation is observed in fit output behavior using  $t\bar{t}Z'$  samples of different  
1723  $m_{Z'}$ ; results fitted using  $m_{Z'} = 2$  TeV are shown without substantial loss of generality.

1724 The background modeling is evaluated under the background-only hypothesis. The fitted  
1725 background NFs are shown in Table 8.1 and are consistent with their nominal values within  
1726 one standard deviation, or two standard deviations in the case of  $\text{NF}_{\text{HF } e}$  and  $\text{NF}_{t\bar{t}W+(4j)}$ .  
1727 Figure 8.2 shows good agreement between data and post-fit background distributions in  
1728 non-prompt background CRs and  $t\bar{t}W$  CRs.

1729 The pre-fit and post-fit background yields are shown in Table 8.2. Except for HF  $e$   
1730 background, post-fit yields for various backgrounds e.g.  $t\bar{t}t\bar{t}$ ,  $t\bar{t}H$ , other fake, etc. are  
1731 increased; the pre-fit to post-fit variations are consistent within  $\pm\sigma$ . Data and total post-fit  
1732 yields are also consistent within  $\pm\sigma$ . Post-fit yield for HF  $e$  background is lowered compared  
1733 to pre-fit yield within within  $2\sigma$  which can be related to the fitted value of  $\text{NF}_{\text{HF } e}$  in  
1734 Table 8.1; however, this difference in pre- and post-fit yields of HF  $e$  background has negligible  
1735 impact on the  $\mu$  as seen in Table 8.3.

1736 Table 8.3 outlines the impact on the signal strength  $\mu$  of various sources of uncertainty  
1737 grouped by their corresponding category. The background sources of uncertainty with the  
1738 largest impact is  $t\bar{t}t\bar{t}$  modeling, in particular  $t\bar{t}t\bar{t}$  generator choice and cross-section uncer-  
1739 tainties, followed by  $t\bar{t}W$  modeling due to their significant contributions in the SR observed  
1740 in Figure 6.1, especially in the more sensitive regions requiring three or more  $b$ -tagged jets.  
1741 The most significant impact on  $\mu$  within the set of instrumental uncertainties are uncertain-  
1742 ties on jet  $b$ -tagging attributable to the high jet and  $b$ -jet multiplicities in the BSM  $t\bar{t}t\bar{t}$  signal  
1743 signature.

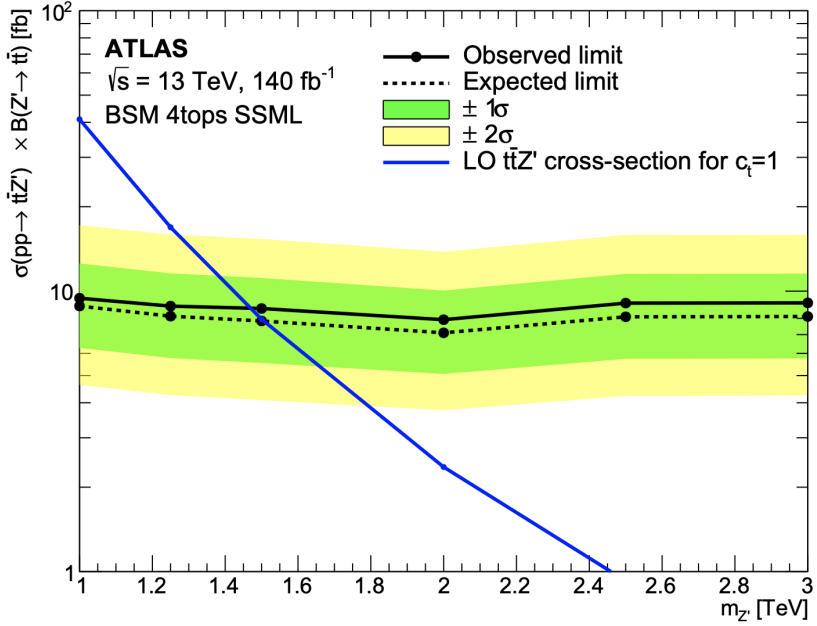


Figure 8.1: Observed (solid line) and expected (dotted line) upper limits as a function of the  $Z'$  mass at 95% CL on the cross-section of  $pp \rightarrow t\bar{t}Z'$  production times the  $Z' \rightarrow t\bar{t}$  branching ratio. The region above the observed limit is excluded. The solid blue line represents the theoretical signal cross-section with  $c_t = 1$  at LO in QCD [73]. The green and yellow bands represent the 68% ( $\pm\sigma$ ) and 95% ( $\pm 2\sigma$ ) confidence intervals respectively.

Table 8.1: Normalization factors for backgrounds with dedicated CRs, obtained from a simultaneous fit in all CRs and SR under the background-only hypothesis. The nominal pre-fit value is 1 for all NFs and 0 for the scaling factors  $a_0$  and  $a_1$ . Uncertainties shown include both statistical and systematic uncertainties.

Parameter	NF <sub>HF e</sub>	NF <sub>HF <math>\mu</math></sub>	NF <sub>Mat. Conv.</sub>	NF <sub>Low <math>m_{\gamma^*}</math></sub>	$a_0$	$a_1$	NF <sub><math>t\bar{t}W+(4j)</math></sub>	NF <sub><math>t\bar{t}W-(4j)</math></sub>
Fit value	$0.68^{+0.23}_{-0.22}$	$0.97^{+0.17}_{-0.16}$	$0.97^{+0.31}_{-0.28}$	$0.97^{+0.23}_{-0.20}$	$0.39^{+0.11}_{-0.11}$	$0.42^{+0.25}_{-0.24}$	$1.21^{+0.18}_{-0.18}$	$1.10^{+0.26}_{-0.26}$

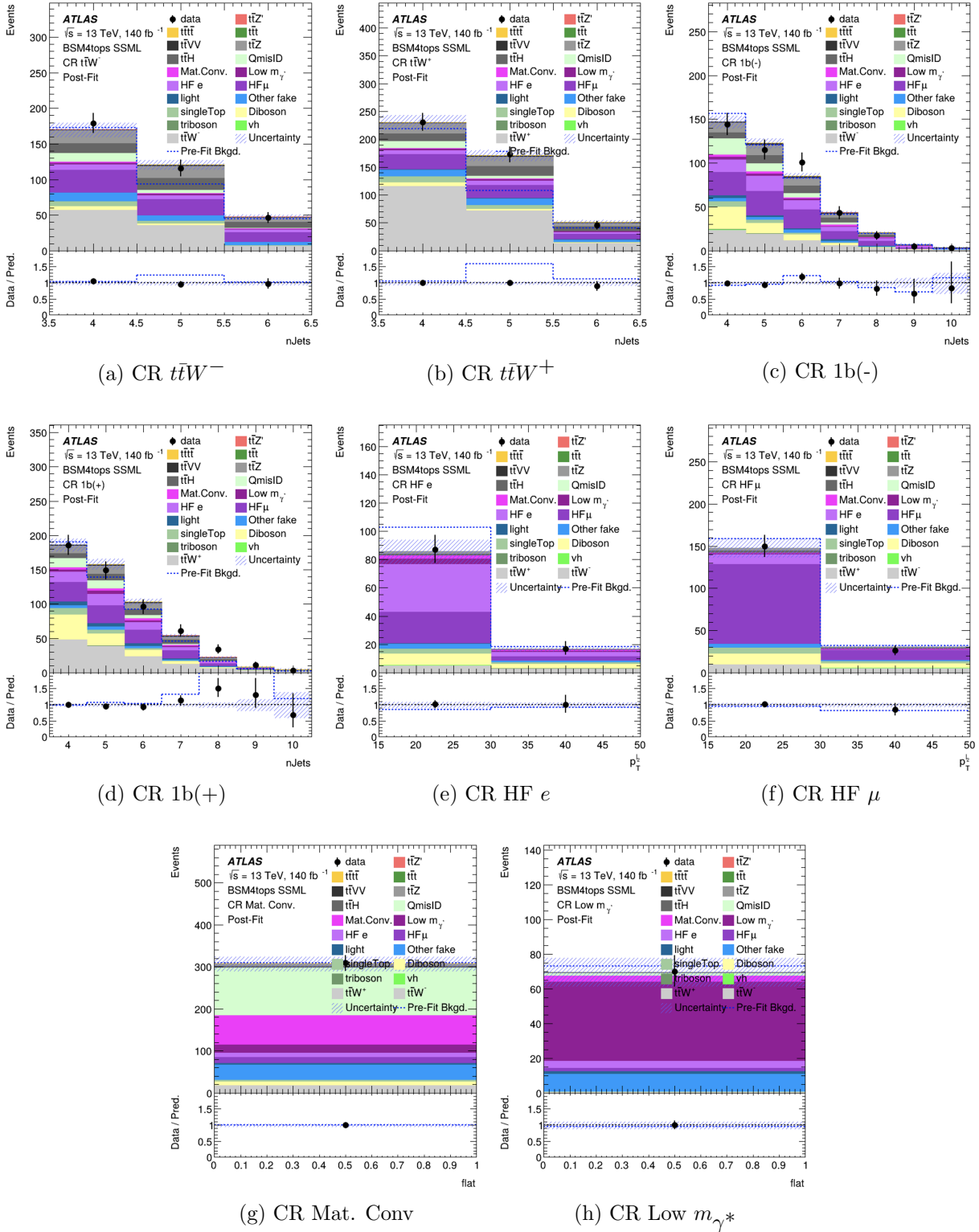


Figure 8.2: Comparison between data and post-fit prediction for the discriminant observable in each non-prompt and  $t\bar{W}$  background CR. The lower panel shows the ratio between data and post-fit predictions. The shaded band represents the total uncertainty on the fit. The dashed line represents the pre-fit distribution.

Table 8.2: Pre-fit and post-fit background yields in the inclusive SR. The number of data events and pre-fit estimate signal yields are also shown. Background yields shown are obtained from the fit using the  $t\bar{t}Z'$  signal sample with  $m_{Z'} = 2$  TeV. Pre-fit yields for  $t\bar{t}W$  background are set to 0 nominally prior to data-driven normalization. Total yield uncertainty differs from the quadrature sum of constituent uncertainties due to correlation and anticorrelation effects.

Process	Pre-fit	Post-fit
<b>Background</b>		
$t\bar{t}t\bar{t}$	$42.35 \pm 5.45$	$46.91 \pm 5.19$
$t\bar{t}W^+$	-	$103.93 \pm 15.91$
$t\bar{t}W^-$	-	$55.27 \pm 11.14$
$t\bar{t}Z$	$78.02 \pm 14.12$	$75.57 \pm 11.13$
$t\bar{t}H$	$81.00 \pm 7.10$	$82.90 \pm 7.30$
$t\bar{t}t$	$3.33 \pm 0.59$	$3.37 \pm 0.60$
Single-top ( $tq$ , $tZq$ , $tWZ$ , etc.)	$13.38 \pm 2.87$	$12.69 \pm 2.86$
$t\bar{t}VV/t\bar{t}VH/t\bar{t}HH$	$17.07 \pm 4.66$	$16.44 \pm 4.64$
Charge misidentification	$40.31 \pm 0.32$	$40.33 \pm 0.32$
$VV/VVV/VH$	$10.01 \pm 4.76$	$6.69 \pm 2.75$
Mat. Conv.	$26.20 \pm 0.91$	$25.76 \pm 6.06$
Low $m_{\gamma^*}$	$26.14 \pm 0.66$	$25.62 \pm 4.23$
HF $e$	$21.99 \pm 1.45$	$15.42 \pm 3.70$
HF $\mu$	$31.33 \pm 3.47$	$31.53 \pm 5.06$
Light-flavor decays	$13.47 \pm 0.53$	$13.54 \pm 0.53$
Other fake & non-prompt	$24.90 \pm 2.26$	$26.00 \pm 1.96$
Total background	-	$576.53 \pm 19.86$
<b>Signal <math>t\bar{t}Z' \rightarrow t\bar{t}t\bar{t}</math></b>		
$m_{Z'} = 1$ TeV	$52.83 \pm 1.41$	-
$m_{Z'} = 1.25$ TeV	$52.94 \pm 1.35$	-
$m_{Z'} = 1.5$ TeV	$53.07 \pm 1.47$	-
$m_{Z'} = 2$ TeV	$52.49 \pm 1.43$	-
$m_{Z'} = 2.5$ TeV	$53.07 \pm 1.47$	-
$m_{Z'} = 3$ TeV	$52.45 \pm 1.50$	-
<b>Data</b>	604	

Table 8.3: Post-fit impact of uncertainty sources on the signal strength  $\mu$ , grouped by categories. Values shown are obtained from the fit using the  $t\bar{t}Z'$  signal sample with  $m_{Z'} = 2$  TeV. Impact on  $\mu$  is evaluated for each uncertainty category by re-fitting with the corresponding set of NPs fixed to their best-fit values. Total uncertainty differs from the quadrature sum of constituent uncertainties due to correlation between NPs in the fit.

Uncertainty source	$\Delta\mu$	
<b>Signal modeling</b>		
$t\bar{t}Z'$	+0.00	-0.00
<b>Background modeling</b>		
$t\bar{t}\bar{t}$	+0.15	-0.13
$t\bar{t}W$	+0.04	-0.03
$t\bar{t}Z$	+0.02	-0.02
$t\bar{t}H$	+0.02	-0.02
Non-prompt leptons	+0.00	-0.00
Other backgrounds	+0.02	-0.02
<b>Instrumental</b>		
Luminosity	+0.00	-0.00
Jet uncertainties	+0.04	-0.04
Jet flavor tagging ( $b$ -jets)	+0.04	-0.04
Jet flavor tagging ( $c$ -jets)	+0.01	-0.01
Jet flavor tagging (light-jets)	+0.02	-0.01
MC simulation sample size	+0.01	-0.01
Other experimental uncertainties	+0.01	-0.01
Total systematic uncertainty	+0.15	-0.17
<b>Statistical</b>		
$t\bar{t}W$ NFs and scaling factors	+0.01	-0.01
Non-prompt lepton NFs (HF, Mat. Conv., Low $m_{\gamma^*}$ )	+0.00	-0.00
Total statistical uncertainty	+0.25	-0.23
<b>Total uncertainty</b>	+0.29	-0.29

# 1744 Chapter 9. Summary

1745 This dissertation presents a search for BSM top-philic heavy vector resonance based on a  
1746 simplified top-philic color singlet  $Z'(\rightarrow t\bar{t})$  model in the top-quark pair associated production  
1747 channel ( $t\bar{t}Z'$ ). The search is performed in the same-sign dilepton and multilepton channel  
1748 of the  $t\bar{t}t\bar{t}$  final states, using the full Run 2 data set collected between 2015 and 2018 by the  
1749 ATLAS detector at the LHC, corresponding to an integrated luminosity of  $140 \text{ fb}^{-1}$  of  $pp$   
1750 collisions at center-of-mass energy  $\sqrt{s} = 13 \text{ TeV}$ .

1751 New data-driven estimation methods for  $t\bar{t}W$  and charge misidentification background  
1752 are employed to improve background modeling and signal sensitivity compared to previous  
1753 analysis [28]. No significant excess over Standard Model predictions is observed. Observed  
1754 exclusion limits at 95% confidence level as a function of the  $Z'$  mass are set on the production  
1755 cross section of  $pp \rightarrow t\bar{t}Z'$  times the  $Z' \rightarrow t\bar{t}$  branching ratio, ranging from 7.9 fb to 9.4 fb  
1756 depending on the  $Z'$  mass. The analysis probes a  $Z'$  mass range from 1 TeV to 3 TeV under  
1757 the assumption of a top- $Z'$  coupling strength of  $c_t = 1$  and chirality angle  $\theta = \pi/4$ .

1758 Further improvements in analysis strategies, including multivariate techniques for signal  
1759 discrimination, are expected to increase discovery potential in future searches. Looking  
1760 forward, the upcoming Run 3 data with increased luminosity at  $\sqrt{s} = 13.6 \text{ TeV}$  along  
1761 with prospects of the High-Luminosity LHC will significantly enhance sensitivity to BSM  
1762 physics and offer more opportunities to explore top-philic resonances and other exciting new  
1763 phenomena.

# References

- 1764 [1] J. Schwinger. *On Quantum-Electrodynamics and the Magnetic Moment of the Elec-*  
tron. *Phys. Rev.* **73** (4 1948), pp. 416–417 (cit. on p. 1).
- 1766 [2] R. P. Feynman. *Space-Time Approach to Quantum Electrodynamics.* *Phys. Rev.* **76**  
(6 1949), pp. 769–789 (cit. on p. 1).
- 1769 [3] S. Tomonaga. *On a relativistically invariant formulation of the quantum theory of*  
wave fields. *Prog. Theor. Phys.* **1** (1946), pp. 27–42 (cit. on p. 1).
- 1771 [4] E. Fermi. *An attempt of a theory of beta radiation. I.* *Nuclear Physics B* **4** (1967).  
Translated from the original 1934 German article by C. P. Enz and C. H. Beck, pp. 1–  
1773 27 (cit. on p. 1).
- 1774 [5] D. J. Griffiths. *Introduction to Elementary Particles.* 2nd. Weinheim: Wiley-VCH,  
1775 2008. ISBN: 978-3-527-40601-2 (cit. on p. 1).
- 1776 [6] C. Yang and R. Mills. *Conservation of Isotopic Spin and Isotopic Gauge Invariance.*  
1777 *Phys. Rev.* **96** (1 1954), pp. 191–195 (cit. on pp. 1, 10).
- 1778 [7] A. Milsted and T. J. Osborne. *Quantum Yang-Mills theory: An overview of a program.*  
1779 *Phys. Rev. D* **98** (1 2018), p. 014505 (cit. on pp. 1, 10).

- 1780 [8] S. L. Glashow. *Partial-symmetries of weak interactions*. Nuclear Physics 22.4 (1961),  
1781 pp. 579–588. ISSN: 0029-5582 (cit. on p. 1).
- 1782 [9] D. J. Gross and F. Wilczek. *Ultraviolet Behavior of Non-Abelian Gauge Theories*.  
1783 Phys. Rev. Lett. 30 (26 1973), pp. 1343–1346 (cit. on p. 1).
- 1784 [10] H. D. Politzer. *Reliable Perturbative Results for Strong Interactions?* Phys. Rev. Lett.  
1785 30 (26 1973), pp. 1346–1349 (cit. on p. 1).
- 1786 [11] P. Higgs. *Broken symmetries and the masses of gauge bosons*. Phys. Rev. Lett. 13 (16  
1787 1964), pp. 508–509 (cit. on pp. 1, 14).
- 1788 [12] P. Higgs. *Broken symmetries, massless particles and gauge fields*. Physics Letters 12.2  
1789 (1964), pp. 132–133. ISSN: 0031-9163 (cit. on pp. 1, 14).
- 1790 [13] F. Englert and R. Brout. *Broken Symmetry and the Mass of Gauge Vector Mesons*.  
1791 Phys. Rev. Lett. 13 (9 1964), pp. 321–323 (cit. on pp. 1, 14).
- 1792 [14] S. Weinberg. *The making of the Standard Model*. The European Physical Journal C  
1793 34.1 (May 2004), 513. ISSN: 1434-6052. arXiv: hep-ph/0401010 [hep-ph] (cit. on  
1794 p. 2).
- 1795 [15] D. P. Barber et al. *Discovery of Three-Jet Events and a Test of Quantum Chromody-  
1796 namics at PETRA*. Phys. Rev. Lett. 43 (12 1979), pp. 830–833 (cit. on p. 2).
- 1797 [16] G. Arnison et al. *Experimental Observation of Isolated Large Transverse Energy Elec-  
1798 trons with Associated Missing Energy at  $\sqrt{s} = 540 \text{ GeV}$* . Phys. Lett. B 122 (1983),  
1799 pp. 103–116 (cit. on p. 2).

- 1800 [17] G. Arnison and others. *Experimental Observation of Lepton Pairs of Invariant Mass*  
1801 *Around  $95 \text{ GeV}/c^2$  at the CERN SPS Collider.* *Phys. Lett. B* **126** (1983), pp. 398–410  
1802 (cit. on p. 2).
- 1803 [18] CDF Collaboration. *Observation of Top Quark Production in  $\bar{p}p$  Collisions with the*  
1804 *Collider Detector at Fermilab.* *Phys. Rev. Lett.* **74** (14 1995), pp. 2626–2631 (cit. on  
1805 p. 2).
- 1806 [19] DØ Collaboration. *Observation of the Top Quark.* *Phys. Rev. Lett.* **74** (14 1995),  
1807 pp. 2632–2637 (cit. on p. 2).
- 1808 [20] ATLAS Collaboration. *Observation of a new particle in the search for the Standard*  
1809 *Model Higgs boson with the ATLAS detector at the LHC.* *Phys. Lett. B* **716** (2012),  
1810 p. 1. arXiv: 1207.7214 [[hep-ex](#)] (cit. on pp. 2, 14).
- 1811 [21] CMS Collaboration. *Observation of a new boson at a mass of 125 GeV with the CMS*  
1812 *experiment at the LHC.* *Phys. Lett. B* **716** (2012), p. 30. arXiv: 1207.7235 [[hep-ex](#)]  
1813 (cit. on pp. 2, 14).
- 1814 [22] S. Navas et al. *Review of particle physics.* *Phys. Rev. D* **110.3** (2024), p. 030001 (cit.  
1815 on pp. 2, 7, 8).
- 1816 [23] Y. Fukuda et al. *Evidence for Oscillation of Atmospheric Neutrinos.* *Phys. Rev. Lett.*  
1817 **81** (8 1998), pp. 1562–1567 (cit. on p. 2).
- 1818 [24] M. Cristinziani and M. Mulders. *Top-quark physics at the Large Hadron Collider.*  
1819 *Journal of Physics G: Nuclear and Particle Physics* **44.6** (2017), p. 063001. arXiv:  
1820 1606.00327 [[hep-ex](#)] (cit. on pp. 2, 8).

- 1821 [25] ATLAS and CMS Collaborations. *Combination of inclusive top-quark pair production*  
1822 *cross-section measurements using ATLAS and CMS data at  $\sqrt{s} = 7$  and 8 TeV.* *JHEP*  
1823 **07** (2023), p. 213. arXiv: [2205.13830 \[hep-ex\]](#) (cit. on p. 3).
- 1824 [26] C. Degrande, J.-M. Grard, C. Grojean, F. Maltoni, and G. Servant. *Non-resonant new*  
1825 *physics in top pair production at hadron colliders.* *Journal of High Energy Physics*  
1826 **2011.3** (Mar. 2011). ISSN: 1029-8479. arXiv: [1010.6304 \[hep-ph\]](#) (cit. on p. 3).
- 1827 [27] ATLAS Collaboration. *The ATLAS Experiment at the CERN Large Hadron Collider.*  
1828 *JINST* **3** (2008), S08003 (cit. on pp. 3, 22, 25, 26, 28–32).
- 1829 [28] ATLAS Collaboration. *Search for top-philic heavy resonances in pp collisions at  $\sqrt{s} =$*   
1830 *13 TeV with the ATLAS detector.* *Eur. Phys. J. C* **84** (2024), p. 157. arXiv: [2304.01678 \[hep-ex\]](#) (cit. on pp. 3, 4, 18, 92).
- 1832 [29] H. P. Nilles. *Supersymmetry, Supergravity and Particle Physics.* *Phys. Rept.* **110**  
1833 (1984), pp. 1–162 (cit. on p. 3).
- 1834 [30] G. R. Farrar and P. Fayet. *Phenomenology of the Production, Decay, and Detection*  
1835 *of New Hadronic States Associated with Supersymmetry.* *Phys. Lett. B* **76** (1978),  
1836 pp. 575–579 (cit. on p. 3).
- 1837 [31] T. Plehn and T. M. P. Tait. *Seeking sgluons.* *Journal of Physics G: Nuclear and*  
1838 *Particle Physics* **36.7** (2009), p. 075001. arXiv: [0810.3919 \[hep-ph\]](#) (cit. on p. 3).
- 1839 [32] S. Calvet, B. Fuks, P. Gris, and L. Valry. *Searching for sgluons in multitop events*  
1840 *at a center-of-mass energy of 8 TeV.* *Journal of High Energy Physics* **2013.4** (Apr.  
1841 2013). ISSN: 1029-8479. arXiv: [1212.3360 \[hep-ph\]](#) (cit. on p. 3).

- 1842 [33] A. Pomarol and J. Serra. *Top quark compositeness: Feasibility and implications*. Phys-  
1843       ical Review D 78.7 (Oct. 2008). ISSN: 1550-2368. arXiv: 0806.3247 [hep-ph] (cit. on  
1844       p. 3).
- 1845 [34] K. Kumar, T. M. Tait, and R. Vega-Morales. *Manifestations of top compositeness at*  
1846       *colliders*. Journal of High Energy Physics 2009.05 (May 2009), 022022. ISSN: 1029-  
1847       8479. arXiv: 0901.3808 [hep-ph] (cit. on p. 3).
- 1848 [35] G. Banelli, E. Salvioni, J. Serra, T. Theil, and A. Weiler. *The present and future of*  
1849       *four top operators*. Journal of High Energy Physics 2021.2 (Feb. 2021). ISSN: 1029-  
1850       8479. arXiv: 2010.05915 [hep-ph] (cit. on p. 3).
- 1851 [36] R. Aoude, H. El Faham, F. Maltoni, and E. Vryonidou. *Complete SMEFT predictions*  
1852       *for four top quark production at hadron colliders*. Journal of High Energy Physics  
1853       2022.10 (Oct. 2022). ISSN: 1029-8479. arXiv: 2208.04962 [hep-ph] (cit. on p. 3).
- 1854 [37] C. Zhang. *Constraining qqtt operators from four-top production: a case for enhanced*  
1855       *EFT sensitivity*. Chinese Physics C 42.2 (Feb. 2018), p. 023104. ISSN: 1674-1137.  
1856       arXiv: 1708.05928 [hep-ph] (cit. on p. 3).
- 1857 [38] L. Darmé, B. Fuks, and F. Maltoni. *Topophilic heavy resonances in four-top final*  
1858       *states and their EFT interpretation*. Journal of High Energy Physics 2021.9 (Sept.  
1859       2021). ISSN: 1029-8479. arXiv: 2104.09512 [hep-ph] (cit. on pp. 3, 17).
- 1860 [39] N. Craig, F. D'Eramo, P. Draper, S. Thomas, and H. Zhang. *The Hunt for the Rest*  
1861       *of the Higgs Bosons*. JHEP 06 (2015), p. 137. arXiv: 1504.04630 [hep-ph] (cit. on  
1862       pp. 3, 17).

- 1863 [40] N. Craig, J. Hajer, Y.-Y. Li, T. Liu, and H. Zhang. *Heavy Higgs bosons at low  $\tan \beta$ :  
1864 from the LHC to 100 TeV*. *Journal of High Energy Physics* 2017.1 (Jan. 2017). ISSN:  
1865 1029-8479. arXiv: [1605.08744 \[hep-ph\]](#) (cit. on pp. 3, 17).
- 1866 [41] G. C. Branco et al. *Theory and phenomenology of two-Higgs-doublet models*. *Phys.  
1867 Rept.* 516 (2012), pp. 1–102. arXiv: [1106.0034 \[hep-ph\]](#) (cit. on pp. 3, 17).
- 1868 [42] S. Gori, I.-W. Kim, N. R. Shah, and K. M. Zurek. *Closing the wedge: Search strategies  
1869 for extended Higgs sectors with heavy flavor final states*. *Phys. Rev. D* 93 (7 2016),  
1870 p. [075038](#) (cit. on pp. 3, 17).
- 1871 [43] P. S. B. Dev and A. Pilaftsis. *Maximally symmetric two Higgs doublet model with  
1872 natural Standard Model alignment*. *Journal of High Energy Physics* 2014.12 (Dec.  
1873 2014), p. 024. arXiv: [1408.3405 \[hep-ph\]](#) (cit. on pp. 3, 17).
- 1874 [44] ATLAS Collaboration. *Observation of four-top-quark production in the multilepton  
1875 final state with the ATLAS detector*. *Eur. Phys. J. C* 83 (2023), p. 496. arXiv: [2303.  
1876 15061 \[hep-ex\]](#) (cit. on pp. 3, 4, 18, 51, 64, 71, 80).
- 1877 [45] N. Greiner, K. Kong, J.-C. Park, S. C. Park, and J.-C. Winter. *Model-independent  
1878 production of a topophilic resonance at the LHC*. *Journal of High Energy Physics*  
1879 2015.4 (2015), p. 29. ISSN: 1029-8479. arXiv: [1410.6099 \[hep-ph\]](#) (cit. on pp. ix, 3,  
1880 18–20).
- 1881 [46] ATLAS Collaboration. *Evidence for  $t\bar{t}t\bar{t}$  production in the multilepton final state in  
1882 proton–proton collisions at  $\sqrt{s} = 13\text{TeV}$  with the ATLAS detector*. *Eur. Phys. J. C*  
1883 80 (2020), p. 1085. arXiv: [2007.14858 \[hep-ex\]](#) (cit. on pp. 4, 71).
- 1884 [47] D. H. Perkins. *Introduction to High Energy Physics*. 4th. Cambridge, UK: Cambridge  
1885 University Press, Apr. 2000. ISBN: 9780521621960 (cit. on p. 5).

- 1886 [48] C. Burgard and D. Galbraith. *Standard Model of Physics*. URL: <https://texample.net/model-physics/> (visited on 06/02/2025) (cit. on p. 6).
- 1887
- 1888 [49] H. Georgi. *Lie Algebras in Particle Physics: from Isospin to Unified Theories*. 2nd.
- 1889 CRC Press, 2000. ISBN: 9780429499210 (cit. on pp. 7, 10).
- 1890 [50] ATLAS and CMS Collaborations. *Combination of Measurements of the Top Quark*
- 1891 *Mass from Data Collected by the ATLAS and CMS Experiments at  $\sqrt{s} = 7$  and 8 TeV*.
- 1892 *Phys. Rev. Lett.* **132** (2023), p. 261902. arXiv: [2402.08713 \[hep-ex\]](https://arxiv.org/abs/2402.08713) (cit. on p. 8).
- 1893 [51] H. de la Torre and T. Farooque. *Looking beyond the Standard Model with Third Gen-*
- 1894 *eration Quarks at the LHC*. *Symmetry* **14**.3 (2022), p. 444 (cit. on p. 8).
- 1895 [52] Q.-H. Cao, J.-N. Fu, Y. Liu, X.-H. Wang, and R. Zhang. *Probing Top-philic New*
- 1896 *Physics via Four-Top-Quark Production*. *Chinese Physics C* **45**.9 (2021), p. 093107.
- 1897 arXiv: [2105.03372 \[hep-ph\]](https://arxiv.org/abs/2105.03372) (cit. on p. 8).
- 1898 [53] H. Beauchesne et al. *A case study about BSM vector resonances with direct couplings*
- 1899 *to the third quark generation*. *European Physical Journal C* **80**.5 (2020), p. 485. arXiv:
- 1900 [1908.11619 \[hep-ph\]](https://arxiv.org/abs/1908.11619) (cit. on p. 8).
- 1901 [54] F. Maltoni, D. Pagani, and S. Tentori. *Top-quark pair production as a probe of light*
- 1902 *top-philic scalars and anomalous Higgs interactions*. *Journal of High Energy Physics*
- 1903 **2024**.9 (Sept. 2024), p. 098. arXiv: [2406.06694 \[hep-ph\]](https://arxiv.org/abs/2406.06694) (cit. on p. 8).
- 1904 [55] CMS Collaboration. *Search for  $t\bar{t}H$  production in the  $H \rightarrow b\bar{b}$  decay channel with*
- 1905 *leptonic  $t\bar{t}$  decays in proton–proton collisions at  $\sqrt{s} = 13$  TeV*. *JHEP* **03** (2019),
- 1906 p. 026. arXiv: [1804.03682 \[hep-ex\]](https://arxiv.org/abs/1804.03682) (cit. on p. 8).

- 1907 [56] Y. Grossman and Y. Nir. *The Standard Model: From Fundamental Symmetries to Ex-*  
1908 *perimental Tests*. See Chapter 8.2. Cambridge University Press, 2023. ISBN: 9781009320378  
1909 (cit. on p. 9).
- 1910 [57] M. E. Peskin and D. V. Schroeder. *An Introduction to Quantum Field Theory*. 1st.  
1911 Reading, MA, USA: AddisonWesley, 1995. ISBN: 978-0-201-50397-5 (cit. on p. 9).
- 1912 [58] D. J. Gross. *The role of symmetry in fundamental physics*. Proceedings of the National  
1913 Academy of Sciences of the United States of America 93.25 (Dec. 1996), pp. 14256–  
1914 14259 (cit. on p. 9).
- 1915 [59] M. Bañados and I. Reyes. *A short review on Noethers theorems, gauge symmetries*  
1916 *and boundary terms*. International Journal of Modern Physics D 25.10 (Aug. 2016),  
1917 p. 1630021. ISSN: 1793-6594. arXiv: 1601.03616 [hep-th] (cit. on p. 9).
- 1918 [60] A. Pich. *The Standard Model of electroweak interactions. 2004 European School of*  
1919 *High-Energy Physics*. Feb. 2005, pp. 1–48. arXiv: hep-ph/0502010 [hep-ex] (cit. on  
1920 pp. 11–13).
- 1921 [61] P. Dev and A. Pilaftsis. *High-temperature electroweak symmetry non-restoration from*  
1922 *new fermions and implications for baryogenesis*. Journal of High Energy Physics  
1923 2020.9 (Sept. 2020), p. 012. arXiv: 2002.05174 [hep-ph] (cit. on p. 13).
- 1924 [62] J. Riebesell. *Higgs Potential*. URL: <https://tikz.net/higgs-potential/> (visited on  
1925 07/07/2025) (cit. on p. 15).
- 1926 [63] J. Goldstone, A. Salam, and S. Weinberg. *Broken Symmetries*. Phys. Rev. 127 (3  
1927 1962), pp. 965–970 (cit. on p. 15).
- 1928 [64] J. Ellis. *Higgs Physics. 2013 European School of High-Energy Physics*. 2015, pp. 117–  
1929 168. arXiv: 1312.5672 [hep-ph] (cit. on pp. 15, 16).

- 1930 [65] G. Ferretti and D. Karateev. *Fermionic UV completions of composite Higgs models*.  
1931 Journal of High Energy Physics 2014.3 (Mar. 2014). ISSN: 1029-8479 (cit. on p. 17).
- 1932 [66] L. Vecchi. *A dangerous irrelevant UV-completion of the composite Higgs*. JHEP 02  
1933 (2017), p. 094. arXiv: 1506.00623 [hep-ph] (cit. on p. 17).
- 1934 [67] CDF Collaboration. *Search for New Physics in High-Mass Electron-Positron Events*  
1935 *in  $p\bar{p}$  Collisions at  $\sqrt{s} = 1.96$  TeV*. Phys. Rev. Lett. 99 (17 2007), p. 171802. arXiv:  
1936 0707.2524 [hep-ex] (cit. on p. 17).
- 1937 [68] M. Battaglia and G. Servant. *Four-top production and  $t\bar{t}$ +missing energy events at*  
1938 *multi TeV  $e^+e^-$  colliders*. Nuovo Cim. C 033N2 (2010), pp. 203–208. arXiv: 1005.4632  
1939 [hep-ex] (cit. on p. 17).
- 1940 [69] N. Arkani-Hamed, A. G. Cohen, and H. Georgi. *Electroweak symmetry breaking from*  
1941 *dimensional deconstruction*. Physics Letters B 513.1-2 (July 2001), pp. 232–240. arXiv:  
1942 hep-ph/0105239 [hep-ph] (cit. on p. 17).
- 1943 [70] T. Han, H. E. Logan, B. McElrath, and L.-T. Wang. *Phenomenology of the little Higgs*  
1944 *model*. Phys. Rev. D 67 (9 2003), p. 095004. arXiv: hep-ph/0301040 [hep-ph] (cit. on  
1945 p. 17).
- 1946 [71] P. Langacker and M. Plümacher. *Flavor changing effects in theories with a heavy  $Z'$*   
1947 *boson with family nonuniversal couplings*. Phys. Rev. D 62 (1 2000), p. 013006. arXiv:  
1948 hep-ph/0001204 [hep-ph] (cit. on p. 17).
- 1949 [72] P. Langacker. *The Physics of Heavy  $Z'$  Gauge Bosons*. Rev. Mod. Phys. 81 (2009),  
1950 pp. 1199–1228. arXiv: 0801.1345 [hep-ph] (cit. on p. 17).

- 1951 [73] J. H. Kim, K. Kong, S. J. Lee, and G. Mohlabeng. *Probing TeV scale top-philic*  
1952 *resonances with boosted top-tagging at the high luminosity LHC*. *Phys. Rev. D* **94** (3  
1953 2016), p. 035023. arXiv: [1604.07421 \[hep-ph\]](#) (cit. on pp. ix, 17, 18, 20, 88).
- 1954 [74] P. J. Fox, I. Low, and Y. Zhang. *Top-philic Z' forces at the LHC*. *Journal of High*  
1955 *Energy Physics* **2018.3** (Mar. 2018). ISSN: 1029-8479. arXiv: [1801.03505 \[hep-ph\]](#)  
1956 (cit. on p. 17).
- 1957 [75] CMS Collaboration. *Observation of four top quark production in proton-proton col-*  
1958 *lisions at  $\sqrt{s} = 13\text{TeV}$* . *Physics Letters B* **847** (2023), p. 138290. arXiv: [2305.13439](#)  
1959 [\[hep-ex\]](#) (cit. on p. 18).
- 1960 [76] G. Brooijmans et al. *New Physics at the LHC. A Les Houches Report: Physics at*  
1961 *TeV Colliders 2009 - New Physics Working Group. 6th Les Houches Workshop on*  
1962 *Physics at TeV Colliders*. See Chapter 12. May 2010, pp. 191–380. arXiv: [1005.1229](#)  
1963 [\[hep-ph\]](#) (cit. on pp. ix, 20).
- 1964 [77] P. Sabatini. *Evidence for four-top-quarks production with the ATLAS detector at the*  
1965 *Large Hadron Collider*. Tech. rep. Geneva: CERN, 2021. URL: <https://cds.cern.ch/record/2784150> (cit. on p. 21).
- 1967 [78] L. Evans and P. Bryant. *LHC Machine*. *JINST* **3** (2008), S08001 (cit. on p. 22).
- 1968 [79] CMS Collaboration. *The CMS Experiment at the CERN LHC*. *JINST* **3** (2008),  
1969 S08004 (cit. on p. 22).
- 1970 [80] The ALICE Collaboration. *The ALICE experiment at the CERN LHC*. *JINST* **3**  
1971 (2008), S08002 (cit. on p. 22).
- 1972 [81] The LHCb Collaboration. *The LHCb Detector at the LHC*. *JINST* **3** (2008), S08005  
1973 (cit. on p. 22).

- 1974 [82] E. e. a. Gschwendtner. *AWAKE, The Advanced Proton Driven Plasma Wakefield*  
1975 *Acceleration Experiment at CERN*. Nuclear Instruments and Methods in Physics Re-  
1976 search Section A 829 (2016), pp. 76–82. arXiv: 1512.05498 [physics.acc-ph] (cit. on  
1977 p. 23).
- 1978 [83] J. L. Feng, I. Galon, F. Kling, and S. Trojanowski. *ForwArd Search ExpeRiment at*  
1979 *the LHC*. Phys. Rev. D 97 (3 2018), p. 035001. arXiv: 1708.09389 [hep-ph] (cit. on  
1980 p. 23).
- 1981 [84] The KATRIN collaboration. *The design, construction, and commissioning of the KA-*  
1982 *TRIN experiment*. Journal of Instrumentation 16.08 (2021), T08015. arXiv: 2103.  
1983 04755 [physics.ins-det] (cit. on p. 23).
- 1984 [85] E. Lopienska. *The CERN accelerator complex, layout in 2022*. General Photo. 2022.  
1985 URL: <https://cds.cern.ch/record/2800984> (visited on 07/08/2025) (cit. on p. 23).
- 1986 [86] High Luminosity LHC Project Organization. *The HL-LHC project*. 2025. URL: <https://hilumilhc.web.cern.ch/content/hl-lhc-project> (visited on 06/11/2025) (cit. on  
1987 p. 24).
- 1988 [87] ATLAS Collaboration. *Performance of the ATLAS detector using first collision data*.  
1989 JHEP 09 (2010), p. 056. arXiv: 1005.5254 [hep-ex] (cit. on p. 24).
- 1990 [88] ATLAS Collaboration. *Luminosity determination in  $pp$  collisions at  $\sqrt{s} = 13 \text{ TeV}$*   
1991 *using the ATLAS detector at the LHC*. Eur. Phys. J. C 83 (2023), p. 982. arXiv:  
1992 2212.09379 [hep-ex] (cit. on pp. 25, 51, 74).
- 1993 [89] J. M. Butterworth, G. Dissertori, and G. P. Salam. *Hard Processes in Proton-Proton*  
1994 *Collisions at the Large Hadron Collider*. Annu. Rev. Nucl. Part. Sci. 62 (2012),  
1995 pp. 387–405. arXiv: 1202.0583 [hep-ex] (cit. on p. 25).

- 1997 [90] J. Campbell, J. Huston, and W. J. Stirling. *Hard interactions of quarks and gluons: a primer for LHC physics*. Reports on Progress in Physics 70.1 (2006), p. 89. arXiv: 1998 hep-ph/0611148 [hep-ex] (cit. on p. 25).
- 1999 [91] ATLAS Collaboration. *Standard Model Summary Plots October 2023*. ATL-PHYS- 2000 PUB-2023-039. 2023. URL: <https://cds.cern.ch/record/2882448> (cit. on p. 26).
- 2001 [92] J. Pequenao and P. Schaffner. *How ATLAS detects particles: diagram of particle 2002 paths in the detector*. 2013. URL: <https://cds.cern.ch/record/1505342> (visited on 2003 07/08/2025) (cit. on p. 27).
- 2004 [93] J. Pequenao. *Computer generated image of the ATLAS inner detector*. 2008. URL: 2005 <https://cds.cern.ch/record/1095926> (visited on 07/08/2025) (cit. on p. 28).
- 2006 [94] J. Pequenao. *Computer Generated image of the ATLAS calorimeter*. 2008. URL: 2007 <https://cds.cern.ch/record/1095927> (visited on 07/08/2025) (cit. on p. 30).
- 2008 [95] ATLAS Collaboration. *Operation of the ATLAS trigger system in Run 2*. JINST 15 2009 (2020), P10004. arXiv: 2007.12539 [physics.ins-det] (cit. on p. 33).
- 2010 [96] ATLAS Collaboration. *Performance of the ATLAS track reconstruction algorithms 2011 in dense environments in LHC Run 2*. Eur. Phys. J. C 77 (2017), p. 673. arXiv: 2012 1704.07983 [hep-ex] (cit. on p. 34).
- 2013 [97] T. Cornelissen et al. *Concepts, design and implementation of the ATLAS New Track- 2014 ing (NEWT)*. Tech. rep. Geneva: CERN, 2007. URL: [https://cds.cern.ch/record/1020106](https://cds.cern.ch/record/2015 1020106) (cit. on p. 34).
- 2016 [98] A. Salzburger. *Optimisation of the ATLAS Track Reconstruction Software for Run-2*. 2017 Journal of Physics: Conference Series 664.7 (2015), p. 072042 (cit. on p. 34).

- 2019 [99] R. Frühwirth. *Application of Kalman filtering to track and vertex fitting*. Nucl. Instrum. Methods Phys. Res. A 262.2 (1987), pp. 444–450. ISSN: 0168-9002 (cit. on  
2020 p. 34).
- 2022 [100] T. Cornelissen et al. *The global  $\chi^2$  track fitter in ATLAS*. Journal of Physics: Con-  
2023 ference Series 119.3 (2008), p. 032013 (cit. on p. 34).
- 2024 [101] ATLAS Collaboration. *Improved electron reconstruction in ATLAS using the Gaus-  
2025 sian Sum Filter-based model for bremsstrahlung*. ATLAS-CONF-2012-047. 2012. URL:  
2026 <https://cds.cern.ch/record/1449796> (cit. on p. 34).
- 2027 [102] D. Wicke. *A new algorithm for solving tracking ambiguities*. Tech. rep. Oct. 1998.  
2028 URL: <https://cds.cern.ch/record/2625731> (cit. on p. 35).
- 2029 [103] ATLAS Collaboration. *Reconstruction of primary vertices at the ATLAS experiment  
2030 in Run 1 proton–proton collisions at the LHC*. Eur. Phys. J. C 77 (2017), p. 332.  
2031 arXiv: [1611.10235 \[physics.ins-det\]](https://arxiv.org/abs/1611.10235) (cit. on p. 35).
- 2032 [104] W. Waltenberger, R. Frühwirth, and P. Vanlaer. *Adaptive vertex fitting*. Journal of  
2033 Physics G: Nuclear and Particle Physics 34.12 (2007), N343 (cit. on p. 35).
- 2034 [105] ATLAS Collaboration. *Secondary vertex finding for jet flavour identification with the  
2035 ATLAS detector*. ATL-PHYS-PUB-2017-011. 2017. URL: <https://cds.cern.ch/record/2270366> (cit. on p. 35).
- 2037 [106] ATLAS Collaboration. *Performance of pile-up mitigation techniques for jets in pp  
2038 collisions at  $\sqrt{s} = 8 \text{ TeV}$  using the ATLAS detector*. Eur. Phys. J. C 76 (2016),  
2039 p. 581. arXiv: [1510.03823 \[hep-ex\]](https://arxiv.org/abs/1510.03823) (cit. on pp. 36, 39).

- 2040 [107] ATLAS Collaboration. *Topological cell clustering in the ATLAS calorimeters and its*  
2041 *performance in LHC Run 1.* *Eur. Phys. J. C* **77** (2017), p. 490. arXiv: [1603.02934](#)  
2042 [[hep-ex](#)] (cit. on pp. 36, 37).
- 2043 [108] ATLAS Collaboration. *Jet reconstruction and performance using particle flow with*  
2044 *the ATLAS Detector.* *Eur. Phys. J. C* **77** (2017), p. 466. arXiv: [1703.10485](#) [[hep-ex](#)]  
2045 (cit. on p. 38).
- 2046 [109] M. Cacciari, G. P. Salam, and G. Soyez. *The anti- $k_t$  jet clustering algorithm.* *JHEP*  
2047 **04** (2008), p. 063. arXiv: [0802.1189](#) [[hep-ph](#)] (cit. on p. 38).
- 2048 [110] ATLAS Collaboration. *Jet energy scale and resolution measured in proton–proton*  
2049 *collisions at  $\sqrt{s} = 13\text{ TeV}$  with the ATLAS detector.* *Eur. Phys. J. C* **81** (2021),  
2050 p. 689. arXiv: [2007.02645](#) [[hep-ex](#)] (cit. on pp. 39, 75–77).
- 2051 [111] ATLAS Collaboration. *Jet energy scale measurements and their systematic uncertain-*  
2052 *ties in proton–proton collisions at  $\sqrt{s} = 13\text{ TeV}$  with the ATLAS detector.* *Phys. Rev.*  
2053 **D 96** (2017), p. 072002. arXiv: [1703.09665](#) [[hep-ex](#)] (cit. on pp. 39, 75).
- 2054 [112] ATLAS Collaboration. *Transforming jet flavour tagging at ATLAS.* Tech. rep. Sub-  
2055 mitted to: Nature Communications. Geneva: CERN, 2025. arXiv: [2505.19689](#) (cit. on  
2056 pp. 40–42).
- 2057 [113] A. Vaswani et al. *Attention Is All You Need.* 2023. arXiv: [1706.03762](#) [[cs.CL](#)] (cit. on  
2058 p. 40).
- 2059 [114] ATLAS Collaboration. *Measurements of  $b$ -jet tagging efficiency with the ATLAS de-*  
2060 *tector using  $t\bar{t}$  events at  $\sqrt{s} = 13\text{ TeV}.$*  *JHEP* **08** (2018), p. 089. arXiv: [1805.01845](#)  
2061 [[hep-ex](#)] (cit. on pp. 42, 77).

- 2062 [115] ATLAS Collaboration. *Electron reconstruction and identification in the ATLAS ex-*  
 2063 *periment using the 2015 and 2016 LHC proton–proton collision data at  $\sqrt{s} = 13$  TeV.*  
 2064 *Eur. Phys. J. C* **79** (2019), p. 639. arXiv: [1902.04655 \[physics.ins-det\]](#) (cit. on  
 2065 pp. 43–45).
- 2066 [116] ATLAS Collaboration. *Muon reconstruction and identification efficiency in ATLAS*  
 2067 *using the full Run 2 pp collision data set at  $\sqrt{s} = 13$  TeV.* *Eur. Phys. J. C* **81** (2021),  
 2068 p. 578. arXiv: [2012.00578 \[hep-ex\]](#) (cit. on pp. 46, 47).
- 2069 [117] ATLAS Collaboration. *Muon reconstruction performance of the ATLAS detector in*  
 2070 *proton–proton collision data at  $\sqrt{s} = 13$  TeV.* *Eur. Phys. J. C* **76** (2016), p. 292. arXiv:  
 2071 [1603.05598 \[hep-ex\]](#) (cit. on p. 47).
- 2072 [118] ATLAS Collaboration. *Performance of missing transverse momentum reconstruction*  
 2073 *with the ATLAS detector using proton–proton collisions at  $\sqrt{s} = 13$  TeV.* *Eur. Phys.*  
 2074 *J. C* **78** (2018), p. 903. arXiv: [1802.08168 \[hep-ex\]](#) (cit. on pp. 48, 77).
- 2075 [119] ATLAS Collaboration.  *$E_T^{\text{miss}}$  performance in the ATLAS detector using 2015–2016*  
 2076 *LHC pp collisions.* ATLAS-CONF-2018-023. 2018. URL: <https://cds.cern.ch/record/2625233> (cit. on p. 49).
- 2078 [120] J. Alwall et al. *The automated computation of tree-level and next-to-leading order*  
 2079 *differential cross sections, and their matching to parton shower simulations.* *JHEP* **07**  
 2080 (2014), p. 079. arXiv: [1405.0301 \[hep-ph\]](#) (cit. on pp. 52, 54–57).
- 2081 [121] NNPDF Collaboration, R. D. Ball, et al. *Parton distributions for the LHC run II.*  
 2082 *JHEP* **04** (2015), p. 040. arXiv: [1410.8849 \[hep-ph\]](#) (cit. on pp. 52, 54–58).
- 2083 [122] T. Sjöstrand et al. *An introduction to PYTHIA 8.2.* *Comput. Phys. Commun.* **191**  
 2084 (2015), p. 159. arXiv: [1410.3012 \[hep-ph\]](#) (cit. on pp. 52, 54–58).

- 2085 [123] ATLAS Collaboration. *ATLAS Pythia 8 tunes to 7 TeV data*. ATL-PHYS-PUB-2014-  
 2086 021. 2014. URL: <https://cds.cern.ch/record/1966419> (cit. on pp. 54–58).
- 2087 [124] S. Frixione, E. Laenen, P. Motylinski, and B. R. Webber. *Angular correlations of*  
 2088 *lepton pairs from vector boson and top quark decays in Monte Carlo simulations*.  
 2089 JHEP 04 (2007), p. 081. arXiv: [hep-ph/0702198](https://arxiv.org/abs/hep-ph/0702198) (cit. on p. 54).
- 2090 [125] P. Artoisenet, R. Frederix, O. Mattelaer, and R. Rietkerk. *Automatic spin-entangled*  
 2091 *decays of heavy resonances in Monte Carlo simulations*. JHEP 03 (2013), p. 015.  
 2092 arXiv: [1212.3460 \[hep-ph\]](https://arxiv.org/abs/1212.3460) (cit. on p. 54).
- 2093 [126] D. J. Lange. *The EvtGen particle decay simulation package*. Nucl. Instrum. Meth. A  
 2094 462 (2001), p. 152 (cit. on p. 54).
- 2095 [127] R. Frederix, D. Pagani, and M. Zaro. *Large NLO corrections in  $t\bar{t}W^\pm$  and  $t\bar{t}t\bar{t}$*   
 2096 *hadroproduction from supposedly subleading EW contributions*. JHEP 02 (2018), p. 031.  
 2097 arXiv: [1711.02116 \[hep-ph\]](https://arxiv.org/abs/1711.02116) (cit. on pp. 54, 79).
- 2098 [128] E. Bothmann et al. *Event generation with Sherpa 2.2*. SciPost Phys. 7.3 (2019), p. 034.  
 2099 arXiv: [1905.09127 \[hep-ph\]](https://arxiv.org/abs/1905.09127) (cit. on pp. 54, 55, 57).
- 2100 [129] S. Schumann and F. Krauss. *A parton shower algorithm based on Catani–Seymour*  
 2101 *dipole factorisation*. JHEP 03 (2008), p. 038. arXiv: [0709.1027 \[hep-ph\]](https://arxiv.org/abs/0709.1027) (cit. on  
 2102 pp. 54, 57, 58).
- 2103 [130] S. Höche, F. Krauss, M. Schönherr, and F. Siegert. *A critical appraisal of NLO+PS*  
 2104 *matching methods*. JHEP 09 (2012), p. 049. arXiv: [1111.1220 \[hep-ph\]](https://arxiv.org/abs/1111.1220) (cit. on pp. 54,  
 2105 57, 58).

- 2106 [131] S. Höche, F. Krauss, M. Schönherr, and F. Siegert. *QCD matrix elements + parton*  
 2107       *showers. The NLO case.* JHEP 04 (2013), p. 027. arXiv: [1207.5030 \[hep-ph\]](#) (cit. on  
 2108       pp. 54, 57, 58).
- 2109 [132] S. Catani, F. Krauss, B. R. Webber, and R. Kuhn. *QCD Matrix Elements + Parton*  
 2110       *Showers.* JHEP 11 (2001), p. 063. arXiv: [hep-ph/0109231](#) (cit. on pp. 54, 57, 58).
- 2111 [133] S. Höche, F. Krauss, S. Schumann, and F. Siegert. *QCD matrix elements and truncated*  
 2112       *showers.* JHEP 05 (2009), p. 053. arXiv: [0903.1219 \[hep-ph\]](#) (cit. on pp. 54, 57, 58).
- 2113 [134] F. Cascioli, P. Maierhöfer, and S. Pozzorini. *Scattering Amplitudes with Open Loops.*  
 2114       Phys. Rev. Lett. 108 (2012), p. 111601. arXiv: [1111.5206 \[hep-ph\]](#) (cit. on pp. 54,  
 2115       57, 58).
- 2116 [135] A. Denner, S. Dittmaier, and L. Hofer. *COLLIER: A fortran-based complex one-loop*  
 2117       *library in extended regularizations.* Comput. Phys. Commun. 212 (2017), pp. 220–238.  
 2118       arXiv: [1604.06792 \[hep-ph\]](#) (cit. on pp. 54, 57, 58).
- 2119 [136] F. Buccioni et al. *OpenLoops 2.* Eur. Phys. J. C 79.10 (2019), p. 866. arXiv: [1907.13071](#)  
 2120       [hep-ph] (cit. on p. 54).
- 2121 [137] S. Frixione, G. Ridolfi, and P. Nason. *A positive-weight next-to-leading-order Monte*  
 2122       *Carlo for heavy flavour hadroproduction.* JHEP 09 (2007), p. 126. arXiv: [0707.3088](#)  
 2123       [hep-ph] (cit. on pp. 55, 56, 58).
- 2124 [138] P. Nason. *A new method for combining NLO QCD with shower Monte Carlo algo-*  
 2125       *rithms.* JHEP 11 (2004), p. 040. arXiv: [hep-ph/0409146](#) (cit. on pp. 55, 56, 58).
- 2126 [139] S. Frixione, P. Nason, and C. Oleari. *Matching NLO QCD computations with parton*  
 2127       *shower simulations: the POWHEG method.* JHEP 11 (2007), p. 070. arXiv: [0709.2092](#)  
 2128       [hep-ph] (cit. on pp. 55, 56, 58).

- 2129 [140] S. Alioli, P. Nason, C. Oleari, and E. Re. *A general framework for implementing NLO*  
 2130 *calculations in shower Monte Carlo programs: the POWHEG BOX*. *JHEP* **06** (2010),  
 2131 p. 043. arXiv: [1002.2581 \[hep-ph\]](#) (cit. on pp. 55, 56, 58).
- 2132 [141] NNPDF Collaboration, R. D. Ball, et al. *Parton distributions with LHC data*. *Nucl.*  
 2133 *Phys. B* **867** (2013), p. 244. arXiv: [1207.1303 \[hep-ph\]](#) (cit. on pp. 55, 56, 58).
- 2134 [142] M. Bähr et al. *Herwig++ physics and manual*. *Eur. Phys. J. C* **58** (2008), p. 639.  
 2135 arXiv: [0803.0883 \[hep-ph\]](#) (cit. on p. 55).
- 2136 [143] J. Bellm et al. *Herwig 7.0/Herwig++ 3.0 release note*. *Eur. Phys. J. C* **76**.4 (2016),  
 2137 p. 196. arXiv: [1512.01178 \[hep-ph\]](#) (cit. on p. 55).
- 2138 [144] S. Alekhin, J. Blümlein, S. Klein, and S. Moch. *The 3-, 4-, and 5-flavor NNLO parton*  
 2139 *distribution functions from deep-inelastic-scattering data at hadron colliders*. *Physical*  
 2140 *Review D* **81**.1 (Jan. 2010). ISSN: 1550-2368. arXiv: [0908.2766 \[hep-ph\]](#) (cit. on  
 2141 pp. 55, 56).
- 2142 [145] ATLAS Collaboration. *Studies on top-quark Monte Carlo modelling for Top2016*.  
 2143 ATL-PHYS-PUB-2016-020. 2016. URL: <https://cds.cern.ch/record/2216168> (cit. on  
 2144 p. 56).
- 2145 [146] S. Frixione, E. Laenen, P. Motylinski, C. White, and B. R. Webber. *Single-top hadropro-*  
 2146 *duction in association with a W boson*. *JHEP* **07** (2008), p. 029. arXiv: [0805.3067](#)  
 2147 [\[hep-ph\]](#) (cit. on p. 56).
- 2148 [147] T. Gleisberg and S. Höche. *Comix, a new matrix element generator*. *JHEP* **12** (2008),  
 2149 p. 039. arXiv: [0808.3674 \[hep-ph\]](#) (cit. on p. 57).

- 2150 [148] C. Anastasiou, L. Dixon, K. Melnikov, and F. Petriello. *High-precision QCD at hadron*  
 2151 *colliders: Electroweak gauge boson rapidity distributions at next-to-next-to leading or-*  
 2152 *der.* Phys. Rev. D 69 (2004), p. 094008. arXiv: [hep-ph/0312266](#) (cit. on p. 57).
- 2153 [149] ATLAS Collaboration. *ATLAS data quality operations and performance for 2015–*  
 2154 *2018 data-taking.* JINST 15 (2020), P04003. arXiv: [1911.04632 \[physics.ins-det\]](#)  
 2155 (cit. on p. 59).
- 2156 [150] ATLAS Collaboration. *Analysis of  $t\bar{t}H$  and  $t\bar{t}W$  production in multilepton final states*  
 2157 *with the ATLAS detector.* ATLAS-CONF-2019-045. 2019. URL: <https://cds.cern.ch/record/2693930> (cit. on pp. 64, 68, 81).
- 2159 [151] ATLAS Collaboration. *Measurement of the total and differential cross-sections of  $t\bar{t}W$*   
 2160 *production in  $pp$  collisions at  $\sqrt{s} = 13 \text{ TeV}$  with the ATLAS detector.* JHEP 05 (2024),  
 2161 p. 131. arXiv: [2401.05299 \[hep-ex\]](#) (cit. on p. 64).
- 2162 [152] ATLAS Collaboration. *Search for new phenomena in events with same-charge leptons*  
 2163 *and  $b$ -jets in  $pp$  collisions at  $\sqrt{s} = 13 \text{ TeV}$  with the ATLAS detector.* JHEP 12 (2018),  
 2164 p. 039. arXiv: [1807.11883 \[hep-ex\]](#) (cit. on p. 69).
- 2165 [153] ATLAS Collaboration. *Search for  $R$ -parity-violating supersymmetry in a final state*  
 2166 *containing leptons and many jets with the ATLAS experiment using  $\sqrt{s} = 13 \text{ TeV}$*   
 2167 *proton–proton collision data.* Eur. Phys. J. C 81 (2021), p. 1023. arXiv: [2106.09609 \[hep-ex\]](#) (cit. on p. 71).
- 2169 [154] E. Gerwick, T. Plehn, S. Schumann, and P. Schichtel. *Scaling Patterns for QCD Jets.*  
 2170 JHEP 10 (2012), p. 162. arXiv: [1208.3676 \[hep-ph\]](#) (cit. on pp. 71, 72).
- 2171 [155] G. Avoni et al. *The new LUCID-2 detector for luminosity measurement and moni-*  
 2172 *toring in ATLAS.* JINST 13.07 (2018), P07017 (cit. on p. 74).

- 2173 [156] ATLAS Collaboration. *Tagging and suppression of pileup jets*. ATL-PHYS-PUB-2014-  
2174 001. 2014. URL: <https://cds.cern.ch/record/1643929> (cit. on pp. 75, 77).
- 2175 [157] ATLAS Collaboration. *Measurements of inclusive and differential fiducial cross-sections  
2176 of  $t\bar{t}$  production with additional heavy-flavour jets in proton–proton collisions at  $\sqrt{s} =$   
2177 13 TeV with the ATLAS detector*. JHEP 04 (2019), p. 046. arXiv: 1811.12113 [hep-ex]  
2178 (cit. on p. 79).
- 2179 [158] D. de Florian et al. *Handbook of LHC Higgs Cross Sections: 4. Deciphering the Nature  
2180 of the Higgs Sector*. CERN Yellow Rep. Monogr. 2 (2017), pp. 1–869. arXiv: 1610.  
2181 07922 [hep-ph] (cit. on p. 79).
- 2182 [159] ATLAS Collaboration. *Measurement of the production cross-section of a single top  
2183 quark in association with a Z boson in proton–proton collisions at 13 TeV with the  
2184 ATLAS detector*. ATLAS-CONF-2017-052. 2017. URL: <https://cds.cern.ch/record/2273868> (cit. on p. 79).
- 2186 [160] F. Demartin, B. Maier, F. Maltoni, K. Mawatari, and M. Zaro. *tWH associated  
2187 production at the LHC*. EPJC 77.1 (2017). arXiv: 1607.05862 [hep-ph]. URL: <https://doi.org/10.1140/epjc/s10052-017-4601-7> (cit. on p. 79).
- 2189 [161] ATLAS Collaboration. *Measurement of  $W^\pm Z$  production cross sections and gauge  
2190 boson polarisation in pp collisions at  $\sqrt{s} = 13$  TeV with the ATLAS detector*. Eur.  
2191 Phys. J. C 79 (2019), p. 535. arXiv: 1902.05759 [hep-ex] (cit. on p. 79).
- 2192 [162] G. Cowan, K. Cranmer, E. Gross, and O. Vitells. *Asymptotic formulae for likelihood-  
2193 based tests of new physics*. The European Physical Journal C 71.2 (Feb. 2011). ISSN:  
2194 1434-6052. arXiv: 1007.1727 [physics.data-an]. URL: <http://dx.doi.org/10.1140/epjc/s10052-011-1554-0> (cit. on p. 83).

- 2196 [163] J. Neyman and E. S. Pearson. *IX. On the problem of the most efficient tests of*  
2197 *statistical hypotheses.* Philosophical Transactions of the Royal Society of London.  
2198 Series A, Containing Papers of a Mathematical or Physical Character 231.694-706  
2199 (1933), pp. 289–337 (cit. on p. 83).
- 2200 [164] S. S. Wilks. *The large-sample distribution of the likelihood ratio for testing composite*  
2201 *hypotheses.* Annals of Mathematical Statistics 9.1 (1938), pp. 60–62 (cit. on p. 84).
- 2202 [165] T. Junk. *Confidence level computation for combining searches with small statistics.*  
2203 Nuclear Instruments and Methods in Physics Research Section A: Accelerators, Spec-  
2204 trometers, Detectors and Associated Equipment 434.23 (Sept. 1999), 435443. ISSN:  
2205 0168-9002. arXiv: [hep-ex/9902006 \[hep-ex\]](https://arxiv.org/abs/hep-ex/9902006) (cit. on p. 85).
- 2206 [166] A. L. Read. *Modified frequentist analysis of search results: The CLs method.* Tech.  
2207 rep. CERN-OPEN-2000-205. Presented at Workshop on Confidence Limits, Geneva,  
2208 Switzerland. CERN, 2000. URL: <https://cds.cern.ch/record/451614> (cit. on p. 85).